

Check
AD736015

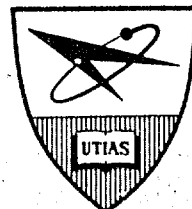
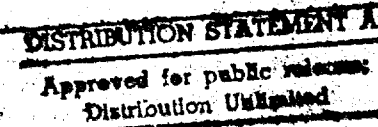
INSTITUTE
FOR
AEROSPACE STUDIES

UNIVERSITY OF TORONTO

AN EXPERIMENTAL DETERMINATION OF THE
POLARIZABILITY FOR SINGLY IONIZED ARGON

by

M. P. F. Bristow



DDC
REF ID: A65513
JAN 28 1972
K3 C

**BEST
AVAILABLE COPY**

72-141
P
April, 1971.

Reproduced by
NATIONAL TECHNICAL
INFORMATION SERVICE
Springfield, Va. 22151

UTIAS Report No. 158
AFOSR-TR-71-2461

UNCLASSIFIED

Security Classification

DOCUMENT CONTROL DATA - R&D

(Security classification of title, body of abstract and indexing annotation must be entered when the overall report is classified)

1. ORIGINATING ACTIVITY (Corporate author) University of Toronto, Institute for Aerospace Studies. Toronto 5, Ontario, Canada.		2a. REPORT SECURITY CLASSIFICATION UNCLASSIFIED
		2b. GROUP
3. REPORT TITLE AN EXPERIMENTAL DETERMINATION OF THE POLARIZABILITY FOR SINGLY IONIZED ARGON		
4. DESCRIPTIVE NOTE ⁴ (Type of report and inclusive dates) Scientific Interim		
5. AUTHOR(S) (Last name, first name, initial) M. P. F. Bristow		
6. REPORT DATE April, 1971.	7a. TOTAL NO. OF PAGES 53	7b. NO. OF REFS 82
8a. CONTRACT OR GRANT NO. AFOSR-1368-68	8b. ORIGINATOR'S REPORT NUMBER(S) UTIAS Report No. 158	
8c. PROJECT NO. 9783-01	8d. OTHER REPORT NO(S) (Any other numbers that may be assigned this report) AFOSR-TR-71-2461	
10. AVAILABILITY/LIMITATION NOTICES Approved for public release; distribution unlimited		
11. SUPPLEMENTARY NOTES TECH, OTHER	12. SPONSORING MILITARY ACTIVITY AF Office of Scientific Research (NAM), 1400 Wilson Blvd, Arlington, Virginia, 22209, USA	
13. ABSTRACT <p>Two-wavelength interferometry, employing either a ruby (6943Å) or a neodymium (10,600Å) laser with a second harmonic generator, was used to study argon plasmas in a shock tube for shock Mach numbers from 17 to 24, initial pressures from 3.0 to 0.3 mm Hg and for degrees of ionization up to 50%. The measured equilibrium electron densities for both wavelength pairs were about 1.9% greater than the calculated values accounting for the excited states, but 1.6% less than the values based on the neglect of these states. Assuming a plasma of free electrons and ground-state atoms and ions, the interferograms yielded ratios of the polarizability for the argon ion to that for the atom of 0.650 ± 0.33 at 3471Å and 0.647 ± 0.41 at 5300Å. These results are in general agreement with the value of 0.716 for the ratio of the static polarizabilities obtained by the method of Slater screening constants. The uniformity of the measured electron densities and polarizabilities with change in wavelength suggests that the effect of the excited state refractivities are not important for temperatures up to 13,500°K.</p>		

UNCLASSIFIED

Security Classification

14. KEY WORDS	LINK A		LINK B		LINK C	
	ROLE	WT	ROLE	WT	ROLE	WT
1. Refractive index 2. Polarizability 3. Argon plasma 4. Laser interferometry 5. Shock waves						
INSTRUCTIONS						
1. ORIGINATING ACTIVITY: Enter the name and address of the contractor, subcontractor, grantee, Department of Defense activity or other organization (corporate author) issuing the report.	imposed by security classification, using standard statements such as:					
2a. REPORT SECURITY CLASSIFICATION: Enter the overall security classification of the report. Indicate whether "Restricted Data" is included. Marking is to be in accordance with appropriate security regulations.	<ul style="list-style-type: none"> (1) "Qualified requesters may obtain copies of this report from DDC." (2) "Foreign announcement and dissemination of this report by DDC is not authorized." (3) "U. S. Government agencies may obtain copies of this report directly from DDC. Other qualified DDC users shall request through ." 					
2b. GROUP: Automatic downgrading is specified in DoD Directive 5200.10 and Armed Forces Industrial Manual. Enter the group number. Also, when applicable, show that optional markings have been used for Group 3 and Group 4 as authorized.	<ul style="list-style-type: none"> (4) "U. S. military agencies may obtain copies of this report directly from DDC. Other qualified users shall request through ." (5) "All distribution of this report is controlled. Qualified DDC users shall request through ." 					
3. REPORT TITLE: Enter the complete report title in all capital letters. Titles in all cases should be unclassified. If a meaningful title cannot be selected without classification, show title classification in all capitals in parenthesis immediately following the title.	<p>If the report has been furnished to the Office of Technical Services, Department of Commerce, for sale to the public, indicate this fact and enter the price, if known.</p>					
4. DESCRIPTIVE NOTES: If appropriate, enter the type of report, e.g., interim, progress, summary, annual, or final. Give the inclusive dates when a specific reporting period is covered.	11. SUPPLEMENTARY NOTES: Use for additional explanatory notes.					
5. AUTHOR(S): Enter the name(s) of author(s) as shown on or in the report. Enter last name, first name, middle initial. If military, show rank and branch of service. The name of the principal author is an absolute minimum requirement.	12. SPONSORING MILITARY ACTIVITY: Enter the name of the departmental project office or laboratory sponsoring (paying for) the research and development. Include address.					
6. REPORT DATE: Enter the date of the report as day, month, year, or month, year. If more than one date appears on the report, use date of publication.	13. ABSTRACT: Enter an abstract giving a brief and factual summary of the document indicative of the report, even though it may also appear elsewhere in the body of the technical report. If additional space is required, a continuation sheet shall be attached.					
7a. TOTAL NUMBER OF PAGES: The total page count should follow normal pagination procedures; i.e., enter the number of pages containing information.	It is highly desirable that the abstract of classified reports be unclassified. Each paragraph of the abstract shall end with an indication of the military security classification of the information in the paragraph, represented as (TS), (S), (C), or (U).					
7b. NUMBER OF REFERENCES: Enter the total number of references cited in the report.	There is no limitation on the length of the abstract. However, the suggested length is from 150 to 225 words.					
8a. CONTRACT OR GRANT NUMBER: If appropriate, enter the applicable number of the contract or grant under which the report was written.	14. KEY WORDS: Key words are technically meaningful terms or short phrases that characterize a report and may be used as index entries for cataloging the report. Key words must be selected so that no security classification is required. Identifiers, such as equipment model designation, trade name, military project code name, geographic location, may be used as key words but will be followed by an indication of technical context. The assignment of links, rules, and weights is optional.					
8b, 8c, & 8d. PROJECT NUMBER: Enter the appropriate military department identification, such as project number, subproject number, system numbers, task number, etc.						
9a. ORIGINATOR'S REPORT NUMBER(S): Enter the official report number by which the document will be identified and controlled by the originating activity. This number must be unique to this report.						
9b. OTHER REPORT NUMBER(S): If the report has been assigned any other report numbers (either by the originator or by the sponsor), also enter this number(s).						
10. AVAILABILITY/LIMITATION NOTICES: Enter any limitations on further dissemination of the report, other than those						

UNCLASSIFIED

Security Classification

AN EXPERIMENTAL DETERMINATION OF THE
POLARIZABILITY FOR SINGLY IONIZED ARGON

by

M. P. F. Bristow

Manuscript submitted Jan, 1971.

April, 1971.

UTIAS Report No.158

ACKNOWLEDGEMENT

The author wishes to express his thanks to Dr. G. N. Patterson, Director of the Institute, for the opportunity to study at UTIAS.

I wish to thank Dr. I. I. Glass for his continued interest and encouragement throughout the course of this research.

The advice and assistance in operating the shock tube facility received from Mr. P. Crouse and the technical support staff are gratefully acknowledged.

Thanks must also go to N. Chan, K. H. Gindl and B. Whitten for their assistance with the numerical computations. In addition the author would like to thank D. Wettlaufer for making available the interferogram in Fig. 8(a).

The Postdoctorate Research Fellowship awarded to the author by the Institute for Aerospace Studies is acknowledged with thanks. Financial support for this research was provided by the Air Force Office of Scientific Research under Grant No. AF-AFOSR 68-1368A and by the National Research Council of Canada.

SUMMARY

Two-wavelength interferometry, employing either a ruby (6943\AA) or a neodymium ($10,600\text{\AA}$) laser with a second harmonic generator, was used to study argon plasmas in a shock tube for shock Mach numbers from 17 to 24, initial pressures from 3.0 to 0.3 mm Hg and for degrees of ionization up to 50%. The measured equilibrium electron densities for both wavelength pairs were about 1.9% greater than the calculated values accounting for the excited states, but 1.6% less than the values based on the neglect of these states. Assuming a plasma of free electrons and ground-state atoms and ions, the interferograms yielded ratios of the polarizability for the argon ion to that for the atom of $0.650 \pm .033$ at 3471\AA and $0.647 \pm .041$ at 5300\AA . These results are in general agreement with the value of 0.716 for the ratio of the static polarizabilities obtained by the method of Slater screening constants. The uniformity of the measured electron densities and polarizabilities with change in wavelength suggests that the effect of the excited state refractivities are not important for temperatures up to $13,500^{\circ}\text{K}$.

TABLE OF CONTENTS

	<u>PAGE</u>
Acknowledgements	
Summary	
Notation	
I. INTRODUCTION	1
1.1 Introduction	1
1.2 Review	1
2. THEORETICAL CONSIDERATIONS	3
2.1 Plasma Refractive Index	3
2.2 Relations Between Fringe Shift and the Change in the Plasma Phase Refractive Index	11
2.3 Determination of the Plasma Electron Density by the Method of Two Wavelength Interferometry	12
3. THE EXPERIMENTAL FACILITIES	14
3.1 Shock Tube	14
3.1.1 Shock Tube Driver Section	14
3.1.2 Criteria for the Design of Shock Tube Diaphragms	15
3.1.3 Shock Tube Driven Section	17
3.1.4 Measurement of the Incident Shock Wave Properties	17
3.2 Optical Diagnostic and Recording Equipment	20
3.2.1 Laser Light Source	20
3.2.2 Electronic Operation of the Laser System	23
3.2.3 Mach-Zehnder Interferometer	24
3.2.4 Adjustment and Operation of the Interferometer	25
3.2.5 Test and Reference Section Windows	26
3.2.6 Interference Fringe Photography	27
3.3 Data Analysis	28
4. EXPERIMENTAL MEASUREMENTS, RESULTS, DISCUSSION AND CONCLUSIONS	28
4.1 Introduction	28
4.2 Experimental Measurements	29
4.2.1 Flow Disturbances	29
4.2.2 Interferometric Measurements	35
4.3 Experimental Determination of the Equilibrium Electron Density	36

	<u>PAGE</u>
4.4 Experimental Determination of the Polarizability for Singly-Ionized Argon	40
4.5 Conclusions	44
REFERENCES	45
TABLES	
FIGURES	
APPENDICES: Appendix A	

NOTATION

A	Einstein coefficient of spontaneous emission
A, B	Integral fringe shifts (Appendix A)
a,b,c,d,k,l,m,n	Dimensional fractional fringe shifts (Appendix A)
c	Velocity of light
e	Electronic charge
E	Energy of electronic quantum state above ground state
f	Absorption oscillator strength
g	Statistic weight (degeneracy) of electron quantum state
h	Planck's constant
K	Specific refractivity (Gladstone-Dale Constant)
k	Boltzmann's constant
L	Test section geometrical path length
M	Mach number
m	Electron mass
N	Particle number density, also number of statistical samples
p	Pressure
q	Principal quantum number
s	Total fringe shift
T	Temperature
X	Total ionization relaxation zone length
x	Degree of single ionization
α	Induced electric dipole polarizability
γ	Absorption damping factor
λ	Wavelength of electromagnetic radiation
μ	Phase refractive index
ν	Frequency of electromagnetic radiation

ρ Mass density
 σ Photoionization cross-section, also standard deviation
 Ψ Partition function

Subscripts

A Neutral atom species.
 A^* Neutral atom excited state species
c Continuum energy level
e Free electron species
I First ion species
L Energy level located at ionization limit
 m, n Electronic energy level
P Plasma
p Pressure
r Bound classical electron oscillator
S Normal incident shock
s Plasma species
T Temperature
X Laser second harmonic wavelength
Y Laser fundamental wavelength
0 Ground state energy level. Also conditions of Standard Temperature and Pressure (STP, 273.16°C and 760 mmHg)
1 Preshock state
2 Post shock equilibrium state
4 Combustion driver gas state

Superscripts

E Experimental value
F Calculated value for which excited electronic states are omitted

G

Calculated value for which excited electronic states are included

λ

Wavelength

Physical Constants

Values of physical constants were taken from Ref. 78

1. INTRODUCTION AND REVIEW

1.1 Introduction

A knowledge of the electric dipole polarizability for atomic or molecular species is an essential prerequisite to obtaining a better understanding of how individual atoms and molecules interact both with each other, with free electrons and other forms of matter and finally with static and dynamic electric and magnetic fields. Typical properties which are intimately related to the polarizability are the long range intermolecular dispersion force constant, the Verdet constant of Faraday optical rotation, the diamagnetic susceptibility, the Rayleigh scattering cross section, the total effective oscillator strength and the dielectric constant.

However, it is the relationship between the polarizability α_s for species s and the phase refractive index μ_s representing the bulk property of the transmitting medium which is of primary interest in the present circumstance; for dilute gases this relationship is given by (Ref. 3)

$$(\mu_s - 1) = 2\pi N_s \alpha_s \quad (1.1.1)$$

where N_s is the particle number density of species s .

Experimentally measured refractive indices provide a relatively accurate yardstick against which the merits of the presently available theoretical calculations can be judged. However, a more practical need arises during the optical and particularly the interferometric study of transparent systems which are undergoing either physical or chemical changes. Clearly the refractive indices of all species present during the reaction must be known prior to interpretation of the experimental data obtained through interferometry.

In particular, this laboratory is presently undertaking an interferometric study of nonequilibrium shock generated argon plasmas which requires a knowledge of the refractivities of all the plasma species present, viz., the free electrons, the neutral argon atoms and the singly charged ions. As the refractivity for this latter species is as yet unknown, it is to be the purpose of the present study to experimentally determine a value for this quantity.

1.2 Review

Previous measurements of the polarizabilities of chemically active gaseous species, normally existing only at high temperatures, have been made almost exclusively using the shock tube in conjunction with a (Mach-Zehndar) interferometer (Refs. 1 to 9); the authors and respective species are indicated in Table. 1.

Although numerous optical and particularly interferometric studies have been made on argon plasmas, the contribution of the bound electrons to the overall plasma refractive index is usually neglected or at best approximated by the neutral atom ground state value in view of the relatively large refractivity and strong dispersion of the free electrons.

There have been two studies which have specifically set out to measure the refractivity of an argon plasma. Firstly, Alpher and White (Réfs. 1,2), who pioneered the use of the shock tube-interferometer technique in measuring

the polarizability of high temperature species, employed interferometry simultaneously at two wavelengths. By assuming the dispersion for the atom and ion to be negligibly small, they showed that the measured and calculated electron densities were in good agreement, but with the average experimental value being about 2% greater than the value calculated from the shock Hugoniot equation. From this agreement, it was concluded that the theoretical free electron refractive index μ_e , given by (see Section 2.1),

$$(\mu_e - 1) = - 4.484 \times 10^{-14} \lambda^2 N_e \quad (1.2.1)$$

where λ and N_e are the wavelength and electron particle density respectively, is a good description of reality in the optical region of the spectrum*. The reason for this small but systematic discrepancy between the measured and calculated electron densities is not clear. It appears that their theoretical calculation employed Saha and energy equations using only the ground state terms in the summation for the electronic partition functions of the neutral atom and first ion. Consequently this calculated value is an upper bound (see Section 4.3) suggesting that the discrepancy stems from some other unspecified source. In addition, Alpher and White indicated that the measured plasma refractive index was consistently larger than the calculated value but gave no numerical estimate for this difference. This calculation assumed a plasma of free electrons and ground-state atoms and ions where the ion refractivity was taken to be 0.67 of the corresponding neutral atom value as obtained using Slater screening constant theory** (Ref. 10). However, it should be noted that this theory is at best only approximate as indicated by the fact that the absolute value of the neutral argon ground state static polarizability is about $2\frac{1}{2}$ times the well documented experimental value. Alpher and White suggested several possible explanations for this observed difference between the measured and calculated plasma refractive indices and in particular that the excited states might be contributing to the experimental measurements.

It is therefore concluded from the work of Alpher and White that the figure of 0.67 for the ratio of the polarizability of the first ion to that for the neutral atom is of the correct order of magnitude but that due to uncertainties in the measured plasma refractive index and electron density, it is not possible to place a figure on the accuracy of this result.

The second study was made by Hug, Evans, Tankin and Cambel (Refs. 13, 14) who employed optical interferometry to study axisymmetric argon plasmas produced by either a plasma jet or a free burning arc. Experimental values for the plasma refractive index were found to be generally about 12% below the calculated value based on a plasma of free electrons and ground state atoms and ions. It was suggested that this might be due to the effect of the highly excited bound electrons lying close to the continuum behaving as if free thereby producing a reduction in the value of the observed plasma refractive index. However, it should be mentioned that Alpher and White made their measurements

* Alpher and White (Ref. 2) gave a value for the constant in Eq. 1.2.1 equal to 4.46 whereas the present author calculates a value of 4.484 using the self consistent set of physical constants given in Ref. 78.

** Both the present author and Ascoli-Bartoli et al (Ref. 11) calculate a value of 0.72 for this ratio using the same theory as given in Ref. 10. In addition Alpher and White quote a value of 0.69 in Ref. 12 using the same theoretical model.

at 4122\AA and 5463\AA whereas Hug et al used a He-Ne laser at 6328\AA (Refs.: 13, 14) and also at $11,523\text{\AA}$ (Ref. 15) so that the latter measurements were more sensitive to the free electron concentration. It would therefore seem that the experiments of Hug et al were not sufficiently sensitive to resolve the contribution of the argon ion to the total plasma refractive index.

It is therefore the purpose of the present work to measure the induced electric dipole polarizability for singly ionized argon by employing short wavelength interferometry to study a shock tube generated argon plasma.

The shock tube is capable of providing a known concentration of a given species at a well defined thermodynamic state over a wide range of temperature and pressure. In addition, the gas sample is one-dimensional such that reduction of the interferometric data is most straightforward.

The refractive indices of the atom and ion plasma species are virtually independent of wavelength whereas the value for the free electrons given by Eq. 1.2.1, is strongly dispersive dictating that the experimental measurements be made at as short a wavelength as is consistent with the experimental system; this ideal is readily achieved by using the second harmonic of the ruby laser whose wavelength of 3471\AA lies just below the cut-off frequency for conventional glass optics.

In addition, by paying careful attention to accuracy in the calculation and solution of the shock Hugoniot equations and in the experimental measurements, the ion refractivity was measured with a respectable degree of accuracy in spite of the dominant contributions of the free electron and neutral atom terms to the overall plasma refractivity.

Finally, both theoretical and experimental approaches are made to determine whether the neutral atom excited states contribute significantly to the measured plasma refractive index.

2. THEORETICAL CONSIDERATIONS

2.1 Plasma Refractive Index

For pressures of the order of one atmosphere, the plasma refractive index can be given by (Ref. 12)

$$(\mu_p - 1)_{p,T} = \sum_s (\mu_s - 1)_{p,T} \quad (2.1.1)$$

where the summation extends over all 's' species which constitute the plasma at pressure p and temperature T. The assumption of additivity implies that the individual plasma components do not interact with each other, viz., that the long range attractive intermolecular forces do not contribute to the refractivity. Both experimental and theoretical values of the polarizability for argon at high pressure show that deviations from the zero pressure value are no greater than 1/2% at 100 atmospheres (Ref. 16). It is therefore assumed that the refractivity for a given species exhibits a linear dependence on density (Ref. 17).

For a plasma of neutral atoms, first ions and free electrons, Eq. 2.1.1 can be expanded to give

$$(\mu_p^{-1})_{p,T} = (\mu_e^{-1})_{p,T} + (\mu_A^{-1})_{p,T} + (\mu_I^{-1})_{p,T} \quad (2.1.2)$$

where the free electron, neutral atom and first ion terms are denoted by subscripts 'e', 'A' and 'I' respectively. The neutral atom and first ion components implicitly contain the contributions from the excited electronic states in addition to that for the ground state.

Ditchburn (Ref. 18) has given the classical derivation for the refractive index μ_s of a gaseous species, based on the dipole moment induced in the bound optical electron oscillator by an incident electromagnetic wave; this is given by (Ref. 18)

$$(\mu_s^2 - 1) = \frac{e^2 N_s}{\pi m} \sum_r \frac{f_r}{(\nu_r^2 - \nu^2 + i\gamma_r \nu)} \quad (2.1.3)$$

where f_r is the number of electron oscillators in each atom with resonant frequency ν_r , e is the electron charge, m is the electron mass, N_s is the number density of species s , ν is the frequency of the incident electromagnetic radiation, and γ_r is the absorption damping factor for electron oscillator type r .

In the optical region of the spectrum two simplifications can be made to Eq. 2.1.3. Firstly, γ_r is very small compared to ν so that provided ν , the frequency of the incident radiation, is remote from the resonance frequency ν_r , then the absorption damping term can be omitted. Secondly, in the optical region μ_s for gaseous species generally has a value close to unity so that Eq. 2.1.3 can be reliably approximated as

$$(\mu_s^2 - 1) = \frac{e^2 N_s}{2\pi m} \sum_r \frac{f_r}{(\nu_r^2 - \nu^2)} \quad (2.1.4)$$

For a free electron gas, the resonance frequencies are all zero so that Eq. 2.1.4 becomes

$$(\mu_e^{-1}) = \frac{-e^2 N_e}{2\pi m v^2} = -4.4844 \times 10^{-14} N_e \lambda^2 \quad (2.1.5)$$

where N_e is the electron density and $\lambda (=c/v)$ is the wavelength of the incident radiation. Alpher and White (Refs. 1, 2) who measured the free electron refractivity in the optical region found their results to be in close agreement with Eq. 2.1.5 (see Section 1.2).

The quantum mechanical analogue of Eq. (2.1.4) for the species refractive index is essentially the same except that the bound electron is now a quantized oscillator making transitions between any two states m and n , rather than a fixed oscillator r . Due to the existence of an infinite array of possible quantum states, the quantized analogue of Eq. 2.1.4 must be obtained by summing over all m states. This formulation was first given by Ladenberg (Refs. 19,20) who showed that for dilute gases in the absence of external fields, the total refractivity for a system of electrons bound in atomic and ionic configurations for incident radiation of frequency ν , can be given by

$$(\mu_s - 1) = \frac{e^2}{2\pi m} \sum_{m=0}^{\infty} N_m \left\{ \sum_{n=m+1}^{\infty} f_{nm} \frac{\left(1 - \frac{N_n}{N_m} \frac{g_m}{g_n}\right)}{(v_{mn}^2 - v^2)} + \int_{v_{mc} = v_{mL}}^{\infty} \frac{\partial f_{mc}}{\partial v} \frac{dv_{mc}}{(v_{mc}^2 - v^2)} \right\} \quad (2.1.6)$$

where m and n refer to any two discrete energy levels, m being the lower of the two states whose statistical weights are g_m and g_n respectively. N_m and N_n are the number densities of the atoms in these two states and v_{mn} is the frequency of the radiation emitted in the transition from n to m for which the absorption oscillator strength is f_{nm} . Similarly, subscripts L and c refer to energy levels existing at the ionization limit and in the continuum respectively.

The second term in the expression for the discrete transitions represents the effect of negative dispersion or induced emission which only becomes important at high temperatures where the populations of the excited states become significant. It should be noted that the experimental demonstration of the existence of this phenomenon by Ladenberg (Ref. 19) was an important confirmation of the correctness of the theory of quantum mechanics.

The integral within the curly brackets in Eq. 2.1.6 represents the contribution to the species refractive index due to transitions from discrete states M to continuum states C, lying at energies greater than $h\nu_{OL}$ above the ground state where $h\nu_{OL}$ is the energy required to ionize a neutral ground state atom. The partial derivative within the integral is related to the photoionization cross-section $\sigma_m(v_{mc})$ associated with absorption from discrete state M to continuum state C by the expression (Ref. 23),

$$\frac{\partial f}{\partial v_{mc}} = \sigma_m(v_{mc}) \frac{mc}{\nu_e^2}$$

It should be noted that these two phenomena are both predicted by the quantum theory of matter and have no analogue in the classical theory.

At temperatures such that the populations of the excited states are small, Eq. 2.1.6 can be simplified so that the species refractive index μ_s can be given by the ground state term for which $m = 0$, viz

$$(\mu_s - 1) = \frac{e^2 N_s}{2\pi m} \left\{ \sum_{n=1}^{\infty} \frac{f_{no}}{(v_{on}^2 - v^2)} + \int_{v_{OL}}^{\infty} \frac{\partial f_{oc}}{\partial v_{oc}} \frac{dv_{oc}}{(v_{oc}^2 - v^2)} \right\} \quad (2.1.7)$$

where N_s is the ground state number density and is hence equivalent to the total species density in the low temperature limit.

Using the few available resonance oscillator strength values for neutral argon (Ref. 21), the refractivity for this species was calculated using the first term of Eq. 2.1.7 and was found to constitute only 24% of the experimental value (Ref. 22) at 3471\AA , the wavelength of the second harmonic

of the ruby laser. Similarly, the corresponding value calculated for singly ionized argon is only 9% of the value calculated from Slater screening constant theory (see Section 1.2) where $(\mu_I - 1)/(\mu_A - 1) \approx 0.67$. Clearly many more resonance oscillator strengths for discrete transitions must be known before this approach can be used to obtain the refractive indices of species having relatively complex spectra such as argon. In addition, resonance transitions to the continuum states can be expected to make a significant contribution as is the case for helium (Ref. 23). As yet no wave mechanical calculation appears to have been made for the dispersion of either neutral or singly ionized argon.

With regard to the experimental determination of the dispersion for neutral argon, the situation is more satisfactory. Two recent measurements, the first by Peck and Fisher (Ref. 22) for visible and near infrared wavelengths and the second by Chaschina, Gladushchak and Schreider (Ref. 24) for vacuum ultra-violet wavelengths, both show very close agreement when the data of Peck and Fisher is extrapolated into the vacuum ultra-violet region (Ref. 24). Peck and Fisher gave their data in the form of the empirical dispersion formula

$$(\mu_A - 1)_0 = 6.786711 \times 10^{-5} + \frac{3.0182943 \times 10^{-102}}{(1.44 \times 10^{-6} \lambda^2 - 1)} \quad (2.1.8)$$

where the subscript '0' denotes conditions of standard density and temperature (STP), viz. 0°C and 760 mm Hg and where λ is the wavelength of the incident wavelength in Angstrom units (\AA). As these measurements were made for ambient conditions, the populations of the excited states are therefore insignificant, so that Eq. (2.1.8) in effect represents the refractivity for neutral ground state argon and is, in principle, equivalent to the expression given by Eq. (2.1.7). The experimental data represented by Eq. (2.1.8) will therefore be used to describe the dispersion of neutral (ground state) argon as it exists in the preshock state for laser wavelengths from the near infra-red through to the near ultra-violet regions of the spectrum (see Sections 3 and 4).

However, before Eq. 2.1.8 can be used to describe the neutral atom refractivity component of the plasma refractive index in Eq. 2.1.2, it has to be shown that the refractivity for neutral argon remains, for all practical purposes, constant for temperatures up to 13,500°K typical of the experiments to be described in Section 4. This implies that the effects of both negative dispersion and the excited state polarizabilities must make an insignificant contribution to the overall species refractivity in the wavelength region of interest.

In principle the species refractivity given by Eq. 2.1.6 is a function of temperature due both to the strong temperature dependence of the population number densities N_m and to the fact that the excited state polarizabilities and statistical weights diverge rapidly with increasing principal quantum number.

Firstly, consideration is given to the contribution of negative dispersion to the overall species refractivity. If the atomic and ionic electronic energy levels are assumed to exist in a Boltzmann distribution, then the population number densities are given by

$$N_m = \frac{N_s g_m \exp(-E_m/kT)}{\sum_{m=0}^{\infty} g_m \exp(-E_m/kT)} \quad (2.1.9)$$

where the summation in the denominator is the electronic partition function for species 's', N_s is the total number density for species 's' and E_m is the energy of the mth electronic state above the ground state ($m = 0$).

For the ground state, the negative dispersion factor in Eq. 2.1.6 is $(1 - N_n/N_0 \cdot g_0/g_n)$ which assumes the value $(1 - \exp(-E_n/kT))$ for a Boltzmann distribution. A 'worst case' estimate of this term can now be obtained by giving E_m a constant value corresponding to the lowest excited state which for neutral argon is that for the $3P_2$ metastable level ($3p^54s$ configuration) lying 93143 cm^{-1} above the ground state (Ref. 25). This term is now a constant with respect to m and can therefore be taken outside the summation in Eq. 2.1.6; at $13,500^\circ \text{K}$ this factor has a value of $(1 - 2 \times 10^{-5})$ which is essentially equal to unity.

As the contribution of the excited state polarizabilities to the overall species refractivity is itself considered to be of second order at least for the range of temperatures for the present experiments, it is felt that the overall effect of negative dispersion on these values will be small. However, as the energies involved in discrete non-resonance transitions for neutral argon can be considerably smaller than those for the resonance transitions, it was felt prudent to include this correction term into the calculation made to estimate the contribution of the excited state polarizabilities to the neutral argon refractivity. This calculation will be dealt with shortly.

An indication of the magnitude of polarizability for the excited states can be gauged from the value for the first excited state of neutral argon, i.e., the $3P_2$ level of the $3p^54s$ configuration. Bederson et al (Refs. 26, 27) have used an electric and magnetic field balance technique to measure the polarizability for this metastable state and found it to have a value about 30 times greater than that for the ground state. Unfortunately this technique is only suitable for measuring the polarizabilities of metastable excited states due to their relatively long lifetimes. It should be noted that, at $13,500^\circ \text{K}$, the population of the $3P_2$ level is about $1/5000$ of the ground state value so that considered alone, this contribution is negligible. However, for the hydrogenic-type gas, the polarizability for the q^{th} principal quantum level varies as q^6 (Ref. 5). Although this functional relationship is not exactly true for the case of argon, it does demonstrate the very strong dependence of the polarizability on the principal quantum number. This point receives added emphasis when it is realized that the $q = 21$ level with a statistical weight $g = 3200$ may be occupied for an argon plasma at $13,500^\circ \text{K}$ and 1 atmosphere pressure prior to termination of the series by the plasma microfield (Ref. 28). It should, however, be noted that although the plasma microfield restricts the occupation of the discrete levels to a finite number, it is now possible to have transitions to continuum states at energies which formerly existed below the undepressed ionization limit. As a near continuous array of discrete terminal levels has now been replaced by a continuous array, it is suggested that the effect of the plasma microfield on the species refractive index is negligible.

An attempt has therefore been made to estimate the summed effect of the excited state polarizabilities for neutral argon by applying Eq. 2.1.6 with $m = 1$ through to infinity together with the available tabulations of oscillator strength values for discrete non-resonance transitions. A total of 657 terms was obtained from the recent National Bureau of Standards compilation (Ref. 21) of most likely values, together with additional theoretical values from the calculations of Murphy (Ref. 29) and of Johnston (Ref. 30) and additional experimental values from the experiments

of Wiese et al (Ref. 79).

Comprehensive calculations of the polarizability for any one excited electronic state using this method requires a detailed knowledge of a very large number of oscillator strength values, including the contribution from discrete-continuous transitions. The present calculation can therefore at best only hope to estimate the dispersive effect due to the stronger discrete transitions in the neutral argon spectrum.

The contribution of discrete non-resonance transitions to the total excited polarizability contribution, is obtained from Eq. 2.1.6 in the form

$$(\mu_{A^*} - 1) = \frac{e^2}{2\pi m} \sum_{m=1}^{\infty} N_m \sum_{n=m+1}^{\infty} \frac{f_{nm}}{(v_{nm}^2 - v_n^2)} \left(1 - \frac{N_n}{N_m} \frac{g_m}{g_n} \right) \quad (2.1.10)$$

For a Boltzmann distribution of level populations, this equation can be rewritten as:

$$(\mu_{A^*} - 1) = \frac{N_A \lambda^2}{16\pi^3 c \psi_A} \sum_{m=1}^{\infty} \sum_{n=m+1}^{\infty} \left\{ \frac{\lambda_{mn}^4 g_n \exp(-E_m/kT)}{(\lambda_{mn}^2 - \lambda_{mn}^2)} (1 - \exp(-(E_m - E_n)/kT)) A_{mn} \right\} \quad (2.1.11)$$

where λ_{mn} corresponds to transition n to m, N_A is the neutral argon atom particle density,

$$A_{mn} = \left(\frac{f_{nm}}{\lambda_{mn}^2} \right) \left(\frac{g_m}{g_n} \right) \left(\frac{8\pi^2 e^2}{mc} \right)$$

is the Einstein coefficient of spontaneous emission and ψ_A is the partition function for neutral argon.

The calculation was performed for a number of air wavelengths in the near ultra violet, visible and near infrared regions and in particular for those wavelengths corresponding to the ruby laser, $\lambda = 6943.5 \text{ \AA}$ (Ref. 80) and its second harmonic, to the neodymium laser, $\lambda = 10,600 \text{ \AA}$ and its second harmonic and to the He-Ne laser wavelengths at 6328 \AA and 11523 \AA .

Whereas the spectral bandwidths for the ruby and helium-neon lasers are generally less than 0.1 \AA , that for the neodymium laser consists of a system of lines distributed over a 50 \AA bandwidth. Unfortunately the spectral structure of the neodymium laser output is a function of a number of laser parameters, e.g., pump energy, Q-switch mode, laser glass type and quality, cavity end reflectors, so that it is difficult to control or predict the spectral nature of the neodymium laser radiation. However, there appears to be as yet no oscillator strength data available corresponding to any dominant neutral argon transitions which fall in the spectral regions of the neodymium laser or its second harmonic. Hence the use of an average value for the wavelengths of the neodymium laser and its second harmonic is felt to be permissible.

For wavelengths shorter than $10,000 \text{ \AA}$ Wright et al (Ref. 31) have tabulated both the allowed and the forbidden transitions for neutral argon. From these tables it is apparent that the only allowed transition lying close

to any of the visible or ultra-violet laser lines is that in the 5d-4s array with an air wavelength of 3472.54 \AA . Unfortunately the oscillator strength for this transition has been neither calculated nor measured. However, Desai and Corcoran, who measured oscillator strengths for neutral argon in this spectral region (Ref. 32), have noted that the emission for this line lies at or below the noise level of their measurements such that the Einstein spontaneous emission coefficient for this transition has a value $\leq 1.3 \times 10^{-5} \text{ sec}^{-1}$ (Ref. 33). This value was therefore included in the calculation for the total excited state refractivity although a preliminary calculation indicated that its contribution at 3471.75 \AA was not large.

Although there are a large number of neutral argon transitions in the region of the He-Ne laser line at 11523 \AA , no similar tabulation exists for the transitions in the vicinity of this laser line. The results for this wavelength should therefore only be considered as tentative although none of the known transitions lie close to this wavelength.

The calculation was performed for temperatures of 10,000°K, 13,500°K, 15,000°K and 20,000 K for a plasma pressure of one atmosphere with the corresponding neutral atom partition function taken from the tabulation of Dreilishak et al (Ref. 28).

The total excited state refractive index contributions for the above mentioned laser wavelengths and plasma conditions are shown in Table 2 where the major contribution occurs at 6943.5 \AA .

For plasma conditions of 13,500°K and 1 atmosphere pressure at 6943.5 \AA , the refractivity for the excited electronic states of neutral argon is about 6.6% of the total species value or about 6.1% of the corresponding ground state value.

Figure 1 shows the total neutral argon refractivity as a function of wavelength for the stated experimental conditions which in addition to the ground state contributions, includes those either from the total of 657 non-resonance discrete transitions or from the 30 transitions of the 4p-4s array. The ground state contribution to the overall neutral atom refractivity as measured by Peck and Fisher (Ref. 22) is also shown for comparison.

It immediately becomes obvious that for wavelengths less than about 9000 \AA , the transitions in the 4p-4s array make the dominant contribution to the excited state refractivity and are responsible for the broad resonance extrema which are centered at about 8200 \AA and 9100 \AA . This is not surprising as the transitions for this array tend to fall into two wavelength groups centered on the transitions having vacuum wavelengths of 8117.5 \AA and 9125 \AA which have by far the largest ($g_A g_m$) values in their respective groups.

For longer wavelengths, the influence of a great many relatively strong near infrared transitions becomes apparent by virtue of the irregular nature of the data shown in Fig. 1. However, the fact that the shorter wavelength data appears to be continuous is purely a result of choosing the diagnostic wavelengths to be sufficiently remote from any individual transitions, i.e., $(\gamma - \lambda_{mn}) \geq 20\text{\AA}$ say, so that local resonances do not occur. (Equation 2.1.11 is by its very nature a non-continuous function of the wavelength of the incident radiation).

An interesting observation regarding the two extrema shown in

Fig. 1, is that they are not due to a single transition but to about 20 out of the total of 30 transitions in the $4p-4s$ array. In addition, these transitions all originate from the resonance levels which for an equilibrium plasma are the most highly populated of the excited states of neutral argon.

It should be possible to confirm the existence of these resonances by performing single frequency interferometry on an equilibrium plasma of known thermodynamic and ground state refractivity properties at a number of different wavelengths in the neighbourhood of these extrema. An ideal source of diagnostic radiation for such measurements could be provided by a pulsed dye laser which can be tuned to operate in this wavelength region.

If the existence of these extrema is confirmed, then it should be possible to monitor directly the population density of the rate-limiting resonance states for neutral argon. This could be achieved in a manner similar to that proposed by Measures (Ref. 34), who suggests that by performing dual frequency interferometry at wavelengths close to and relatively remote from the line center for a single transition, one can separate out the fringe shift contributions due to changes in the other unknown plasma species from that due to the single transition under observation. In the present situation, due to the broad spectral nature of these extrema, the fringe shifts at both wavelengths would contain contributions due to the transitions in the $4p-4s$ array as well as those due to the free electrons and the ground states of neutral and singly ionized argon. However, this is no obstacle to interpretation of the data as only those components due to the excited state transitions will exhibit a marked wavelength dependence over a relatively small wavelength interval. For example, at 8000\AA with $\Delta\lambda = 40\text{\AA}$, the change in the free electron refractivity is about 1%, which to a first approximation can be ignored.

Although these calculations appear to indicate that the excited states make a small but real contribution to the neutral argon refractivity for temperatures greater than 10,000 K and particularly for the ruby laser fundamental wavelength of 6943.5\AA , it was decided to omit this excited state contribution from the neutral argon refractivity. This was due to the uncertainty introduced into the calculation by the omission of a large number of unknown oscillator strength values for transitions between bound states in addition to those for discrete-continuum transitions. Rather, it was decided to use the experimental data of Peck and Fisher (Ref. 22) given by Eq. 2.1.8, to describe the total neutral argon refractivity for the shock generated argon plasma at pressure p and temperature T .

As this excited state refractivity contribution should selectively effect the experimental determination of the free electron density as obtained from the two-wavelength interferometric technique (see Section 2.3), which is primarily dependent on the fringe shift at 6943.5\AA and not on the fringe shift at 3471.75\AA , then a comparison between the measured electron density made using the ruby and neodymium lasers and the corresponding calculated values should reflect the presence of a significant excited state refractivity contribution. This comparison will be discussed in Sections 4.3 and 4.4 in the light of the present experimental measurements.

In view of the relatively small neutral argon excited state refractivity contributions to the plasma refractive index for the chosen diagnostic wavelengths, a similar calculation to estimate the effect of the excited states of singly ionized argon does not seem to be necessary. The population of the

first excited state for this species at 13,500°K is approximately 3×10^{-6} of the ground state value which is considerably smaller than for the resonance states of neutral argon. In addition, a major obstacle to such a calculation exists in that no oscillator strength data is available for the non-resonant transitions from this level, although numerous values are available for transitions between the more energetic but sparsely populated levels (Ref. 21).

The expression for the plasma refractive index to be used in the analysis of the present experimental measurements will therefore be given by Eq. 2.1.2 with the free electron term provided by Eq. 2.1.5, the neutral atom term Eq. 2.1.8 and with the ion refractivity term to be determined as described in Sections 2.2 and 2.4.

2.2 Relationship Between the Fringe Shift and the Change in the Plasma Phase Refractive Index

The fringe shift S_{12}^λ as obtained using a Mach-Zehnder interferometer is related to the change in the phase refractive indices between any two states 1 and 2, by the relationship.

$$S_{12}^\lambda = \left(\frac{L}{\lambda} \right) \left[\sum_s (\mu_s^\lambda - 1)_2 - \sum_\Delta (\mu_s^\lambda - 1)_1 \right] \quad (2.2.1)$$

where superscript λ refers to the wavelengths of the diagnostic radiation and L is the geometrical path length over which the change occurs. Expanding the summation terms in Eq. 2.2.1 into the form given by Eq. 2.1.2 and denoting the pre-shock and post shock (plasma) states by subscripts 1 and 2 respectively, the fringe shift equation now becomes

$$S_{12}^\lambda = \left(\frac{L}{\lambda} \right) \left[\left\{ (\mu_A^\lambda - 1)_2 + (\mu_I^\lambda - 1)_2 + (\mu_e^\lambda - 1)_2 \right\} - \left\{ (\mu_A^\lambda - 1)_1 \right\} \right] \quad (2.2.2)$$

where it is assumed that the preshock gas at state 1 consists entirely of neutral argon atoms.

As the component refractivities are linearly dependent on their respective densities, then Eq. 2.2.2 can be rewritten in terms of the refractivities at standard temperature and pressure (STP) to give

$$\begin{aligned} S_{12}^\lambda = & \left(\frac{L}{\lambda} \right) \left[\left\{ (\mu_A^\lambda - 1)_0 \left(\frac{\rho_2}{\rho_0} \right) (1-x_2) + (\mu_I^\lambda - 1)_0 \left(\frac{\rho_2}{\rho_0} \right) x_2 \right. \right. \\ & \left. \left. + (\mu_e^\lambda - 1)_0 \left(\frac{\rho_2}{\rho_0} \right) x_2 \right\} - \left\{ (\mu_A^\lambda - 1)_0 \left(\frac{\rho_1}{\rho_0} \right) \right\} \right] \end{aligned} \quad (2.2.3)$$

where subscript '0' denotes conditions at STP, x is the degree of single ionization, ρ is the mass density and $(\mu_A^\lambda - 1)_0$ and $(\mu_e^\lambda - 1)_0$ are given by Eqs. 2.1.8 and 2.1.5 respectively.

The expression to be used to determine $(\mu_I^\lambda - 1)_0$, the refractivity for singly ionized argon at STP, is obtained directly from Eq. 2.2.3 as

$$(\mu_I^\lambda - 1)_o = S_{12}^\lambda \left(\frac{\lambda}{L} \right) \frac{N_o}{N_{e,2}} - (\mu_e^\lambda - 1)_o - (\mu_A^\lambda - 1)_o \left\{ \frac{N_o}{N_{e,2}} \left(\left(\frac{\rho_2 - \rho_1}{\rho_0} \right) - 1 \right) \right\} \quad (2.2.4)$$

where x_2 , the degree of ionization is eliminated through use of the equality

$$x_2 = \left(\frac{N_{e,2}}{N_o} \right) \left(\frac{\rho_0}{\rho_2} \right)$$

and $N_g = 2.687 \times 10^{19} \text{ cm}^{-3}$ is Loschmidt's number. The quantities to be experimentally determined are therefore S_{12}^λ , the fringe shift between states 1 and 2, ρ_1 and ρ_2 the preshock and equilibrium plasma mass densities and $N_{e,2}$ the plasma free electron density at state 2.

In the optical region of the spectrum, the refractivities for the heavy particles (neutral atoms, ions) are effectively non-dispersive whereas the free electron refractivity varies as λ^2 . It is therefore clear from Eq. 2.2.3 that the fringe shift contribution for the heavy particles varies as λ^{-1} whereas that for the free electrons varies as λ . Hence in order to increase the fringe shift contribution due to the argon ion and consequently the sensitivity of the experimental measurements while simultaneously depressing the contribution due to the free electrons, it is essential to conduct the experiment at as short a wavelength as possible. As will be described in Sections 3 and 4, this is accomplished by employing the second harmonic of the ruby laser at 3471.75\AA which lies just below the cut-off frequency for conventional glass optics.

2.3 Determination of the Plasma Electron Density by the Method of Two Wavelength Interferometry

In order to obtain $(\mu_I^\lambda - 1)_o$ from Eq. 2.2.4 we must know in addition to the fringe shift S_{12}^λ , the values of ρ_2 and x_2 . These can be obtained from the shock Hugoniot equations for given values of the shock Mach number M_s , p_1 and T_1 on the assumption that the gas is in Saha equilibrium. However, in the presence of radiation cooling, it cannot be categorically stated that the shock generated plasma attains Saha equilibrium (Refs. 58, 59, 60). Clearly Saha equilibrium will exist if the electron density calculated via the shock Hugoniot equations is in agreement with the corresponding experimentally measured value. It is the determination of this latter value with which we are now concerned.

As discussed in Section 1.2 and 2.1, the two wavelength interferometric technique of Alpher and White (Refs. 2, 12) is capable of providing an accurate measure of the electron density for both equilibrium and non equilibrium plasmas.

Two simultaneous interferograms of the same shocked gas sample are obtained for wavelengths λ_x and λ_y as far apart as possible, with $\lambda_y > \lambda_x$ at as long a wavelength as the plasma or optical system allows. The latter requirement reflects the strong dispersive nature of the free electron refractivity where $(\mu_e^\lambda - 1) \propto \lambda^2$ in contrast to the weak dispersion of the heavy particle refractivities. By simultaneously solving Eq. 2.2.3 for wavelengths λ_x and λ_y , we have

$$N_e = \frac{\frac{N_0 \lambda_y}{(\mu_e^{y-1})_o^L} \left[S_{12} \frac{\lambda_x}{\lambda_y} \left(\frac{\lambda_x}{\lambda_y} \right) \frac{(\mu_A^{y-1})_o}{(\mu_A^{x-1})_o} \right] \left[\left(\frac{\lambda_x}{\lambda_y} \right)^2 \frac{(\mu_A^{y-1})_o}{(\mu_A^{x-1})_o} - 1 \right]^{-1}}{\left[1 + \frac{(\mu_I^{y-1})_o}{(\mu_A^{y-1})_o} \left\{ \frac{(\mu_I^{y-1})_o}{(\mu_A^{y-1})_o} - \frac{(\mu_I^{x-1})_o}{(\mu_A^{x-1})_o} \right\} \left[\left(\frac{\lambda_x}{\lambda_y} \right)^2 \frac{(\mu_A^{y-1})_o}{(\mu_A^{x-1})_o} - 1 \right]^{-1} \right]} \quad (2.3.1)$$

where it is explicitly assumed that the excited states do not contribute to either the neutral atom or the ion refractivities. The term in curly brackets in the denominator of Eq. 2.3.1 represents the difference between the ratio of the ion refractivity to the neutral atom refractivity at λ_y to that at λ_x . The resonance absorption transitions for neutral argon occur at 1048.2 \AA and 1066.7 \AA (Ref. 21) with the result that the dispersion for neutral argon is very weak in the near ultra-violet, visible and near infrared regions of the spectrum. The corresponding transitions for singly ionized argon occur at 918.8 \AA and 932.0 \AA (Ref. 21), so that the dispersion for this species can be expected to be even weaker than that for neutral argon in the same spectral region. Hence this difference term referred to above is likely to be very small. However, by taking the pessimistically large value of

$$\left\{ \frac{(\mu_I^{y-1})_o}{(\mu_A^{y-1})_o} - \frac{(\mu_I^{x-1})_o}{(\mu_A^{x-1})_o} \right\} = \pm 0.1$$

which for the wavelengths of the ruby laser (6943.5 \AA) and (3471.7 \AA) respond to about a 16% change in the ion refractivity, the denominator in Eq. 2.3.1 takes a value of (1 ∓ 0.0063) . Similarly for the wavelengths of the neodymium laser (10600 \AA) and its second harmonic (5300 \AA), this term has a value of (1 ∓ 0.0027) . It is therefore clear that this term has a negligible effect on the electron density given by Eq. 2.3.1 under normal conditions and can hence be omitted.

The expression to be used to obtain the experimental electron density from the fringe shift data is therefore given by

$$N_e = \frac{N_0 \lambda_y}{(\mu_e^{y-1})_o^L} \left[S_{12} \frac{\lambda_x}{\lambda_y} \left(\frac{\lambda_x}{\lambda_y} \right) \frac{(\mu_A^{y-1})_o}{(\mu_A^{x-1})_o} \right] \left[\left(\frac{\lambda_x}{\lambda_y} \right)^2 \frac{(\mu_A^{y-1})_o}{(\mu_A^{x-1})_o} - 1 \right]^{-1} \quad (2.3.2)$$

Two points regarding Eq. 2.3.2 call for comment. Firstly this expression is completely independent of the (as yet unknown) ion refractivity and only weakly dependent on the neutral atom refractivity through the ratio

$$(\mu_A^{x-1})_o / (\mu_A^{y-1})_o ,$$

which has a value close to unity in the optical region. By assuming this ratio to be unity, an error of 0.85% is generated in N_e for the wavelengths of the ruby laser and its second harmonic. For the neodymium laser and its second harmonic, the corresponding error of 0.2% is less significant.

Secondly, the accuracy with which N_e can be measured is dependent on the magnitude of $(\lambda_y - \lambda_x)/(\lambda_y + \lambda_x)$. For a laser (λ_y) and its second harmonic (λ_x) this term takes a value of 1/3. As $(\lambda_y - \lambda_x)$ approaches zero, then both the numerator and denominator approach zero so that the value N_e becomes highly susceptible to errors in $S_{12}^{\lambda_y}$ and $S_{12}^{\lambda_x}$. It should be mentioned that Alpher and White (Ref. 2, 12) made the additional assumption that $(\mu_A^{\lambda_y-1})_o = (\mu_A^{\lambda_x-1})_o = \text{const.}$ with the result that

$$N_e = \frac{N_o}{(\mu_e^{-1})_o} \left(\frac{\lambda_y}{L} \right) \left[S_{12}^{\lambda_y} - S_{12}^{\lambda_x} \left(\frac{\lambda_x}{\lambda_y} \right) \right] \left[\left(\frac{\lambda_x}{\lambda_y} \right)^2 - 1 \right]^{-1} \quad (2.3.3)$$

However, in their case, the wavelength separation was somewhat smaller with $(\lambda_y - \lambda_x)/(\lambda_y + \lambda_x) = 0.14$, so that this approximation is more acceptable although a price is paid in accuracy as has already been noted.

3. EXPERIMENTAL FACILITIES

3.1 Shock Tube

A detailed account of the construction and operation of the UTIAS 4" x 7" combustion driven shock tube has been given by Boyer (Ref. 35). However, several modifications and improvements were made to this facility with a view to expediting the present experiments. These are described in the following sections.

3.1.1 Shock Tube Driver Section

A number of refinements have been made in the operation of the combustion driver facility. It was noticed that the stoichiometric mixture of hydrogen and oxygen diluted by 75% of helium tended to exhibit rough combustion. This became manifest as a series of high frequency (~ 1Khz), moderate amplitude oscillations superimposed on the main pressure rise. The reason for the pressure traces given by Boyer (Ref. 35) not exhibiting these oscillations may be related to the change in length in the driver tube from the original value of 13.75 ft. to the present length of 50 in. It should be mentioned that the period of these pressure pulses corresponds closely to that of a single sound wave reflecting between the end walls of the 50 in. long combustion chamber cavity at the sound speed of the 75% helium combustion mixture (Ref. 36).

As it is conceivable that these pressure pulses might amplify into a detonation wave or alternatively damage and possibly break the ignition wire, a change to 80% helium dilution was made in view of the experiences of Nagamatsu and Martin (Ref. 37). Although this measure had the desired effect of achieving smooth combustion, it was also observed to result in a small reduction in shock Mach number for otherwise identical initial conditions together with a much increased time to peak combustion pressure, viz. 100 msec as against 10 msec.

There are several possible explanations for this reduction in performance. Firstly, the more rapid rise time at 75% helium dilution may tend to accelerate the diaphragm opening process thereby promoting more efficient shock formation. Secondly, a longer residence time for combustion, in principle, leads to higher thermal losses with a consequent drop in pressure and sound speed of the driver gas. Finally and significantly, calculations (Ref. 36) indicate that the peak combustion pressure at 80% helium dilution is about 10% less than

for 75% dilution for the same precombustion pressure.

A compromise dilution of $77\frac{1}{2}\%$ was therefore tried and found to give smooth combustion for which the risetime to peak combustion pressure was comparable to that for 75% helium dilution. Although Benoit (Ref. 36) indicates that this degree of dilution achieves a peak pressure approximately 5% less than that for the 75% dilution, a similar loss of shock tube performance was not observed.

In addition, with a view to ensuring complete combustion, the $77\frac{1}{2}\%$ dilution was partitioned into components of 5% hydrogen and $72\frac{1}{2}\%$ helium. This ensures better hydrogen-oxygen contact and more rapid combustion while simultaneously raising the post-combustion sound speed without creating any undue hazard due to the presence of an unburnt hydrogen fraction in the dump tank.

For this $77\frac{1}{2}\%$ level of helium dilution, the experimentally determined shock tube characteristic for combustion driving into argon using a single diaphragm was found to be given by $\ln(p_4/p_1) = \{0.422 M_s + 4.02\}$ for $10 \leq M_s \leq 24$, where p_4 is the peak combustion pressure, p_1 is the preshock (initial) test gas pressure and M_s is the incident shock Mach number. The ratio of p_4 to p_{mix} , the pre-combustion pressure for the above conditions, was found to have an experimental value of 6.85 ± 0.25 whereas the calculated value was about 8.05 (Ref. 36). As p_4 is initially determined by the shock requirements, the conservative value of $(p_4/p_{mix}) = 6.60$ was therefore employed in conducting the present experiments.

The other change made to the combustion system involved increasing the thickness of the tungsten heating wire used to ignite the combustion mixture from a diameter of 0.010" to 0.015" with a view to reducing the possibility of a break before, during or after a run and hence to ensure use of the wire for several runs. Initially, the 50 inch length of 0.015 in.dia. wire has a resistance of 0.61 ohms which tends to double after each run due to oxidation. The wire was usually changed after the resistance exceeded 2 ohms or after every three runs whichever comes first. For high pressure runs ($p_4 > 5000$ psi) however, the wire tended to break during combustion but without any otherwise deleterious effects on the combustion process or the facility.

In order to heat the tungsten wire to the same temperature in order to maintain smooth combustion, the voltage on the $4\frac{1}{2}\mu F$ capacitor was increased by 50% to 12.75 Kv providing an energy density of about 90 Joules per foot of 0.015" diameter wire, sufficient to make the wire glow a bright red-orange colour when tested in air at one atmosphere pressure.

A common cause of detonation is localized ignition. In the present system these conditions were observed to exist in the form of arcing at the wire terminals due to inadequate clamping pressure. This became particularly important in view of the above mentioned voltage increase. Careful redesign of the end clamps was found to be sufficient to eliminate this localized sparking.

3.1.2 Criteria for Design of the Shock Tube Diaphragms

The bursting pressure characteristics for circular scribed diaphragms

given by Boyer (Ref. 35) refer to discs of annealed stainless steel type 302 with an unsupported diameter of $6\frac{1}{2}$ inches. However, the diaphragms now used have been standardized to stainless steel type 304 with a 2B finish for which the diaphragm clamp has a clear diameter of $7\frac{1}{8}$ inches. The production of new calibration curves was therefore found to be necessary.

A series of tests using the hydraulic diaphragm bursting rig described in Ref. 35 was performed on annealed diaphragms of type 304 stainless steel having thicknesses of 0.062, 0.109 and 0.172 inches. The experimentally measured bursting pressures for the scribed diaphragms p_h was adequately described by the dimensionless relationship

$$\left(\frac{p_h}{p_t} \right) = \left(\frac{h}{t} \right)^n \quad (3.1.2.1)$$

where p_t is the bursting pressure of the unscribed diaphragm, h is the residual diaphragm thickness after scribing and t is the total diaphragm thickness. The measurements indicated a value for $n = 2.20 \pm 0.1$ for $(h/t) > 0.10$ where the error limits for n are due to a number of uncertainties, e.g., variations in material composition, degree of anneal, diaphragm wedge angle and total thickness h and also to errors in measurements of p_t , p_h and h .

The bursting pressure of the unscribed diaphragms, p_t , was found to be given by the usual relationship (Ref. 81)

$$p_t = \left(\frac{4\sigma t}{d} \right) K \quad (3.1.2.2)$$

where σ is the ultimate tensile strength for the annealed material (85000 psi for SS304), d is the unsupported diameter of the diaphragms and K is a factor which corrects for the non-ideality of the diaphragm performance due to the competing effects of work hardening and diaphragm thinning which occur during deformation just prior to bursting. Ideally K should be unity and in reality has a value close to this value. Unfortunately a universal experimental value of K was not obtained, possibly due to variations in material composition, degree of anneal, wedge angle and surface finish. Specific values of K for each diaphragm thickness are as follows:

$$\begin{aligned} t = 0.172 \text{ in}, \quad K &= 1.01 \\ t = 0.109 \text{ in}, \quad K &= 1.10 \\ t = 0.062 \text{ in}, \quad K &= 1.06 \end{aligned} \quad \left. \begin{array}{l} \text{for SS304 and } d = 7\frac{1}{8} \text{ in} \\ \text{in} \end{array} \right\}$$

For combining Eq. 3.1.2.1 and 3.1.2.2 the bursting pressure for a given scribed diaphragm is given by

$$p_h = \left(\frac{4\sigma t}{t} \right) K \cdot \left(\frac{h}{t} \right)^n \quad (3.1.2.3)$$

which when combined with the experimental values of n and K , gives a reliable prediction of diaphragm performance for $(h/t) > 0.10$.

given by Boyer (Ref. 35) refer to discs of annealed stainless steel type 302 with an unsupported diameter of $6\frac{1}{2}$ inches. However, the diaphragms now used have been standardized to stainless steel type 304 with a 2B finish for which the diaphragm clamp has a clear diameter of $7\frac{1}{8}$ inches. The production of new calibration curves was therefore found to be necessary.

A series of tests using the hydraulic diaphragm bursting rig described in Ref. 35 was performed on annealed diaphragms of type 304 stainless steel having thicknesses of 0.062, 0.109 and 0.172 inches. The experimentally measured bursting pressures for the scribed diaphragms p_h was adequately described by the dimensionless relationship

$$\left(\frac{p_h}{p_t} \right) = \left(\frac{h}{t} \right)^n \quad (3.1.2.1)$$

where p_t is the bursting pressure of the unscribed diaphragm, h is the residual diaphragm thickness after scribing and t is the total diaphragm thickness. The measurements indicated a value for $n = 2.20 \pm 0.1$ for $(h/t) > 0.10$ where the error limits for n are due to a number of uncertainties, e.g., variations in material composition, degree of anneal, diaphragm wedge angle and total thickness h and also to errors in measurements of p_t , p_h and h .

The bursting pressure of the unscribed diaphragms, p_t , was found to be given by the usual relationship (Ref. 81)

$$p_t = \left(\frac{4\sigma t}{d} \right) K \quad (3.1.2.2)$$

where σ is the ultimate tensile strength for the annealed material (85000 psi for SS304), d is the unsupported diameter of the diaphragms and K is a factor which corrects for the non-ideality of the diaphragm performance due to the competing effects of work hardening and diaphragm thinning which occur during deformation just prior to bursting. Ideally K should be unity and in reality has a value close to this value. Unfortunately a universal experimental value of K was not obtained, possibly due to variations in material composition, degree of anneal, wedge angle and surface finish. Specific values of K for each diaphragm thickness are as follows:

$$\begin{aligned} t = 0.172 \text{ in}, \quad K &= 1.01 \\ t = 0.109 \text{ in}, \quad K &= 1.10 \quad \} \text{ for SS304 and } d = 7\frac{1}{8} \text{ in} \\ t = 0.062 \text{ in}, \quad K &= 1.06 \end{aligned}$$

For combining Eq. 3.1.2.1 and 3.1.2.2 the bursting pressure for a given scribed diaphragm is given by

$$p_h = \left(\frac{4\sigma t}{t} \right) K \cdot \left(\frac{h}{t} \right)^n \quad (3.1.2.3)$$

which when combined with the experimental values of n and K , gives a reliable prediction of diaphragm performance for $(h/t) > 0.10$.

3.1.3 Shock Tube Driven Section

Modifications to the driven section were primarily centered around improving the shock tube vacuum with a view to obtaining a high purity test gas sample in the test section prior to shock arrival.

Through the introduction of a 6 in. dia. vacuum diffusion pump between the shock tube and Roots blower vacuum pump (see Ref. 35), a vacuum and leak-outgassing rate of about 1×10^{-5} mmHg and 1×10^{-5} mm Hg/min. respectively were obtained after a 24 hour pumpdown period. The relatively long pumpdown period is due to the large volume of the shock tube dump tank (35.4 cu.ft.) in relation to the shock tube channel (9.6 cu.ft.) together with the low conductance of the shock tube which connects the dump tank to the vacuum pumps.

If desired the vacuum and combined outgassing-leak rate could be improved by about an order of magnitude by extending the pumpdown period from 2 to 3 days. However, as events transpired, a high degree of test-gas purity was not required particularly as the argon test gas was intentionally seeded with approximately 0.4% of molecular hydrogen by pressure for reasons to be discussed in Section 4.2.

The argon and hydrogen test gases used in these experiments were both of the 'Linde High Purity Grade' type. The argon has a manufacturers minimum purity of 99.996% by volume with a typical trace gas analysis of less than 15 ppm of nitrogen, 7 ppm of oxygen and 5 ppm of carbonaceous matter together with a dew point of better than -71°F. Similarly the hydrogen has a quoted purity of 99.99% by volume with less than 100 ppm of nitrogen and 10 ppm of oxygen together with a dew point better than -71°F.

The hydrogen was first admitted into a calibrated reservoir to a predetermined pressure and then released into the shock tube. The argon test gas was then added directly to the shock tube until the desired total initial pressure was attained.

3.1.4 Measurement of the Incident Shock Wave Properties

The measurement of T_1 and p_1 , the initial (preshock) test gas temperature and pressure respectively and U_s the incident shock velocity is in principle most straightforward and has already been discussed by many authors.

However in the present experiments, a great deal of care had to be taken to reduce errors in the measurement of these parameters, particularly as they define the boundary conditions for calculating the shock properties from the shock Hugoniot equations. For example, a 1% error in the measurement of U_s generates a 4% error in the calculated value of N_e , the electron density for a $M_s = 20$ shock into 1 mm Hg of argon.

(i) Initial Preshock Temperature, T_1 :

The initial temperature was measured by means of a mercury bulb thermometer calibrated in 0.2°C intervals which was inserted into a 2 in. deep x 1/4 in.dia. oil filled port located close to the test section. It was assumed that the test gas rapidly comes into a state of thermal equilibrium with the shock tube in the time period between test gas admission and shock initiation (~ 5 min). Values for the initial temperature were interpolated to the nearest

0.1°C with an estimated overall error of $\pm 0.1^{\circ}\text{C}$. This corresponds to a maximum error of $\pm 0.03\%$ in the absolute value of the initial temperature.

(ii) Initial (Preshock) Pressure, p_1

The initial pressure p_1 was monitored by means of an oil manometer based on the design of Hayward (Ref. 38), which covers the pressure range from 0.1 to 40 mmHg.

The manometer consists of a 50 cm long x 1-cm i.d. U-tube, which is connected at one end to an oil reservoir and at the other end to the vacuum system via a length of flexible vacuum tubing. By rotating the manometer through 120° about a horizontal axis, the oil (Dow Corning type 704 diffusion pump oil) is allowed to collect in the reservoir and is vigorously agitated for several minutes so as to induce rapid degassing. Hayward has shown that this type of manometer gives a much better correlation with a McLeod gauge than the more conventional fixed U tube oil manometer having a cross tube with stopcock.

Dow Corning Corp. (Ref. 39) quote a specific gravity of 1.07 at 25°C for DC704 oil with a corresponding temperature coefficient of $9.5 \times 10^{-4}/^{\circ}\text{C}$. A laboratory check on the specific gravity of the sample used produced a value of 1.069 at 25°C which was therefore employed in the present measurements together with the temperature coefficient given above.

The initial preshock pressure p_1 in mmHg is obtained from the difference in oil levels H mm oil by the relationship

$$p_1 = H \left(\frac{\rho_{\text{oil}, T_1}{}^{\circ}\text{C}}{\rho_{\text{Hg}, 0}{}^{\circ}\text{C}} \right) \text{ mmHg}$$

where $\rho_{\text{Hg}, 0}{}^{\circ}\text{C} = 13.595$ is the specific gravity of mercury at 0°C and $\rho_{\text{oil}, T_1}{}^{\circ}\text{C} = 1.069 + (25 - T_1) \times 9.5 \times 10^{-4}$ is the specific gravity of the oil at $T_1{}^{\circ}\text{C}$ where T_1 is the laboratory air temperature in the neighbourhood of the manometer.

With a view to ensuring an accurate measurement of p_1 , the manometer was fitted with a viewing cursor and back view mirror so as to provide a horizontal reference mark and to avoid a parallax reading error. In addition the vertical position of the manometer was checked from time to time with a plumb line.

Originally it was only intended to use the oil manometer for pressures down to about 2 mmHg and to use a McLeod gauge (5 mmHg to 1 μHg) for lower pressures down to 0.3 mmHg. However, in the range of overlap of the two gauges, the McLeod gauge gave readings which were about 3% higher than those for the oil manometer. This was initially thought to be due to a poor reference vacuum in the isolated limb of the manometer but was ruled out after leak testing the manometer. In addition, the vapour pressure of the DC 704 oil is about 2×10^{-8} mmHg at 25°C (Ref. 39) and is therefore not a contributing factor to this difference.

In the absence of any obvious fault in the oil manometer, the error was therefore ascribed to the calibration of the McLeod gauge (Stokes Model No. 276-AA). Consequently all p_1 measurements were made on the oil manometer with the main source of error considered to be that due to the visual reading.

of the oil levels; this was estimated to be ± 0.1 mm of oil which at $p_1 = 0.3$ mmHg corresponds to a maximum random error of $\pm 2\frac{1}{2}\%$.

However, in order to attain these limits of accuracy at low p_1 values, the oil manometer should be isolated for at least 10 minutes after admission of the test gas before H is read in order to allow the oil adhering to the tube walls to drain back through the meniscus. A 'settling' reading error between the left and right hand limbs is thereby avoided.

(iii) Incident Shock Velocity, U_s

The incident shock velocity is obtained by the usual method of measuring the time interval between shock arrival at two axially displaced pressure sensitive detectors. The detectors are separated by 609.6 ± 0.1 mm and located at points which are equal distances upstream and downstream of the centre of the test section windows (see Fig. 2). The piezo-electric shock detectors (Atlantic Research LD 25 Blast Pressure Transducers) are flush mounted and have 6 mm dia lead zirconate titanate elements covered with a thin translucent layer of plasticized epoxy resin. The output of these gauges is approximately $0.15V/\text{psi}$.

The signals from the pressure detectors are taken directly via short leads to battery-driven emitter-follower units, having unit amplification and $1/10\mu\text{sec}$ risetime and then to the start and stop inputs of a $\pm 1/10\mu\text{sec}$ resolution electronic timer (Hewlett Packard Universal Counter 5325A). This counter-timer has separate variable triggering level capability for each channel so that variations in sensitivity between gauges can be accommodated. However, wherever possible matched gauges were used so as to reduce both temporal and spatial errors incurred in measuring the shock velocity.

The finite size (6 mm dia) of the piezo-electric elements introduces a maximum uncertainty of ± 6 mm into the distance separating the gauges. However, it was considered that by using matched gauges, this uncertainty could be reduced to ± 3 mm which corresponds to $\pm 1/2\%$ uncertainty in the gauge separation.

The risetime of the output waveform of these gauges in response to the frozen shock front pressure jump is generally of the order of $1\mu\text{sec}$ as illustrated by the lower trace of oscillogram (b) in Fig. 3. The first 'ring' of these gauges has a risetime of about $1/2 \mu\text{sec}$ and an amplitude of about 60% of the total pressure rise. The separate channels of the timer are therefore set to trigger at 50% of the anticipated voltage rise for the frozen shock pressure rise. This introduces a maximum uncertainty of $\pm 1/2 \mu\text{sec}$ into the time interval measurement which in a typical period of $100 \mu\text{sec}$ constitutes a random error of $\pm 1/2\%$.

Hence the temporal uncertainty of $\pm 1/2\%$ due to the finite rise time of the gauge combined with the spatial uncertainty of $\pm 1/2\%$ introduces a total possible random error of $\pm 1\%$ into the measurement of the shock velocity. Check measurements made using two pairs of similarly displaced gauges with a similar counter produced discrepancies between the two readings of the order of $1/10 \mu\text{sec}$ indicating that the $\pm 1\%$ error referred to above is somewhat pessimistic.

A problem encountered with these pressure gauges at an early stage in the project is illustrated by the apparent precursor profile in oscillogram (a) of Fig. 3 which tended to cause the various electronic units to pre-trigger.

As strong shocks into argon are known to produce significant photon and

electron precursors (Ref. 40), it was suspected that the precursor signal monitored by the pressure gauges was due to one or both of these aforementioned sources.

In the first instance the translucent epoxy resin covering the gauge was given an additional covering of transparent silicone (General Electric RTV) rubber. This had no effect in blocking the precursor signal suggesting that electron leakage to the gauge elements was not the cause. However, a similar film of black silicone rubber completely blocked this precursor as illustrated by oscillogram (b) in Fig. 3, suggesting that the precursor was due solely to the photon flux coming from the strongly radiating equilibrium region behind the shock front. This is not surprising as it is well known that the piezo-electric effect is always accompanied by the pyro-electric effect in which an electric charge is produced at crystal surfaces exposed to thermal radiation (Ref. 31).

The general consensus in the literature concerning the precursor phenomenon is that for strong shocks into inert gases the observable precursor electron density is produced by photoionization (Ref. 40) whereas for relatively weak shocks, e.g., $M_s < 10$ into argon, the observed precursor electrons are now thought to be due to electron diffusion (see Refs. 40, 42, 43) which for conditions of high Mach number becomes masked by the photoionization process.

It is felt that some attention should be paid to the effect of shock attenuation both on the shock velocity measurement and on the plasma properties behind the shock front.

For shock Mach numbers from 17 to 24 and initial pressures from 0.3 to 3 mm Hg, the shock front attenuation in the region of the test section was very low being typically 1/3% per foot of the 7 in. x 4 in. shock tube. The attenuation as monitored by several velocity measurements in the test section region was generally so low as to be less than the uncertainty in the measurement of the shock velocity itself which has been shown to be of the order $\pm 1\%$.

As will be indicated in Section 4, the ionization relaxation region from the shock front to conditions of Saha equilibrium is usually of the order of 10 to 20 mm so that the effect of attenuation on the shock properties over this distance can be neglected in view of the attenuation figures given above.

3.2 Optical Diagnostics and Recording Equipment

The description of the optical system is broadly divided into areas dealing with the laser light source, the interferometer itself and finally the photographic recording system.

3.2.1 Laser Light Source

Dual-frequency lasers have been employed by a number of authors to observe various plasma phenomena either by interferometric or schlieren techniques (Ref. 44 to 49).

The dual frequency laser employed is a TRG 10⁴A system, which is giant pulsed by means of an integrally-mounted Pockels cell Q-switch and is capable of operating either as a ruby or a neodymium doped glass laser by suitable choice lasing element and cavity end reflectors. The ruby laser operates at a wavelength of 6943.5 Å at 24°C (Ref. 80) with a spectral bandwidth of less than 0.1 Å and when Q-switched produces a 30-MW pulse of 15-nsec duration. Similarly the neodymium

laser operates at 10600\AA with a bandwidth of about 50\AA for which the Q-switched power and pulse duration are 20-MW and 15-nsec, respectively.

The second harmonic generator for the ruby laser consists of a critically oriented crystal of potassium di-hydrogen phosphate (KDP) which is mounted in an oil-filled cell attached directly to the output end of the laser cavity. Power generation for this process is typically 5 to 10% efficient for the 3-cm long crystal and produces coherent radiation at 3471.75\AA , which is both parallel to and concurrent with the incident laser radiation. The spectral bandwidth of the second harmonic of the ruby laser is typically 0.05\AA or less. Similarly an appropriately cut KDP crystal is used to achieve second harmonic generation of the neodymium laser output at 5300\AA with a bandwidth of less than 25\AA .

A certain measure of care should be taken in the adjustment and use of these second harmonic generators. Although the fundamental and second harmonic beams are parallel, the second harmonic beam becomes displaced from the axis of the fundamental due to double refraction within the KDP (Ref. 50). For both the ruby and neodymium lasers, the angular displacement of the second harmonic in KDP is approximately 1.77° (Refs. 50, 51), which for the 3-cm path-length crystal currently employed, corresponds to an output beam displacement of 0.92 mm. It is therefore clear that when the dual frequency is used to illuminate a schlieren system, the laser should be arranged so that the axes of both the fundamental and second harmonic beams intersect the schlieren knife edge.

The efficiency of second harmonic generation is critically dependent on the orientation of the KDP crystal with respect to the incident laser beam (Ref. 52) necessitating careful adjustment. Second harmonic generation is also strongly temperature dependent (Refs. 52, 53) such that small changes in the temperature of the KDP induced by variable laboratory conditions or by frequent laser operation can result in a large reduction in second-harmonic power conversion. Ideally this unit should be contained in a thermostatically controlled environment. For second-harmonic generation by the ruby laser (Ref. 53) and the neodymium laser (Ref. 52) in KDP, the temperature gradients for the phase matching angle are $46\text{arcsec}/^\circ\text{C}$ and $33.6\text{ arcsec}/^\circ\text{C}$ respectively.

In the field of optical plasma diagnostics, the advantages of the pulsed laser over the more conventional spark or exploding wire light are as follows:

- (i) The short pulse duration of the Q-switched laser, generally from 10 to 30 nsec, is about an order of magnitude shorter than for thermal sources of adequate intensity. For the laser, this results in excellent shock front and relaxation zone definition when photographic recording is employed.
- (ii) The high intensity laser radiation is ideal for discriminating against plasma radiation particularly when employed in conjunction with a combination of spatial and spectral filters. However, care must be taken to ensure that the spatial power density of the laser radiation is not sufficient to cause breakdown of the transmission or reflection media. If the beam is brought to a sharp focus either in air or some other gaseous system, local plasma formation may occur resulting in a loss of usable laser power due to absorption. In the case of mirror and filter surfaces or transmission media such as absorption filters, lenses, windows, etc., permanent radiation damage can occur.

(iii) The high degree of spectral (temporal) coherence of the laser output makes for excellent wavelength definition e.g., the ruby laser wavelength at 24°C is 6943.5Å (Ref. 80) with a bandwidth of 0.1Å when resonant cavity end reflectors are used. With a white light source, an acceptable degree of monochromaticity can be obtained by means of interference filters but at the expense of a large drop in intensity.

As discussed in Section 2.1, it is necessary for the laser wavelength to be remote from any absorption lines or bands of the transmitting medium under investigation, in order to avoid the effects of anomalous dispersion or absorption. However, in certain circumstances, these effects can be utilized to selectively monitor the populations and behaviour of specific internal states, particularly those involved in transitions which control a given relaxation or reaction process.

(iv) The ability of the pulsed laser to operate over a wide range of wavelengths from the near ultra-violet (3471Å) to the near infrared (10600Å) makes it an ideal light source for plasma interferometry. This laser therefore operates over the full spectral bandwidth of the present optical system. The second harmonic of the ruby laser at 3471Å lies just below the cutoff frequency of conventional glass optics whereas the fundamental of the neodymium laser at 10600Å lies at the long wavelength sensitivity limit of currently available photographic emulsions.

The two-wavelength plasma interferometry techniques of Alpher and White (Ref. 2) for measuring electron density, requires a long wavelength light source operating simultaneously at two different wavelengths (see Section 2.3). This role is ideally met by the neodymium laser and its second harmonic generator operating simultaneously at 10600Å and 5300Å.

For the observation of changes in mass density a short wavelength source is required (see Section 2.2) and is accomplished by use of the ruby laser second harmonic at 3471Å.

(v) By the nature of its formation, the laser beam is highly unidirectional, being in the form of a narrow near parallel beam with a divergence of a few milliradians such that a system of condensing optics is not necessary.

(vi) Due to the monochromatic and unidirectional state of the laser beam, it can (in principle) be focussed down to a diffraction limited spot. The laser is therefore an ideal source for use in schlieren photography as the sensitivity of this technique is an inverse function of source size (Ref. 82).

However, plasma formation and knife edge damage may occur once the laser power exceeds some critical value. Also, fine control of the small source image on the knife edge requires an extremely fine degree of control.

(vii) The high degree of spatial and temporal coherence of the laser beam makes it an ideal interferometer light source. When a white light (thermal) source is used to illuminate a Mach-Zehnder type interferometer,

it is necessary to path length match the two beam paths to within half a wave ($\lambda/2$) if a fringe field of high contrast is to be obtained. However, with the laser, this requirement can be relaxed.

If the bandwidth of the laser output is $\Delta\lambda$ for laser radiation of wavelength λ , then it can be easily shown by a classical wave optics argument that the allowed path length mismatch over which the two beams become $\lambda/2$ out of phase is given by $\lambda^2/2\Delta\lambda$. For the ruby laser operating at 6943\AA with a spectral bandwidth of 0.1\AA , this means that the path length of the two beams must not differ by more than $2\frac{1}{2}$ cms if high fringe contrast is to be obtained. The neodymium laser operating at 10600\AA has a bandwidth of about 50\AA so that in this case a path length mismatch of only 0.1 mm is allowed.

However, the direct use of the laser beam does carry certain disadvantages. Firstly, the spatial or transverse modes of the laser beam result in non-uniform illumination of the system under investigation unless spatial mode selection has been employed usually resulting in a reduction in beam intensity. Secondly, due to the coherent nature of the laser radiation, small imperfections and dust particles in the optical system tend to generate a system of diffraction rings which are clearly visible in the photographic plane. Finally, numerous sets of unwanted fringes tend to form by interference between the many optical surfaces in the system all of which become visible in the photographic plane. As will be described in Section 3.4, these difficulties can be eliminated by spoiling the phase coherence of the laser beam by transmission through a diffuser, which in effect becomes the interferometer light source.

3.2.2 Electronic Operation

The operation of the laser as the shock tube-interferometer light source is complicated by the fact that the lasing elements must be flash lamp pumped for a fixed period of time prior to Q-switching in order that the required population inversion is attained.

The Pockels cell Q-switch is arranged to open at a time when the flash lamp output is just beginning to decay. If the Pockels cell is opened at an earlier time, then in addition to the required giant pulse, a series of normal mode pulses will be obtained, as the quarter-wave voltage is re-applied to the Pockels cell over a period of about 1 msec. This will result in a number of undesired interferograms being super-imposed on the desired interferogram of the shock phenomenon under investigation. Alternatively, if the Pockels cell is opened at a later time, then a much weaker giant pulse will be obtained (Ref. 54). The flash lamp pumping times for the ruby and neodymium lasing elements as used in the TRG 104A laser system are $950 \pm 25 \mu\text{sec}$ and $800 \pm 20 \mu\text{sec}$ respectively. The $800 \mu\text{sec}$ delay period for the neodymium laser provides a giant pulse which is just sufficient for interference fringe photography but which subsequently allows the laser to free run in normal mode operation. This effect manifests itself as a loss in fringe resolution rather than as a series of multiple exposures as can be seen in the interferogram produced by the neodymium laser shown in Fig. 15(ii). However the second harmonic generation process varies as the square of the fundamental laser pulse power so that these normal mode pulses are too weak to generate a perceptible level of second harmonic radiation. This accounts for the relatively 'noise' free interferogram produced

by the second harmonic shown in Fig. 15(i). Fortunately the ruby laser can be Q-switched after a longer delay period ($\sim 950 \mu\text{sec}$) without incurring a serious loss in giant pulse power but where the flash radiation has decayed to a level which is below threshold for normal mode laser operation.

Hence a certain knowledge of the shock velocity and attenuation is required prior to each shock run in order that the laser flash lamp can be arranged to trigger at the appropriate time prior to shock arrival in the test section. A schematic of the system by which this is achieved is shown in Fig. 2. Shock arrival at pressure gauge 1 triggers the delay generator which after the elapse of the delay period triggers the flash lamp capacitor bank. The delay-generator period plus the flash lamp pump period is therefore equal to the time the shock front takes to travel from detector 1 to the centre of the test section.

The Pockels cell Q-switch is similarly activated via a delay circuit initially triggered by shock detector 2. The delay period in this case is arranged to be such that the Pockels cell opens when the shock front is in the desired position in the test section aperture. The delay generator for the Pockels cell is conveniently triggered by the synchronized output signal of the 'start' channel of the counter timer.

3.2.3 Mach-Zehnder Interferometer

The construction and operation of the 9 in. dia. aperture Mach-Zehnder interferometer has been described by Hall (Ref. 55). The adjustment procedure for obtaining and focussing the fringes, which is essentially the same as described by Hall but with small refinements and modifications resulting from the installation of the pulsed laser light source, will be described in the following section (3.2.4).

A scale drawing of the interferometer is shown in Fig. 4. The central body of the interferometer is formed by a 3/8 in. thick welded U-shaped box frame structure. The projections at either end supporting the parabolic collimating and condensing mirrors are canvas covered to prevent dust and air currents from entering the interferometer.

During operation of the interferometer, it was found that small changes in the laboratory temperature had a marked effect on the fringe settings. The small rise in the laboratory temperature generated by the electronic equipment used in the shock tube experiments was found to have a considerable effect on the setting of the focus, orientation and spacing of the fringes during the 4 to 5 minute interval between the taking of the no-flow and flow interferograms.

Further investigations showed that the steel shell of the interferometer was expanding or contracting almost instantaneously in response to these small changes in the laboratory air temperature. Temperature changes of the order of $1/100^\circ\text{C}$ were found to induce changes in the interferometer setting sufficient to generate movements of the order of $1/10$ fringe at 3471\AA .

By lagging the outside of the interferometer shell with 1 in. thick foam sponge, the response time of the interferometer to temperature changes was increased from about 30 seconds to about 10 minutes thereby providing an adequate delay period in which to conduct the shock tube-interferometer experiments. Additional precautions involved placing non-interferometric quality windows over the entry and exit parts of the interferometer and enclosing the

optical paths between the shock tube test section and interferometer with foam sponge tubes with a view to preventing the entry of both dust particles and air currents into the interferometer.

3.2.4. Adjustment and Operation of the Interferometer

The laser system, the interferometer, the test and compensating chamber sections and the camera are all initially centered and co-aligned by means of a helium-neon laser as shown in Fig. 5(a). The purpose of the pentagonal prism is to ensure that the optical axis of the helium-neon laser effectively coincides with that of the ruby/neodymium laser.

As the position of the test section windows is fixed, all other components in the system including the compensating chamber must be positioned with respect to the test section aperture. The optical axis of the interferometer is arranged to be perpendicular to the shock tube axis by adjusting the various system components until the reflection of the laser beam from the test section windows is returned to the laser cavity.

As discussed in Section 3.2.1, accurate path length matching of a two beam interferometer is not necessary when using a laser light source having a long coherence length. However, this leads to the undesirable effects of laser mode structure, spurious fringes and dust generated diffraction patterns being visible in the photographic plane. These effects can be eliminated by passing the laser beam through a diffuser which becomes in effect a light source of finite size. The spatial modes of the laser beam become smeared out resulting in uniform illumination of the test section whereas the diffraction rings and the fringes are effectively eliminated due to the reduced spatial coherence of the beam transmitted by the diffuser. The diffuser is therefore located at the focus of the collimating optics of the interferometer, which in this case is a 60 in. focal length parabolic mirror (see Fig. 4). As a result of this expedient, it now becomes necessary to path length match the interferometer according to the procedure described by Hall (Ref. 55).

Path length matching is initially achieved using a high pressure mercury-vapour lamp light source together with a condensing lens and source slit as shown in Fig. 5(b) (see Ref. 55 for details concerning adjustment of interferometer optics*). Once fringes are visible on the camera screen, the central order fringes can be located using a hand spectroscope. By imaging three or four horizontal fringes onto the vertical spectroscope slit, oblique fringes are observed in the spectroscope. Beam splitter 1 (see Fig. 4) is then translated until the fringes in the spectroscope become horizontal. These are then the central order fringes where the two optical paths of the interferometer are equal for

* Hall (Ref. 55) omitted to mention in his procedure that after path length matching of the interferometer by translation of beam splitter 1 as described in Section 3.2 of Ref. 55, the two beams are no longer exactly superimposed. This therefore necessitates further adjustments of mirrors 1 and 2 as described in Section 3.1 of Ref. 55 although this iterative procedure rapidly converges to point where high contrast monochromatic fringes can be seen.

all wavelengths to within a distance of the order of one wavelength.

Both the virtual fringes focussed in the test section and the image of the test section are then brought to a real focus on the camera screen by use of a large diffuse light source (see Ref. 55 for procedural details). This conveniently takes the form of a domestic tungsten lamp as shown in Fig. 5 (d).

The pulsed (ruby or neodymium) laser is then centered and aligned with the optical axes of the system using a helium-neon laser and pentagonal prism as shown in Fig. 5(e).

The optical system as employed in the dual frequency laser interferometer experiments is shown in Fig. 5(f). The 1-cm dia. dual-frequency laser beam is reduced to a spot of about 5-mm dia. on a double sided diffuser by means of a weak single component lens. The diffuser was produced by grinding both faces of a microscope slide with a 10μ alumina or carborundum grit. The effective source size was then defined by a 5-mm dia. stop affixed to the output side of the diffuser (see Fig. 5(f)).

Although use of this diffuser resulted in a considerable reduction in the intensity of the interferometer beam, it was still found to be sufficient to activate 300 ASA panchromatic emulsions at 6943\AA while simultaneously providing adequate discrimination against the argon shock plasma radiation.

In principle the finite size of the source aperture tends to degrade the degree of collimation of the interferometer beam and also to limit the number of fringes visible in the plane of focus. For the present system, the 5-mm diameter aperture corresponds to an interferometer beam divergence of about 0.1° which over the 4.010-in. width of the shock tube path length, results in a limiting spatial resolution of about 0.01 in. Similarly the number of visible fringes, given by $1/\theta^2$ (Ref. 56), where θ is the interferometer divergence half angle, is of the order of 10^5 . It is therefore clear that the finite size of the diffuser light source does not constitute a real limitation on the use of this system in the present circumstances.

3.2.5 Test Section and Compensating Chamber Windows

The 8 in. dia. aperture x 3-3/4 in. thick test section and compensating chamber windows were manufactured from Schott BK7 optical quality glass and were polished flat so that the 8 in. diameter transmitted wavefront of each window was flat to $\lambda/4$ at 6328\AA with wedge angles not exceeding 1 sec of arc.

The windows were mounted so as to provide a disturbance free flow to the shock wave. However, during manufacture, the inner edge was given a 45° x $1/8"$ wide bevel as a precaution against chipping. Although this depression did not generate any interferometrically observable flow disturbances, the flow stagnation in this region had the effect of causing severe erosion giving the glass surface a sand blasted appearance. This effect was satisfactorily eliminated by filling the bevel in with flexible type of epoxy resin. In order to facilitate removal of the windows from the frames, the bevel surface was treated with an anti-bonding agent so that the epoxy resin only adhered to the window frames.

A serious problem with these test section windows as with a previous pair of rectangular aperture windows (Ref. 35) involved the appearance of small

cracks originating from the re-entrant corners of the 'T' shaped cross section of the windows. These cracks were found to be caused by the application of uneven clamping pressure rather than by shock wave pressure loading. Although etching of the re-entrant corner region with hydrofluoric acid is known to remove surface microcracks from which these cracks originate, optical laboratories were not prepared to perform this work in view of the proximity of the interferometric quality surfaces. Future window designs have therefore abandoned the 'T' shaped cross section support mounting for a bevel edged support format.

3.2.6 Interference Fringe Photography

The camera used for performing two wavelength interferometry is shown in plan view in Fig. 4 and schematically in Fig. 5(f).

The interferometer beam is brought to a point focus at the iris diaphragm which acts as a stop for the uncollimated plasma radiation. The image of the test section is then focussed onto the photographic plane by an 80 cm focal length converging meniscus type spectacle lens located just behind the iris diaphragm.

An aluminized beam splitter was found to be adequate for separating the two beams although in circumstances of low intensity the use of a colour selective dichroic beam splitter would be more advantageous. Narrow band interference filters centered on the respective laser wavelengths provide further discrimination against the plasma radiation. It is worth noting that in none of the experiments to be described in Section 4, was the plasma radiation sufficiently intense as to be observed on the interferograms. This contrasts sharply with the experience of Alpher and White (Ref. 2) who employed a spark light source to perform two wavelength interferometry on shock generated argon plasmas.

Due to the dispersive nature of the camera lens, care had to be taken to ensure that the photographic emulsion was correctly positioned for each of the four laser wavelengths employed in these experiments. Precise focussing of the centre of the test section in the photographic plane was accomplished by mounting a grid of 0.010 in. diameter wires on both sides of the test section windows. A sharp focus of the test section was then obtained by moving the camera viewing screen to a point midway between the position of focus for the two sets of wires. As these wires were also used as reference markers from which the fringe shifts were measured, care was taken to ensure that the wires lay either parallel to or perpendicular to the shock tube axis. For the present optical system, the depth of field was sufficiently large that both sets of wires remained in reasonably sharp focus when the camera was focussed onto the centre of the test section.

Eastman Kodak RS Panchromatic (650 A.S.A.) emulsion on 0.007 in. thick estar sheet base was found to provide good response to the laser radiation at 3471 Å, 5300 Å and 6943 Å when processed in Kodak D19 developer.

Interference fringe photography at 10600 Å, the wavelength of the neodymium laser, presents more of a problem. Eastman Kodak I-Z spectroscopic plates for use in the near infrared region were initially used in the unsensitized condition but failed to give a sufficiently dense image. However when sensitized in chilled ammonia solution immediately prior to use according to the prescription of Pope and Kirby (Ref. 57), the speed of the I-Z emulsion is increased by a factor of about 400 which was more than adequate for the purposes of the present experiments.

A final check on the interference fringe field setting for the visible and ultraviolet laser wavelengths was made immediately prior to a shock run using Polaroid (3000 A.S.A.) positive print film thereby ensuring the satisfactory functioning of the optical - electronic system.

3.3 Data Analysis

The procedure adopted for extracting the fringe shift data from the flow and no-flow interferograms is described in Appendix A. However there remains the problem of making a judgement with regard to the location of the centre of any given fringe.

Preliminary tests with a microdensitometer showed that the dark fringes gave relatively sharp extrema which were easy to locate. Due to the over-exposure of the bright fringes, these fringes become considerably broadened such that the corresponding dark fringes in the limit of very high intensity, tend to become well defined thin lines.

However a sufficiently accurate location of the dark fringe centres was obtained by enlarging the interferograms by a factor of 10 and making a direct visual judgement of fringe location. The enlargements were made on Kodak 1594 Aerial Mapping Paper which maintains a high degree of dimensional stability after processing. It also has a matt (i.e., non-glossy) finish which makes for easy visual interpretation.

The location of the dark fringe centre lines from the positive enlargements were made to an estimated accuracy of less than ± 0.2 mm. This corresponds to a maximum error of ± 0.04 fringes at 3471 \AA and 5300 \AA for a minimum fringe spacing of 10 mm and ± 0.02 fringes at 6943 \AA and 10600 \AA for a minimum fringe spacing of 20 mm.

4. EXPERIMENTAL MEASUREMENTS, RESULTS, DISCUSSION AND CONCLUSIONS

4.1 Introduction

The structure of the relaxation, equilibrium and recombination regions behind strong shocks into argon has already been examined both experimentally and theoretically by Bershader and his co-workers (Refs. 58, 59, 60). Hence only a brief qualitative description of the non-equilibrium processes is given here in order to familiarize the reader with the context of the present experiments.

Figure 6(i) shows typical fringe shift profiles behind a strong shock into argon for both the laser fundamental (λ) and second harmonic ($\lambda/2$) wavelengths. The positive fringe shifts across the shock front is due to the compression of the neutral atom where the shift for the laser second harmonic is approximately twice that for the fundamental wavelength due to the inverse linear dependence of the heavy particle fringe shift on wavelength (see Sect 2.2.3). On approaching equilibrium there is a rapid increase in the free electron concentration, sufficient to produce a large negative fringe shift particularly at the laser fundamental wavelength; this is due to the linear dependence of the free electron fringe shift on wavelength (see Eq. 2.1.5 and Eq. 2.2.3).

Figure 6(ii) demonstrates the two temperature nature of the incubation zone prior to equilibrium where the neutral atoms are initially brought to a relatively high translational or 'frozen' temperature immediately behind the

shock front. This gas of highly energetic neutral atoms then acts as an energy source both for the ionization process and for the thermalization of the free electrons.

Finally Fig. 6(iii) illustrates in terms of the changes in the degree of ionization the various stages of non-equilibrium which exist behind a strong shock moving into an inert gas. Regime I (in the nomenclature of Ref. 58) is the region in which ionization occurs through the relatively inefficient atom-atom collision process in the absence of a significant concentration of free electrons. Eventually, in Regime II, the free electron concentration becomes such that inelastic electron-atom collisions dominate the reaction and the degree of ionization approaches a maximum corresponding to Saha equilibrium (Ref. 58). The onset of Regime III, at a point just prior to Saha equilibrium is characterized by a strong emission of radiation (Refs. 59, 60) which results in plasma cooling and hence in electron-ion recombination. This effect is illustrated in Fig. 6 by the slow rise in the fringe shifts and the corresponding fall in the plasma temperature and degree of ionization.

4.2 Experimental Measurements

4.2.1 Flow Disturbances

An initial series of shock experiments performed in pure argon were consistently plagued by a complex system of flow disturbances of wavelength and amplitude sufficient to make accurate interpretation of the interferograms extremely difficult. Although present on all the interferograms of this series, identical wave geometry was not reproducible from run to run for otherwise identical boundary conditions. Typical interferograms shown in Fig. 7 for the ruby laser and second harmonic wavelengths clearly do not exhibit the stable behaviour anticipated in Fig. 6(i).

Inspection of Fig. 7, especially the interferogram for 6943 \AA indicates the existence two opposing symmetrically displaced transverse waves with a region of confluence in the centre. In addition the visible non-planarity of the shock front appears to be directly related to this same system suggesting that the transverse waves are weak forward moving oblique shocks. It is interesting that no references to any such flow disturbances were made either by Alpher and White (Ref. 2) or by Bershadet al (Refs. 58, 59, 60) both groups of which performed space resolved optical interferometry on ionized argon shocks (although the interferogram in Fig. 1 of Ref. 60 does show the presence of a relatively weak system of waves propagating in Regime III).

It is therefore significant that the only difference between the conditions of the present experiment and those of the aforementioned workers are the shock tube cross sectional dimensions. Alpher and White and Bershadet al. used tubes of 8.25-cm x 8.25-cm and 5-cm x 5-cm cross section respectively whereas the dimensions of the present facility are approximately 18-cm x 10-cm. This suggests the possibility of a resonance effect in which the tube cross sectional dimensions and the ionization relaxation zone length are such as to form a cavity capable of supporting a system of transverse waves.

Figure 8 shows a similar pair of interferograms for a shock propagating into nitrogen under similar Mach number and initial pressure conditions. The exponential type dissociation relaxation zone is clearly visible for which the equilibrium degree of dissociation is about 24%. It is interesting to see

that the flow is completely stable and devoid of disturbances with the shock front exhibiting a high degree of planarity (as can be seen by comparison with the adjacent reference wire). This suggests that the transverse wave phenomenon already described is specific to ionized shocks for which the ratio of the shock tube width or height to the relaxation zone length exceeds some critical value. As these waves are not observed behind dissociating nitrogen shocks, it seems reasonable to assume that the argon plasma is providing a means for wave amplification.

Normally, in the absence of applied electric or magnetic fields, plasma instabilities on a macroscopic scale occur due to the existence of a temperature difference between the free electron and heavy particle gases where the latter is composed of ions and neutral atoms. The amplification of initially acoustic disturbances in a collision dominated plasma has been treated by Morse and Ingard (Refs. 61, 62).

However, these authors chose to examine the more usual case in which the electron temperature T_e is initially much larger than the heavy particle temperature T_a . Such conditions are typical of electrically generated plasmas in which the free electrons are initially excited to a high temperature by the application of an electric field which is then terminated allowing the two temperature plasma to relax to equilibrium, the kinetic energy of the free electrons then being transmitted to the heavy particle gas through either a random or a coherent collision process.

The model of Morse and Ingard proposes that in the presence of a low frequency acoustic source where initially $T_e/T_a \gg 1$, the electron energy can become coupled to the acoustic wave such that a positive feedback occurs allowing the electronic energy to be transformed into acoustic energy. The acoustic waves then undergoes spontaneous amplification as a result of this coherent energy transfer where the plasma components all move in phase. In addition, the variation in the state properties of the plasma components are all perturbed to the same degree. In the absence of an initial acoustic perturbation of the plasma the thermal energy of the free electrons would be transferred to the heavy particle gas by random elastic collisions.

It is now relevant to discuss this wave amplification process as it might apply to a thermally generated plasma of the type encountered in the present experiments. The temperatures for the free electron and the heavy particle gases existing in Regimes I and II behind the incident shock front, are the converse of those discussed by Ingard and Morse such that initially $T_e/T_a \ll 1$.

Figure 9 shows a typical two temperature relaxation profile for a $M = 18$ shock into argon at $p_1 = 3$ mmHg as calculated by Oettinger and Bershad (Ref. 60).

Without any theoretical justification it is proposed that, in the case of the thermally generated plasma, the reverse process is possible where the coherent transfer of energy is now directed from the heavy particle gas to the free electrons. There is however some experimental evidence to support this thesis in that the waves exist through the two temperature nature of the plasma existing in Regimes I and II.

Calculations by Measures and Belozerov for strong shocks into hydrogen (Ref. 48) have shown that the electron temperature T_e is essentially equal to the heavy particle temperature T_a in the post shock relaxation zone. As shown in Fig. 10, the temperature difference is virtually zero which contrasts sharply with the large difference between the two temperatures for the case of

argon as seen in Fig. 9.

This difference in behaviour between the hydrogen and argon plasmas arises due to the much larger elastic energy transfer rate between the free electrons and hydrogen in comparison to the corresponding value for argon. This is due to two effects. Firstly (monatomic) hydrogen has 1/40 of the mass of argon and is therefore in better mechanical contact with the electron gas. Secondly, unlike that for argon, the hydrogen-electron elastic collision cross section does not exhibit the Ramsauer effect (Ref. 63). This phenomenon constitutes an anomalous minimum in the electron-atom elastic collision cross sections for the heavier noble gases, which in the case of argon occurs at about 0.4 eV. However this minimum is relatively broad so that for a thermal distribution of velocities at 13500°K, the transfer of kinetic energy to the electron gas from the neutral atom gas through the process of elastic collisions is relatively inefficient. It is therefore clear that the influence of the Ramsauer effect on the relaxation process will be felt primarily in Regime II where the temperatures for both the free electrons and the neutral atoms are approaching the equilibrium value (see Fig. 6(ii)).

It was therefore proposed to add a small percentage of hydrogen to the argon test gas with the purpose of reducing the temperature difference existing between the electrons and the neutral atoms and ions sufficiently to create conditions unfavourable for wave amplification. The hydrogen additive, which for the present shock conditions becomes completely dissociated on passing through the translational shock, has the effect of increasing the rate of energy transfer from the argon atoms to the free electrons through a random elastic collision process thereby raising the free electron temperature to a value closer to that for the neutral atom gas. Simultaneously this should tend to eliminate conditions suitable for the acoustic wave energy transfer mechanism which appears to be highly competitive in the case of pure argon.

A series of experiments was therefore conducted in which varying percentages of hydrogen were added to the argon test gas for constant initial conditions of $M_\infty = 17.10$ and $p_\infty = 2.85$ mmHg. Typical argon shock interferograms are shown in Fig. 11 and Fig. 12 corresponding to concentrations by pressure of 0.033, 0.2 and 0.4% of molecular hydrogen in the pre-shock test gas. The improved planarity of the shock front and stability of the relaxation zone with increasing hydrogen concentration is clearly visible.

Several interesting effects were observed. Firstly increasing the percentage of hydrogen in the test gas had the desired effect of damping out the previously observed wave disturbances until complete stability of the shock relaxation zone was achieved for a hydrogen concentration of 0.4% by pressure.

Secondly as anticipated the relaxation length for Regime I becomes considerably reduced as the atom-atom ionization cross section for hydrogen is much larger than that for argon. Specifically the initial slope of the hydrogen-hydrogen excitation collision cross section curve for the rate controlling ground state to first excited state transition (Ref. 48) is about two orders of magnitude larger than the corresponding value for argon (Ref. 64). As already postulated, the presence of small percentages of hydrogen in the argon test gas will raise the electron temperature both in Regimes I and II. It can therefore be expected that the lengths of Regime II will also be reduced as the ionization rate for electron-atom collisions is strongly dependent on the electron temperature,

varying approximately as $T_e^{3/2}$ (Ref. 58).

Figure 13 shows a plot of the normalized total relaxation zone length $p_1 X$ for argon shocks as a function of the concentration of molecular hydrogen in the initial test gas for $M_s = 17$ and $p_1 = 2.85 \text{ mmHg}$ where X is the experimentally measured overall relaxation zone length. The (visually fitted) curve through the data points appears to asymptote satisfactorily towards the value for pure argon (10 ppm impurity level) obtained by Wong and Bershad (Ref. 58). The addition of relatively large concentrations of oxygen or helium had little effect either on the wave disturbances or the relaxation zone length (see Fig. 13).

A further series of shock runs indicated that the addition of 0.4% of molecular hydrogen to the argon test gas resulted in the complete damping of the previously observed disturbances for $M_s = 17$ to 24 and for corresponding $p_1 = 3.0$ to 0.3 mmHg. Consequently all shock runs made for the purpose of measuring the refractivity of singly ionized argon, were made using a test gas containing 0.4% of molecular hydrogen by partial pressure.

The employment of this expedient immediately raises the question concerning the effect of the hydrogen additive on the experimental fringe shift data, on both the experimental and calculated shock properties used in the data reduction and consequently on the final refractivity results for singly ionized argon. A calculation was therefore performed to estimate the effect of 0.4% of hydrogen on the frozen argon shock properties as exist immediately behind the translational shock front prior to the onset of ionization. It was assumed that the molecular hydrogen becomes completely dissociated on passing through the incident shock. For shock Mach numbers from 17 to 24 and for the corresponding frozen shock temperatures ranging from 25,000 to 50,000 K, the assumption of rapid and complete dissociation of the small hydrogen concentration would seem plausible. The results of this calculation are presented in Fig. 14 as percentage deviations from the pure argon case. Changes in the post shock pressure are negligible whereas the values for the density and temperature are approximately +0.4% and -0.7% respectively for $M_s = 17$. These deviations become smaller with increasing Mach number primarily because the dissociation energy for hydrogen becomes a progressively smaller fraction of the total energy. A similar calculation for Saha equilibrium was not performed as it was considered that the results would reflect the figures already obtained for the frozen shock state, particularly as the ionization potential for hydrogen (13.6 eV) is of a similar magnitude to that for argon (15.8 eV).

Consequently as the effects of the 0.4% of hydrogen on the frozen shock properties for argon are small, it is suggested that the errors incurred by ignoring the presence of the hydrogen on the shock properties and the equilibrium fringe shift measurements would be considerably smaller than those from other sources of error. The analysis of the refractivity data was therefore performed on the assumption that the fringe shift measurements were made for pure argon using equilibrium shock Hugoniot data calculated for the case of pure argon.

So far no comment has been made concerning either the source of the initial perturbation for the flow disturbances or the wave structure of the unsteady ionized shock flow. There exist several types of initial perturbation sources capable of generating acoustic waves. These can conveniently be subdivided into three categories as each type tends to act on the flow in a different way.

The first group consists of stationary sources located near the test section such as small wall imperfections, window bevels, pressure transducer plugs, etc., which are capable of producing Mach waves in the supersonic post shock flow. Although much effort was expended in reducing the number and magnitude of these wall imperfections, this had no apparent effect in improving the stability of the shock flow. In addition it is difficult to visualize how the observed disturbances as typified by the interferograms in Figs. 7 and 11 might develop in the region of the test section during the period of shock passage, particularly in view of the stable nature of the shock flow in the case of the dissociating nitrogen shock shown in Fig. 8. The second group of perturbations can be considered as acoustic or weak shock disturbances produced either at or upstream of the contact surface. The contact surface is generally a diffuse turbulent region which might constitute a weak acoustic source. In addition there exists the possibility of a Rayleigh-Taylor contact surface instability (Ref. 65) which may be specific to combustion driving into the heavier argon test gas but not into the lighter nitrogen test gas. Combustion instabilities in the driver gas particularly in the case of constant pressure combustion where combustion continues after diaphragm rupture, has been observed to generate unsteady flow in the driven shocked gas (Ref. 66). The third and final group of flow perturbations are those classified as remote stationary sources located at distances greater than 60 (equivalent) tube diameters upstream of the test section. Such features are the two 2-in. dia. vacuum pumping ports, the round to rectangular transition section and the ruptured diaphragm. Disturbance from sources of this type generally propagate downstream via a series of multiple transverse Mach wave reflections (Ref. 67) which in the absence of any mechanism for amplification, decay as $x^{-3/2}$, where x is the distance from the source to the point of observation (Ref. 68).

In the case of the ionized shock flow, it is possible for these perturbation sources to act in two ways. Firstly, the flow can "pick-up" the disturbances as it passes the perturbation source which is then sustained at a given level by wave amplification as the shock flow progresses down the tube. Alternatively, the disturbance can be transmitted through the flow in a manner similar to the transverse Mach waves referred to above.

All three types of perturbation source, with one possible exception should in principle generate a system of disturbances in the form of either transverse or normal waves which should be detectable in any equilibrium shock flow. It is therefore significant that wave structure was not observed in the nitrogen shock flow interferograms shown in Fig. 8. However it must be recognized that a schlieren picture of the nitrogen flow might reveal the existence of wave structure not visible on an interferogram*. The exception referred to is the case in which the initial disturbance is generated at a point remote from the test section. This system is then amplified by the ionized shock flow as it is swept downstream to the test section such that a stable system of transverse waves is maintained where all knowledge of original source is lost. This latter mechanism for wave initiation would seem to be the most plausible in view of the existing experimental evidence. But clearly a carefully controlled experimental investigation of this phenomenon is required in order to locate the origin of this unsteady shock flow. The interferograms presented in this work do however contain information regarding the mode of propagation of the disturbances in the shock front and various ionization regions.

* Figure 8(a) shows a similar interferogram for a $M_\infty = 11.6$ shock into oxygen at $p_1 = 40.0$ mmHg for which the equilibrium degree of dissociation is about 18%. Due to the relatively high initial pressure, the disturbances referred to are now visible as a system of transverse waves.

If it assumed that the initial disturbance is either an acoustic or a weak compression wave propagating towards the shock front, then according to the arguments presented, amplification should not occur until the disturbance enters Regime II (see Fig. 6(iii)). Although Regime III is one in which plasma cooling occurs due to radiative losses leading to recombination, there appears to be no reason to expect the electron temperature to differ from that for the heavy particles, suggesting therefore that wave amplification does not occur in this flow regime.

It would now seem reasonable to suggest that wave amplification varies at some function of the product of the temperature difference ($T_a - T_e$) and the electron density N_e so that wave amplification will attain a maximum at some point in Regime II where N_e is rising concurrently with the fall in ($T_a - T_e$) as equilibrium is approached. Inspection of the interferograms in Fig. 7 and 11(i) tends to support this thesis in so much as the disturbances appear to achieve their maximum amplitude in this region particularly at the points of wave confluence located behind the shock front wave heads. The fact that incident shock front has become locally intensified by wave interaction indicates that the disturbances have become weak shock waves (Ref. 69), presumably due to wave amplification.

Under these conditions, the interaction also produces a rearward moving rarefaction wave (Ref. 69), which then interacts with and intensifies both the weak incoming shocks and the ionization density jump whilst the rarefaction wave itself becomes attenuated (Ref. 69). It is possible that these quasi-normal waves visible in Regime III of the interferograms in Fig. 7 and 11, are in fact the rearward moving rarefaction waves referred to above. Why these waves should decay so rapidly as they progress upstream into Regime III is not clear unless wave damping is accomplished through a coupling with the radiative cooling process. However, it must be pointed out that it is not proven that these waves are in fact rearward moving; multiple frame interferometry of the shock flow would resolve this question. (N.B. A similar group of waves is visible in Regime III of the ionized argon shock interferogram shown in Fig. 1 of Ref. 60).

There is however one aspect of the observed flow disturbances, so far not discussed, which lends some credence to the foregoing qualitative analysis. It was noticed that there was a systematic tendency for the number of shock induced heads on the incident shock front to increase whilst simultaneously becoming smaller in amplitude with reduction in the ionization relaxation zone length due to the effect of the hydrogen additive on the ionization process. The shocks shown in Fig. 7, 11(i) and 11(ii) all for similar boundary conditions except for the hydrogen concentrations of 0, 0.033 and 0.4% respectively, have 1, 3 and 4 heads respectively. It therefore appears that the region bounded by the shock front and the ionization-induced density rise is tending to behave as a resonant cavity in which the initial wave perturbation becomes intensified both by the acoustic wave amplification process and by coalescence with additional waves entering this zone. This suggests that the ratio of the shock tube width to the ionization relaxation zone length in conjunction with the Mach wave angle is a governing factor in this process, particularly as these waves were not observed in the argon shock flow interferograms of Bershadet al. (Refs. 58, 59, 60) and of Alpher and White (Ref. 2).

It is interesting that this behaviour, particularly as exemplified by the shock flow in Fig. 11(i) is similar to that observed by White (Ref. 70) for detonations in stoichiometric hydrogen-oxygen mixtures diluted in xenon. A resonant transverse wave structure was also obtained for which the number of wave

heads was considered to be related to the reaction zone thickness.

It is realized that the foregoing qualitative discussion pertaining to the origin and behaviour of these flow disturbances poses as many questions as it answers and must therefore only be considered as tentative. Clearly then an experimental and a theoretical investigation of this phenomenon must be conducted with particular emphasis being put on the following points:

- a) Conduct an experimental investigation to locate the initial perturbation source.
- b) Perform a theoretical study of the acoustic wave amplification process for collision dominated plasmas where $(Ta/Te) \gg 1$ and $N \approx 10^{17} \text{ cm}^{-3}$.
- c) Conduct an experimental and theoretical examination of the action of the hydrogen additive.
 - (i) on the nonequilibrium temperature difference,
 - (ii) on the kinetics of regimes I, II and III and
 - (iii) on the acoustic wave amplification process.

and

- d) Analyze both theoretically and experimentally the various wave interaction processes which have been observed to exist in the present ionized argon shock flows.

4.2.2 Interferometric Measurements

A total of 23 shock runs were performed in argon containing 0.4% of molecular hydrogen by partial pressure with flow and no-flow interferograms obtained at the wavelengths of the ruby laser (6943\AA) and its second harmonic (3471\AA). The shock boundary conditions ranged from $M_s = 1.7$ to 24 and $p_s = 3$ to 0.3 mmHg with corresponding degrees of ionization from 17% to 48%, electron densities of about 10^{17} cm^{-3} and pressures of about 1 atmosphere. The equilibrium plasma temperature remained virtually constant at about 13500°K for all the shock runs due to the compensatory effect of the rise in the degree of ionization with increasing shock Mach number.

The fringe shifts S_{12}^λ between preshock state 1 and Saha equilibrium state 2 were obtained according to the procedure outlined in Appendix A using Eq. A.4. The location of the point corresponding to Saha equilibrium along any given fringe was taken to be that at which the plasma refractive index for state 2 attains a minimum. With reference to the interferograms in Figs. 12 and 15, Saha equilibrium was taken to exist when the negative fringe S_{12}^λ reaches its maximum numerical value prior to the onset of radiation cooling. Values of S_{12}^λ were obtained for four vertically distributed locations across the shock wave interferograms for a given wavelength and shock run. Hence as the value of S_{12}^λ given by Eq. A.4 is itself the average of two measurements, then the final value is the arithmetic mean of eight individual measurements.

As discussed in Section 3.3, it was considered possible to locate the fringe centre lines to an accuracy of $\pm 0.2 \text{ mm}$ which corresponds to a maximum

uncertainty in the fringe shift measurements of ± 0.04 fringes for $\lambda = 3471\text{\AA}$ for which the fringe spacing is a minimum.

An additional seven runs were performed using the neodymium glass laser ($10,600\text{\AA}$) and its second harmonic generator ($5,300\text{\AA}$) thereby utilizing the strong wavelength dependence of the free electron refractivity (see Eq. 2.1.5) in order to obtain accurate experimental measurements of the electron density.

Typical shock flow interferograms for the ruby and neodymium lasers for this final series are shown in Figs. 12 and 15 respectively. The large equilibrium fringe shift ($S_{12}^\lambda \approx 7$) for the neodymium laser wavelength ($10,600\text{\AA}$) and the marked effect due to the radiation cooling in Regime III demonstrates the large negative contribution of the free electrons to the plasma refractive index. The corresponding (positive) fringe shift across the frozen shock ($S_{12}^\lambda \approx 0.2$) is due solely to the compression of the neutral atoms.

The analysis and discussion of the electron density and ion refractivity measurements are given in Sections 4.3 and 4.4 respectively.

4.3 The Experimental Determination of the Equilibrium Electron Density

Accurate values for the neutral atoms, first ion and free electron densities are clearly necessary if the refractivity for (singly) ionized argon is to be measured by the interferometric method described in Section 2.2. The experimentally determined free electron density is obtained by the two-wavelength interferometric method described in Section 2.3 which is independent of the existence of either complete or local thermodynamic equilibrium for the plasma. Hence this measured value can be used as an indicator to show whether the concentrations of the plasma constituents have achieved the values given by the Saha equation for the given boundary conditions. As electron-ion recombination due to radiative cooling is known to commence at some point in Regime II (see Fig. 6) prior to equilibrium (Ref. 60), it is possible for the measured equilibrium electron density to lie below the Saha equilibrium value at all times in which case it would not be possible to determine the ion refractivity from Eq. 2.2.4.

For the laser fundamental wavelength λ_y and its corresponding second harmonic λ_x ($= \lambda_y/2$), N_e^E the experimental electron density is obtained from Eq. 2.3.2 as

$$N_e^E = \frac{\frac{N_o}{\lambda} \lambda_y}{(\mu_e^{y-1})_o^L} \frac{\left[S_{12}^y - \frac{S_{12}^\lambda}{2} \frac{(\mu_A^{y-1})_o}{(\mu_A^\lambda - 1)_o} \right]}{\left[\frac{1}{4} \frac{(\mu_A^{y-1})_o}{(\mu_A^\lambda - 1)_o} - 1 \right]} \quad (4.3.1)$$

where it is assumed that the ratio of the ion refractivity to the atom refractivity is independent of wavelength. The experimental fringe shift terms, S_{12}^y and S_{12}^λ for the second harmonic and fundamental respectively were obtained as described in Section 4.2.2 and Appendix A. L is the test section geometrical path length and is equal to 4.010 inches.

The experimental electron densities were compared to two theoretical values, both of which were calculated for Saha equilibrium assuming radiation losses to be negligible and using the shock Hugoniot equations for the given (experimental) values of M_s , p_1 and T_1 . The first calculated value, N_e^G , was obtained using electronic excitation partition functions which included only the ground state terms. The second and more realistic calculated value, N_e^F , was obtained using partition functions which included terms for the excited electronic states in addition to that for the ground state. The effects of the plasma microfield on the neutral atom partition function and the ionization potential were estimated according to the method of Margenau and Lewis (Refs. 71, 72) in which all those electronic orbits were suppressed whose classical major semi-axes exceeded the Debye shielding distance. Data for the energy levels of neutral and singly ionized argon up to a principal quantum number of 32 were taken from the tabulations of Moore (Ref. 25) together with predicted values taken from Ref. 73.

Before comparing N_e^E to these calculated values, it is pertinent to discuss how and why these two calculations differ from each other. N_e^F and N_e^G are compared on a percentage basis in Fig. 16 in which $(N_e^G - N_e^F)/N_e^F$ is plotted as a function of M_s for $p_1 = 10, 1$ and 0.1 mmHg . Several points of interest apparent from this graph are discussed below.

- (i) N_e^G is always greater than N_e^F because in the calculation of N_e^G , the omission of the excited electronic state terms from the partition functions for the atom and ion results in an increase in energy available for investment in ionization. In addition the ratio of the ion partition function to that for the atom as used in the Saha equation increases due to the relatively large excitation energies for the excited states of singly ionized argon, resulting in an increase in N_e^G in relation to N_e^F .
- (ii) $(N_e^G - N_e^F)$ increases with p_1 for a given M_s because as the degree of ionization decreases with increasing p_1 , more energy becomes available for populating the excited electronic states in the case of N_e^F as this is a non-pressure sensitive process (if to a first approximation one ignores the plasma microfield effect). Since this effect does not exist in the case of N_e^G , then $(N_e^G - N_e^F)$ increases with p_1 for a given value of M_s .
- (iii) $(N_e^G - N_e^F)$ increases with M_s for a given p_1 . This can be understood from (i) above, in which the excited state population in the case of N_e^F increases with increasing M_s .
- (iv) It is observed from Fig. 16 that all of the curves of $(N_e^G - N_e^F)/N_e^F$ plotted for constant p_1 attain a maximum at a given value of M_s . This presumably occurs because as the neutral atom concentration falls with increasing M_s for constant p_1 , then the total energy invested in populating the excited states of neutral argon (in the case of N_e^F) also falls thereby reducing $(N_e^G - N_e^F)$. Due to the large excitation energies for singly ionized argon in relation to those for neutral argon, the excited states for this species do not become commensurately populated as the degree of ionization increases.

Values of $(N_e^G - N_e^F)/N_e^F$ for the thirty experimental shock runs are shown in Fig. 17 as a function of M_s . The average value of $(N_e^G - N_e^F)/N_e^F$ is approximately $\pm 3.5\%$ with the curve exhibiting a slow decrease with increase in M_s due to a corresponding drop in p_1 (for the reasons given in (ii) above).

The principal purpose of Fig. 17 is to compare the experimentally measured electron density N_e^E to the calculated value N_e^F . On average $N_e^E = 1.02 \cdot N_e^F \pm 3\%$ or more specifically $(N_e^F - N_e^E)/N_e^F = \pm 1.9\%$ where the latter difference expression exhibits a slow fall with increasing M_s for the reasons given in (ii) above.

Discussion of this discrepancy between N_e^E and N_e^F is treated in two parts with consideration being given first to possible sources of systematic error in N_e^F and then secondly to those in N_e^E .

Sources of Error in Calculating N_e^F

- a) An obvious source of error in N_e^F exists in model used to terminate the electronic excitation partition function. For an argon plasma at 13,500°K and 1 atmosphere pressure, the model of Margenau and Lewis (Refs. 71, 72) terminates the neutral atom partition function at a principal quantum number $q = 21$. Alternatively if one reduces the ionization potential according to the Debye-Hückel method (Ref. 74) and then terminates the partition function at this new ionization limit, a principal quantum number $q = 9$ is obtained. Clearly this will produce a reduction in N_e^F by increasing the energy available for ionization thereby bringing N_e^F into closer agreement with N_e^E .
- b) As N_e^F is related to a particular experiment through the measured values of M_s , p_1 and T_1 , then errors in these values generate errors in N_e^F in relation to N_e^E which is a product of the fringe shift measurements. As indicated in Section 3.1, the maximum errors in measuring M_s and p_1 are $\pm 1\%$ and $\pm 2-1/2\%$ respectively which produce errors in N_e^F of about $2-1/2\%$ for conditions typical of these experiments. However these error limits on N_e^F are due to random errors and cannot therefore be considered to be the source of the systematic 1.9% difference between N_e^E and N_e^F although they are likely the major source of the $\pm 3\%$ scatter in the $(N_e^E - N_e^F)/N_e^F$ data in Fig. 17.

Sources of Error Incurred in the Measurement of N_e^E

- a) N_e^E was obtained from the experimental fringe shift data on the assumption that the ratio $(\mu_I^\lambda - 1)/(\mu_A^\lambda - 1)$ is independent of wavelength. As the values of N_e^E obtained using both the ruby and neodymium glass lasers are consistent, it is doubtful whether this assumption contributes to this discrepancy. Additional confirmation of this conclusion (as will be shown in the following section) is provided by the fact that the ratio $(\mu_I^\lambda - 1)/(\mu_A^\lambda - 1)$ is effectively constant in the optical and near infrared regions of the spectrum.

- b) It was shown in Section 2.1, that the excited states make a -6.6% contribution to the total neutral argon refractivity at 6943\AA for conditions of $13,500\text{ K}$ and 1 atmosphere pressure. If this excited state contribution is introduced into the data analysis for the ruby laser experiments, it produces an approximately 1% reduction in N_e^E thereby halving the observed discrepancy between N_e^E and N_e^F . However the same excited state refractivity calculation for neutral argon indicated a negligible contribution at $10,600\text{\AA}$. Consequently as the average values of $(N_e^E - N_e^F)/N_e^F$ for wavelengths of 6943\AA and $10,600\text{\AA}$ are + 1.8% and + 2.22% respectively where this small difference is in the direction in-consistent with the calculated excited state refractivity contributions, it is concluded that the excited states are not the principal cause of the observed discrepancy between N_e^E and N_e^F .
- c) The prime purpose for monitoring N_e^E was to observe whether there was any significant lowering of the electron density from the value predicted for Saha equilibrium due to radiative recombination. The intensity of the emitted radiation is known to follow the growth of the free electron concentration in Regime II, attaining a maximum at the point corresponding to Saha equilibrium (Ref. 60). From thereon the loss of energy through radiative cooling induces a fall in the electron density; this is characterized by the relatively slow rise of the fringes in Regime III of the interferograms in Fig. 12 and 15.

It was therefore interesting to find that the experimental values, N_e^E were consistently larger than N_e^F although always lower than the upper bound represented by N_e^G . N_e^E for the thirty shock runs of this experiment are shown in Fig. 18 as a function of M_S together with N_e^F for $p_1 = 10, 1$ and 0.1 mmHg . In all cases N_e^E lies below the value of $7 \times 10^{17} \text{ cm}^{-3}$ suggested by McWhirter (Ref. 75) to be necessary for the attainment of local thermodynamic equilibrium (LTE) in an argon plasma at an electron temperature of $13,500\text{ K}$. Even if LTE does not exist due to radiative transitions creating a relative overpopulation of the ground state with respect to a Boltzmann distribution, it is clear that the total neutral argon population must be in good agreement with the Saha value due to the close correspondence between N_e^E and N_e^F . Hence any deviations from LTE will increase the population of the ground state in relation to the overall excited state population thereby reducing the influence of the large refractivity terms for these states on the refractivity measurements for singly ionized argon. However inspection of the argon shock flow interferograms in Fig. 12 and 15 shows that the collision induced electron-atom ionization relaxation process of Regime II is very much more rapid than the radiative recombination process in Regime III due in part to the presence of the hydrogen additive. It would therefore seem plausible to suggest that under these conditions, the plasma achieves a Boltzmann distribution of internal states at the point corresponding to Saha equilibrium which is then maintained as the plasma cools on passage through Regime III.

- d) Griem (Ref. 76, see also Refs. 13, 14) has suggested that electrons bound in orbits lying close to the ionization continuum, behave as if free in the presence of electro-magnetic radiation. The effect of this phenomenon would therefore be such as to create an apparent increase in the measured value of N_e^E .

- e) As mentioned in Section 3.3, the fringe shifts at 10,600 \AA and 6943 \AA were measured to an estimated accuracy of ± 0.02 fringes. For these measurements at 10,600 \AA and 6943 \AA , the minimum fringe shifts were of the order of 5 and 2 respectively, which produce maximum errors in N_e^E of $\pm 1/2\%$ and $\pm 1\%$ respectively. This is confirmed by the reduced scatter of the $(N_e^E - N_e^F)/N_e^F$ data obtained using the neodymium glass laser in relation to that for the ruby laser. Although these error contribute to the scatter of the $(N_e^E - N_e^F)/N_e^F$ data as shown in Fig. 17, they are of a random nature and therefore do not contribute to the systematic difference between N_e^E and N_e^F .

It is therefore suggested that the observed difference between N_e^E and N_e^F is due either to the use of an unrealistic partition-function sum termination model to calculate N_e^F or to the effect of bound electrons lying close to the continuum acting as if free. However it is felt that the experimental values N_e^E are a better description of reality in the present experiment, particularly as these values are obtained directly from the measured fringe shifts. These values are therefore used in the following section to calculate the ion refractivity term $(\mu_I^\lambda - 1)_o$ from the experimental fringe shift data.

4.4 The Experimental Determination of the Refractivity for Singly Ionized Argon

As outlined in Section 2.2, the ion refractivity at STP is related to the experimentally measured fringe shifts S_{12}^λ at Saha equilibrium by Eq. 2.2.4 which is

$$(\mu_I^\lambda - 1)_o = S_{12}^\lambda (\lambda/L)(N_o/N_{e,2}) - (\mu_e^\lambda - 1)_o - (\mu_A^\lambda - 1)_o \left\{ (N_o/N_{e,2})(\rho_2/\rho_1)/\rho_o \right\}^{-1} \quad (4.4.1)$$

where x , the degree of single ionization has been eliminated through use of the equality $x_2 = (N_{e,2}/N_o)(\rho_o/\rho_2)$. The neutral atom and free electron refractivities at STP are given by Eq. 2.1.8 and 2.1.5 respectively. N_o and ρ_o are Loschmidt's number and the standard density for (neutral) argon. ρ_o the preshock density is calculated directly from the measured quantities p_1 and T_1 via the equation of state.

There are in principle two sources of information regarding the values of the two remaining unknown quantities, ρ_2 and $N_{e,2}$ (or for any pair of the three quantities ρ_2 , x_2 and $N_{e,2}$ which can be employed to determine $(\mu_I^\lambda - 1)_o$).

Firstly, these quantities can be calculated directly from the shock Hugoniot equations for conditions of Saha equilibrium corresponding to the experimental values of M_s , p_1 and T_1 using electronic excitation partition functions which include an array of excited state terms as described in Section 4.3. The accuracy of this calculation is limited principally by the random errors in the measurements of M_s and p_1 which have been estimated to be $\pm 1\%$ and $\pm 2-1/2\%$ respectively (see Section 3.1). For a $M_s = 20$ shock into argon at $p_1 = 1 \text{ mmHg}$ and $T_1 = 298^\circ\text{K}$, a $\pm 1\%$ error in M_s generates a $\pm 1\%$ error in ρ_2 , a $\pm 2-1/2\%$ error in x_2 and a $\pm 4\%$ error in $N_{e,2}$. Similarly a $\pm 2-1/2\%$ error in p_1 generates a

$\pm 1/8\%$ error in ρ_2 , a $\pm 1/8\%$ error in x_2 and a $\pm 2-1/2\%$ error in $N_{e,2}$. It would therefore seem desirable to avoid use of the calculated values of $N_{e,2}$ and x_2 to determine $(\mu_I^\lambda - 1)_o$ from Eq. 4.4.1 due to the relatively large errors produced by the random errors incurred in measuring p_1 and M_s . In addition the calculated value N_e^F was shown in Section 4.3 to be on average about 2% below the experimental value N_e^E which was suggested to be due to use of an unrealistic model for terminating the partition function summation.

The second source of information regarding the values of ρ_2 , x_2 and $N_{e,2}$ is provided by the method of two wavelength interferometry which has already been employed to determine $N_{e,2}^E$ (see Sections 2.3 and 4.3). By simultaneous solution of Eq. 2.2.3 for λ_y and λ_x , the laser fundamental and second harmonic wavelengths respectively, expressions for the experimental values of ρ_2 , x_2 and $N_{e,2}$ are obtained directly in terms of the refractivities for the component species at STP and the experimentally measured fringe shifts S_{12}^x and S_{12}^y . Unfortunately the expressions for ρ_2 and x_2 are dependent on the 'as yet' unknown values of $(\mu_I^\lambda - 1)_o$ whereas that for $N_{e,2}$ (Eq. 2.3.2) is to a first approximation independent of the ion refractivity as discussed in Section 2.3.

In view of these foregoing comments and those already made in Section 4.3 regarding $N_{e,2}$, it was decided to use the experimental values of $N_{e,2}^E$ in the expression for $(\mu_I^\lambda - 1)_o$ together with the calculated values of ρ_2 as this quantity has been shown to be relatively insensitive to errors in M_s and p_1 .

The mean values for the refractivity and polarizability of singly ionized argon, calculated from the experimental data via Eq. 4.4.1 are given in Table 3 for wavelengths of 3471\AA and 5300\AA . Also shown are the corresponding values of K_I^λ , the specific refractivity or Gladstone-Dale constant. K_s^λ , the specific refractivity for species s at wavelength λ is related to the refractivity $(\mu_s^\lambda - 1)$ through the relationship

$$K_s^\lambda \rho_s = (\mu_s^\lambda - 1) \quad (4.4.2)$$

As the mass densities for neutral and singly ionized argon at STP are equal if one neglects the difference corresponding to the mass of one electron, then through use of the equalities represented by Eq. 1.1.1 and Eq. 4.4.2, we have that

$$\frac{(\mu_I^\lambda - 1)_o}{(\mu_A^\lambda - 1)_o} = \frac{K_I^\lambda}{K_A^\lambda} = \frac{(\alpha_I^\lambda)_o}{(\alpha_A^\lambda)_o} .$$

As this ratio is frequently employed in the interferometry of argon plasmas, the values for $\lambda = 3471\text{\AA}$ and 5300\AA are also given in Table 3. The individual values for the ratio of the ion refractivity to that for the atom, $(\mu_I^\lambda - 1)_o / (\mu_A^\lambda - 1)_o$, are presented in histogram form in Fig. 19 and 20 for $\lambda = 3471\text{\AA}$ and 5300\AA respectively and for cell widths of 0.1, together with the corresponding Gaussian probability distribution curves (Ref. 77). The histogram for the 23 measurements of $(\mu_I^\lambda - 1)_o / (\mu_A^\lambda - 1)_o$ for $\lambda = 3471\text{\AA}$, exhibits a reasonable correspondence with the Gaussian curve in view of the limited number of samples. The histogram for

$\lambda = 5300\text{\AA}$ is however somewhat more erratic reflecting the fact that only seven results were available.

The large spread of the data in both of these histograms is due primarily to the fact that the fringe shift contribution for the ion is generally a small fraction of the total due to all of the contributing species. For $\lambda = 3471\text{\AA}$ and shock conditions of $M_s = 20$, $p_1 = 1 \text{ mmHg}$ and $T_1 = 298^\circ\text{K}$ and taking $(\mu_I^\lambda - 1) / (\mu_A^\lambda - 1) = 0.65$, the ion contributes about 8% to the sum of the moduli of the fringe shifts for all of the contributing species. Clearly for longer wavelengths, this ion fringe shift contribution will become an even smaller fraction of this total. However the averages of the individual experimental errors for $(\mu_I^\lambda - 1) / (\mu_A^\lambda - 1)$ calculated using the estimated measurement errors for M_s , p_1 , T_1 and S_{12} as given in Section 3.3, were found to be about 2.6 and 3.7 times the standard deviation at 3471\AA and 5300\AA respectively, suggesting that the random error limits given in Section 3.1.4 are overly pessimistic.

Experimental values of $(\mu_I^\lambda - 1) / (\mu_A^\lambda - 1)$ were also determined for the laser fundamental wavelengths $\lambda = 6943\text{\AA}$ and $10,600^\circ\text{\AA}$ and were found to be almost exactly equal to values for the corresponding laser second harmonic wavelengths. This degree of correspondence was regarded with some suspicion particularly as the fringe shifts for these relatively long wavelengths are due principally to the contribution from the free electrons. Investigation of this behaviour showed that the apparent agreement was a direct result of using the experimental values of $N_{e,2}$ to obtain the ion refractivity from Eq. 4.4.1. In deriving the expression for $N_{e,2}$ in Section 2.3 in terms of the experimental fringe shifts, it was assumed that the ratio $(\mu_I^\lambda - 1) / (\mu_A^\lambda - 1)$ was independent of wavelength. Although large (possible) deviations from this assumption were shown to have a negligible effect on the experimental values of $N_{e,2}$ obtained via Eq. 2.3.2, it was found that the effect of this assumption was being carried through into the experimental values of $(\mu_I^\lambda - 1) / (\mu_A^\lambda - 1)$ due to the high sensitivity of the measurements to small changes in electron density. A test calculation for shock conditions of $M_s = 20$, $p_1 = 1 \text{ mmHg}$ and $T_1 = 298^\circ\text{K}$ indicated that a real $\pm 5\%$ difference between the values of $(\mu_I^\lambda - 1) / (\mu_A^\lambda - 1)$ for $\lambda = 3471\text{\AA}$ and 6943\AA would result in a $\pm 1\%$ error in this same ratio at 3471\AA but a $\pm 8\%$ error at 6943\AA if this difference was left unaccounted for in the determination of the experimental values of $N_{e,2}$ through Eq. 2.3.2 instead of the more exact formulation given by Eq. 2.3.1. As these percentages indicate, this assumption tends to bring the calculated values of $(\mu_I^\lambda - 1) / (\mu_A^\lambda - 1)$ for the two wavelengths λ_x and λ_y into close agreement while increasing the absolute error of these calculated values with respect to the real value. It is therefore obvious that the assumption that $(\mu_I^\lambda - 1) / (\mu_A^\lambda - 1)$ is a constant in the derivation of $N_{e,2}$ from the experimental data, can have a significant effect on the ion refractivity at the (longer) laser fundamental wavelength such that these two values tend to asymptote to a common value close to the real value for the wavelength of the laser second harmonic. The ion refractivity results for the laser fundamental wavelengths have therefore been rejected due in part to the low experimental sensitivity attainable under these conditions and in part to the tendency of these results to take on values close to those for the (shorter) second harmonic wavelengths.

However the mean experimental values for the ratio of the ion refractivity to that for the neutral atom obtained from the independent interferometric measurements at 3471 \AA and 5300 \AA , are in close agreement (see Table 3) i.e., $(\mu_I^\lambda - 1)_o / (\mu_A^\lambda - 1)_o = 0.65$. This result is not surprising for, as discussed in Section 2.1., the dispersion for singly ionized argon in the visible and near ultra-violet parts of the spectrum should be similar to that for neutral argon as the resonance transitions lie in the vacuum ultra-violet region. This result therefore validates the assumption used to obtain $N_{e,2}^E$ from Eq. 2.3.2 that the ratio $(\mu_I^\lambda - 1)_o / (\mu_A^\lambda - 1)_o$ is essentially independent of wavelength, which in turn justifies the use of the experimental values of $N_{e,2}^E$ to derive the ion refractivity from Eq. 4.4.1.

It is now relevant to discuss the possible effects of the excited electronic states on the argon ion refractivity results. In Section 2.1 it was shown that the excited states for neutral argon make contributions of approximately -1/2% and -1% to the total neutral atom refractivity at 3471 \AA and 5300 \AA respectively for an argon plasma in LTE at 13,500 K and 1 atmosphere pressure (see Fig. 1 and Table 2.). As these contributions were not included in the data analysis for $(\mu_I^\lambda - 1)_o$, they will represent corresponding corrections to $(\mu_I^\lambda - 1)_o$ of the order of +1/2% and +1% respectively. However as these corrections were found to be relatively small fractions of the total error limits given for $(\mu_I^\lambda - 1)_o$, they were not incorporated into the final refractivity values given in Table 3.

In addition, as already discussed in Section 4.3, the consistency of the experimental $N_{e,2}^E$ results obtained using the dual frequency ruby and neodymium glass lasers indicated that the effect of the excited states was not apparent at the laser fundamental wavelengths. The only significant calculated excited state contribution was found to occur at the ruby laser wavelength, $\lambda = 6943\text{\AA}$. For an argon plasma in LTE (Ref. 75) at 13,500 K and 1 atmosphere pressure, the excited states for neutral argon were calculated to produce a 6.6% reduction in the total species refractivity at 6943 \AA . As shown in Section 4.3 this would reduce the experimentally measured electron densities by about 1%. Hence as the same calculation indicated a negligible contribution at the neodymium glass laser wavelength $\lambda = 10,600\text{\AA}$ and as the average values for $N_{e,2}^E$ obtained using the two lasers differ by about 0.3% in a direction inconsistent with the calculated excited state contribution, it would seem that the excited states have not influenced the experimental electron density results used to calculate $(\mu_I^\lambda - 1)_o$ from Eq. 4.4.1, for the prevailing plasma conditions. It is therefore concluded that for an argon plasma in LTE for conditions of 13,500 K and pressures of the order of 1 atmosphere, the excited states for neutral and singly ionized argon make a negligible contribution to the overall plasma refractive index at the laser wavelengths employed in these experiments. The refractive index data for singly ionized argon given in Table 3 therefore in effect represents the ground state term for this species.

Finally it is interesting to compare the experimentally measured ratio $(\mu_I^\lambda - 1)_o / (\mu_A^\lambda - 1)_o = 0.65$ with the only available theoretical value of 0.72 calculated for infinite wavelength using Slater screening constant theory (Ref. 10). However this correspondence does not apply to the individual refractivities for as indicated in Section 1, this theory is at best only approximate particularly as the absolute calculated values for both neutral and singly ionized

argon are about 2-1/2 times larger than the corresponding experimental values.

4.5 Conclusions

Interferometric measurements made in the visible (5300\AA) and near ultraviolet (3471\AA) regions indicate that the refractivity and electric dipole polarizability for singly ionized argon has a value of about 0.65 of the corresponding value for neutral argon.

This experimental determination shows reasonable correspondence with the calculated ratio for the static polarizabilities but as yet there exists no rigorous calculation for the polarizability of singly ionized argon with which to compare this experimental value.

The constancy of the measured electron densities and ion refractivities obtained at different wavelengths suggest that the effects of the excited state refractivities have not been observed for the conditions of the present experiments.

Experimental confirmation for the validity of the excited state refractivity calculation for neutral argon could be obtained by performing shock tube argon plasma interferometry close to the broad resonance peaks calculated to occur at about 8200\AA and 9100\AA .

REFERENCES

1. Alpher, R. A.
White, D. R.

Phys. Fluids 1, 452 (1958)
2. Alpher, R. A.
White, D. R.

Phys. Fluids 2, 162 (1959)
3. Alpher, R. A.
White, D. R.

Phys. Fluids 2, 153 (1959)
4. White, D. R.

Phys. Fluids 4, 40 (1961)
5. Marlow, W. C.
Bershader, D.

A Shock Tube Study of the Electric Polarizability of Atomic Hydrogen. Stanford University, SUDAAR No. 149, April 1963.
6. Marlow, W. C.
Bershader, D.

Phys. Rev. 133, A629 (1964)
7. Anderson, J. H. B.

An Experimental Determination of the Gladstone-Dale Constants for Dissociating Oxygen. UTIAS T.N. 105, March 1967.
8. Anderson, J. H. B.
Osborne, P. J. K.
Glass, I. I.

Phys. Fluids 10, 1848 (1967)
9. Anderson, J. H. B.

Phys. Fluids. Supplement I, 57 (1969).
10. Hirschfelder, J. O.
Curtiss, C. F.
Bird, R. B.

Molecular Theory of Gases and Liquids. J. Wiley & Sons, New York, 1954.
11. Ascoli-Bartoli, U.
DeAngelis, A.
Martellucci, S.

Il Nuovo Cimento 18, 1116 (1960).
12. Alpher, R. A.
White, D. R.

Optical Interferometry. Ch.X in Plasma Diagnostic Techniques. R. H. Huddlestone and S. L. Leonard, Eds. Academic Press, New York, 1965.
13. Hug, W. F.
Evans, D. L.
Tankin, R. S.
Cambel, A. B.

Measured Index of Refraction of an Argon Plasma ARL Rep. No. 66-0140, July, 1966.
14. Hug, W. F.
Evans, D. L.
Tankin, R. S.
Cambel, A. B.

Phys. Rev. 162, 117 (1967).

15. Hug, W. F.
Tankin, R. S.
Cambel, A. B.
Measurements of the Refractive Index in an Argon Plasma
at 6328 \AA and 1.15 μ ARL Rep. No. 67-0218, Dec, 1967.
16. Ten Seldam, C. A.
De Groot, S. R.
Physica 18, 910 (1952)
17. Weinberg, F. J.
Optics of Flames, Butterworths, London, 1963.
18. Ditchburn, R. W.
Light, Interscience, New York, 1953.
19. Ladenburg, R.
Rev. Mod. Phys. 5, 243 (1933).
20. Mitchell, A. C.
Zemansky, M. W.
Resonance Radiation, Cambridge University Press, 1961.
21. Wiese, W. L.
Smith, M. W.
Miles, B. M.
Atomic Transition Probabilities Vol II Sodium Through
Calcium. NSRDS-NBS22, U.S. Government Printing Office,
Washington, 1969.
22. Peck, E. R.
Fisher, D. J.
J. Opt. Soc. Am. 54, 1362 (1964)
23. Mansfield, C. R.
Peck, E. R.
J. Opt. Soc. Am. 59, 199 (1969)
24. Chaschina, G. I.
Gladushchak, V. I.
Shreider, E. Y.
Opt. Spectr. 24, 542 (1968)
25. Moore, C. E.
Atomic Energy Levels, National Bureau of Standards
Circular No. 467, Vol. I. U.S. Government Printing
Office, Washington, 1949.
26. Pollock, E.
Robinson, E. J.
Bederson, B.
Phys. Rev. 134, A 1210 (1964)
27. Robinson, E. J.
Levine, J.
Bederson, B.
Phys. Rev. 146, 95 (1966)
28. Drellishak, K. S.
Knopp, C. F.
Cambel, A. B.
Partition Functions and Thermodynamic Properties of
Argon Plasmas. Arnold Engineering Development Center
Rep. No. AEDC-TDR-63-146. Aug, 1963.
29. Murphy, P. W.
J. Opt. Soc. Am. 58, 1200 (1968)
30. Johnston, P. D.
Proc. Phys. Soc. (G.B.) 92, 896 (1967)
31. Wright, A. E. Jr.,
Evans, D. L.
Tankin, R. S.
Cambel, A. B.
Argon Electron Transition Tables ARL Rep. No. 67-0016.
Jan, 1967.

32. Desai, S. V. J. Quant. Spectr. Rad. Trans. 8, 172 (1968)
Corcoran, W. H.
33. Desai, S. V. Private Communication 1969.
34. Measures, R. M. Applied Optics 9, 737 (1970)
35. Boyer, A. G. Design, Instrumentation and Performance of the UTIAS
4 in. x 7 in. Hypersonic Shock Tube. UTIAS Rep. No. 99,
May, 1965.
36. Benoit, A. Thermodynamic and Composition Data for Constant Volume
Combustion of Stoichiometric Mixtures of Hydrogen-
Oxygen Diluted with Helium and Hydrogen. UTIAS Tech.
Note No. 85, Nov., 1964.
37. Nagamatsu, H. T. J. Appl. Phys. 30, 1018 (1959)
Martin, E. D.
38. Hayward, A. T. J. J. Sci. Instrum. 40, 173 (1963)
39. Dow Corning Corp. Dow Corning 704 Diffusion Pump Fluid. Bulletin 05-189,
Sept, 1967. Midland, Michigan.
40. Mulac, A. J. An Experimental and Theoretical Investigation of Shock
Tube Precursors. Stanford University, SUDAAR No. 358,
Sept, 1968.
41. Cody, W. G. Piezoelectricity, McGraw Hill, New York, 1946.
42. Weymann, H. D. Phys. Fluids 12, 1193 (1969)
43. Weymann, H. D. Phys. Fluids 12, 1200 (1969)
44. Alcock, A. J. Appl. Phys. Letters 8, 187 (1966)
Ramsden, S. A.
45. Martellucci, S. Nuovo Cimento 44B, 107 (1966)
Mazzucato, E.
46. David, C. D. Jr., Appl. Phys. Letters 11, 394 (1967)
47. Oertel, F. H. Two wavelength laser interferometry of hypersonic ionized
Spurk, J. H. flows. Int. Congr. on Instrumentation in Aerospace
Simulation Facilities, pp. 229-234, Brooklyn Poly-
technic Institute, New York, May 1969.
48. Belozerov, A. N. J. Fluid Mech. 36, 695 (1969)
Measures, R. M.
49. Jeffries, R. A. Phys. Fluids 13, 211 (1970)
50. Boyd, G. D. Phys. Rev. 137, A1305 (1965)
Ashkin, A.
Dziedzic, J. M.
Kleinman, D. A.

51. Zernike, F. Jr., J. Opt. Soc. Am. 54, 1215 (1964)
 52. Volosov, V. D. Sov. Phys. Tech. Phys. 13, 576 (1968)
 Diviekeev, M. I.
 Perlov, D. I.
 53. Barrett, J. J. Phys. Rev. 131, 1469 (1963)
 Weber, A.
 54. Frungel, F. B. A. High Speed Pulse Technology, Vol. II Optical Pulses,
 Lasers, Measuring Technique. Academic Press, New
 York, 1965.
 55. Hall, J. G. The Design and Performance of a 9 inch Plate Mach-
 Zehnder Interferometer, U.T.I.A. Rep. No.27, March,
 1954.
 56. Ladenburg, R. W. 'Interferometry' in Physical Measurements in Gas
 Bershader, D. Dynamics and Combustion. Vol. IX. High Speed
 Aerodynamics and Jet Propulsion Series. Princeton
 University Press, 1954.
 57. Pope, T. P. J. Opt. Soc. Am. 57, 951 (1967)
 Kirby, T. B.
 58. Wong, H. J. Fluid. Mech. 26, 459 (1966)
 Bershader, D.
 59. Horn, K. P. J. Plasma Phys. 1, 157 (1967)
 Wong, H.
 Bershader, D.
 60. Oettinger, P. E. AIAA J. 5, 1625 (1967)
 Bershader, D.
 61. Morse, P. M. 'Theoretical Acoustics'. McGraw-Hill, New York, 1968.
 Ingard, K. U.
 62. Ingard, K. U. Phys. Rev. 145, 41 (1966)
 63. Massey, H. S. W. 'Electronic and Ionic Impact Phenomena'. Oxford Uni-
 Burhop, E. H.S. versity Press, 1952.
 64. McLaren, T. I. Phys. Fluids 11, 2162 (1968)
 Hobson, R. M.
 65. Levine, M. A. Phys. Fluids 13, 1166 (1970)
 66. Wittlif, C. E. Shock Tube Driver Techniques and Attenuation Measure-
 Wilson, M. R. ments. Cornell Aero. Lab, Rep. No. AD-1052-A-4,
 Aug, 1957.
 67. Weynants, R. R. An Experimental Investigation of Shock Wave Diffraction
 Over Compression and Expansion Corners. UTIAS
 T. N. 126, April, 1968.

68. Lapworth, K. C. J. Fluid Mech. 6, 469 (1959)
69. Glass, I. I. J. Aero. Sci. 22, 73 (1955)
Patterson, G. N.
70. White, D. R. Phys. Fluids 4, 465 (1961)
71. Margenau, H. Rev. Mod. Phys. 31, 594 (1959)
Lewis, M.
72. Drelichak, K. S. Phys. Fluids 6, 1280 (1963)
Knopp, C. F.
Cambel, A. B.
73. Drelichak, K. S. 'Partition Functions and Thermodynamic Properties of Argon Plasma'. Arnold Engineering Development Centre, Technical Rep. A.E.D.C.-TDR-63-146, August, 1963.
Knopp, C. F.
Cambel, A. B.
74. McChesney, M. Canad. J. Phys. 42, 2473 (1964)
75. McWhirter, R. W. P. 'Departures from Local Thermodynamic Equilibrium'. Presented in 'A Survey of Phenomena in Ionized Gases'. International Atomic Energy Agency, Vienna, 1968.
76. Griem, H. R. Phys. Rev. 128, 997 (1962)
77. Moroney, M. J. 'Facts from Figures' Pelican No. A236, Penguin Books, London, 1965.
78. American Institute of Physics Handbook, McGraw-Hill, New York, 1963.
79. Wiese, W. L. J. Opt. Soc. Am. 59, 1206 (1969)
Bridge, J. M.
Kornblith, R. L.
Kelleher, D. E.
80. Abella, I. D. J. Appl. Phys. 32, 1177 (1961)
Cummins, H. Z.
81. Glass, I. I. Handbook of Supersonic Aerodynamics, Section 18, Shock Tubes. NAVORD Report 1488 (Vol.6). Bureau of Naval Weapons, 1959.
Hall, J. G.
82. D. W. Balderstone, R. J. North Schlieren Methods, Notes on Applied Science No.31, National Physical Laboratory. HMSO, London, 1963.

AUTHOR	SPECIES	REF.
ALPHER & WHITE (1958, 1959)	ϵ^- (Free Electron)	1, 2
ALPHER & WHITE (1959)	O, N	3
WHITE (1961)	OH	4
MARLOW & BERSHADER (1963, 1964)	H	5, 6
ANDERSON, OSBORNE & GLASS (1967, 1969)	O	7, 8, 9
BRISTOW (1970)	Ar ⁺	present text

TABLE I MEASUREMENTS OF INDUCED ELECTRIC DIPOLE
POLARIZABILITY FOR HIGH TEMPERATURE GASEOUS
SPECIES BY MEANS OF SHOCK TUBE INTERFEROMETRY

λ (Å)	3471.75	5300	6328	6943.5	10600	11523
T (°K) (Ψ_A)						
10000 (1.001)	-3.774 $\times 10^{-8}$	-1.077 $\times 10^{-7}$	-2.173 $\times 10^{-7}$	-5.695 $\times 10^{-7}$	+1.031 $\times 10^{-7}$	-3.732 $\times 10^{-6}$
13500 (1.023)	-1.267 $\times 10^{-6}$	-3.501 $\times 10^{-6}$	-6.721 $\times 10^{-6}$	-1.701 $\times 10^{-5}$	-6.980 $\times 10^{-7}$	-6.690 $\times 10^{-6}$
15000 (1.073)	-3.300 $\times 10^{-6}$	-9.021 $\times 10^{-6}$	-1.702 $\times 10^{-5}$	-4.259 $\times 10^{-5}$	-5.068 $\times 10^{-6}$	-2.183 $\times 10^{-5}$
20000 (2.727)	-1.216 $\times 10^{-5}$	-3.236 $\times 10^{-5}$	-5.839 $\times 10^{-5}$	-1.420 $\times 10^{-4}$	-4.537 $\times 10^{-5}$	-1.177 $\times 10^{-4}$
$(\mu_A^\lambda - 1)_0$	2.903 $\times 10^{-4}$	2.828 $\times 10^{-4}$	2.812 $\times 10^{-4}$	2.805 $\times 10^{-4}$	2.788 $\times 10^{-4}$	2.786 $\times 10^{-4}$

Table 2. Calculated excited state refractivities for neutral Argon as a function of temperature T and wavelength λ for a Plasma pressure $p = 1 \text{ atm}$. electronic partition function Ψ_A is shown in parenthesis below corresponding temperature.

Refractivity for neutral (ground state) Argon at STP, $(\mu_A^\lambda - 1)_0$, is shown on last row for comparison.

	WAVELENGTH, λ (Å)	3471.75	5300
REFRACTIVITY at S.T.P., $(\mu_i^\lambda - 1)_0 \times 10^4$		1.89 ± 0.10	1.83 ± 0.12
POLARIZABILITY, $(\alpha_i^\lambda)_0 (a_0^3)$	1	7.54 ± 0.39	7.31 ± 0.47
	$(\alpha_i^\lambda)_0 (cm^3) \times 10^{24}$	1.12 ± 0.06	1.08 ± 0.07
SPECIFIC REFRACTIVITY, $\kappa_i^\lambda (cm^3/gm)$		0.106 ± 0.005	0.103 ± 0.006
$[\alpha_i^\lambda]/[\alpha_A^\lambda]_0, [\mu_i^\lambda - 1]_0, \kappa_i^\lambda/\kappa_A^\lambda$	2	0.650 ± 0.033	0.647 ± 0.041
NUMBER OF SHOCK RUNS		23	7

1 FIRST BOHR RADIUS , $a_0 = 0.5292 \text{ \AA}$

2 $\alpha_A^\lambda, (\mu_A^\lambda - 1)_0$ & κ_A^λ FROM REF. 22

TABLE 3. REFRACTIVITY, POLARIZABILITY & SPECIFIC REFRACTIVITY
RESULTS FOR SINGLY IONISED ARGON

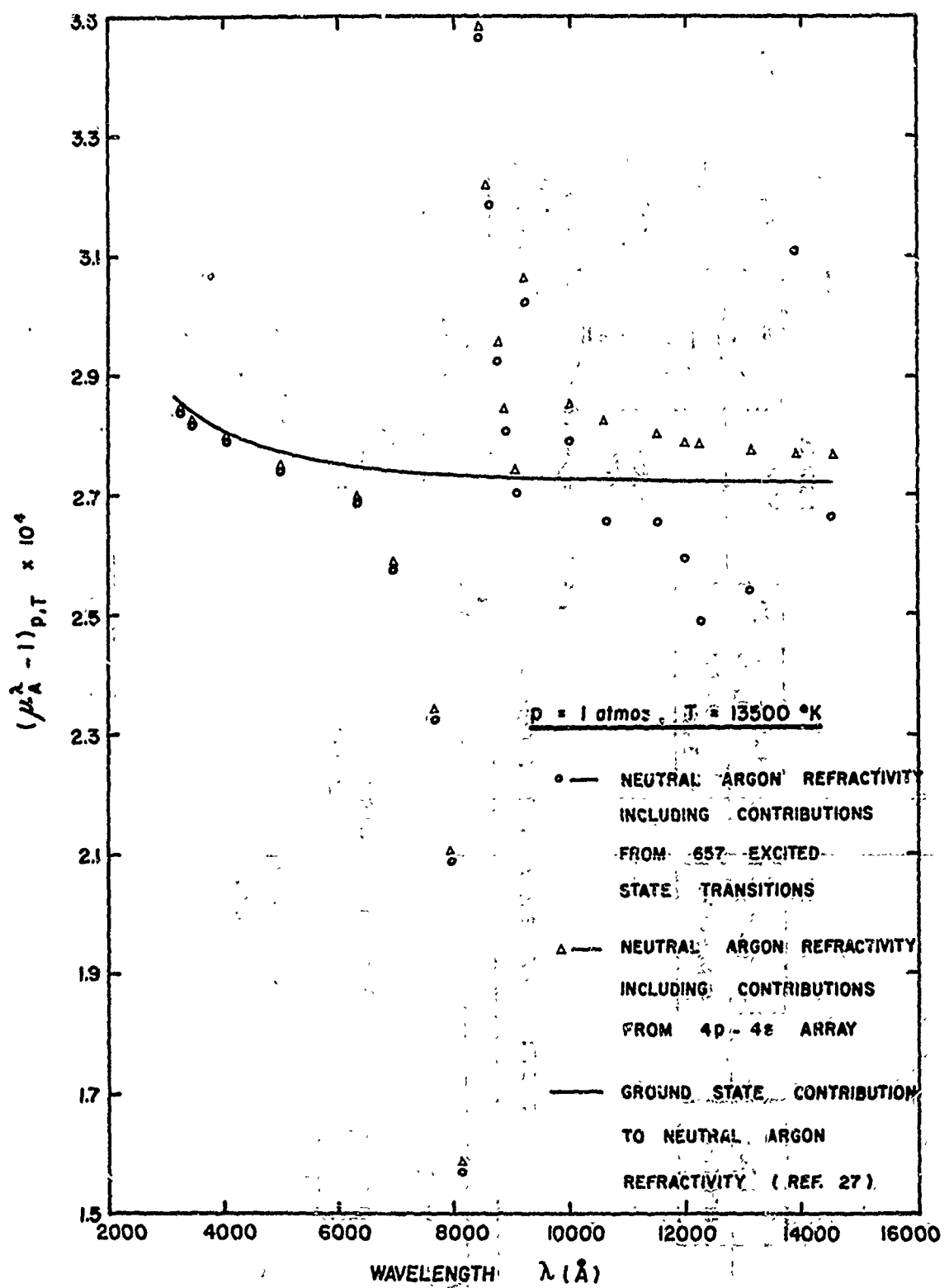


FIG. 1. CALCULATED NEUTRAL ARGON REFRACTIVITY INCLUDING EXCITED STATE CONTRIBUTIONS AS A FUNCTION OF WAVELENGTH FOR PLASMA CONDITIONS OF $13,500^\circ\text{K}$ AND 1 ATMOSPHERE PRESSURE

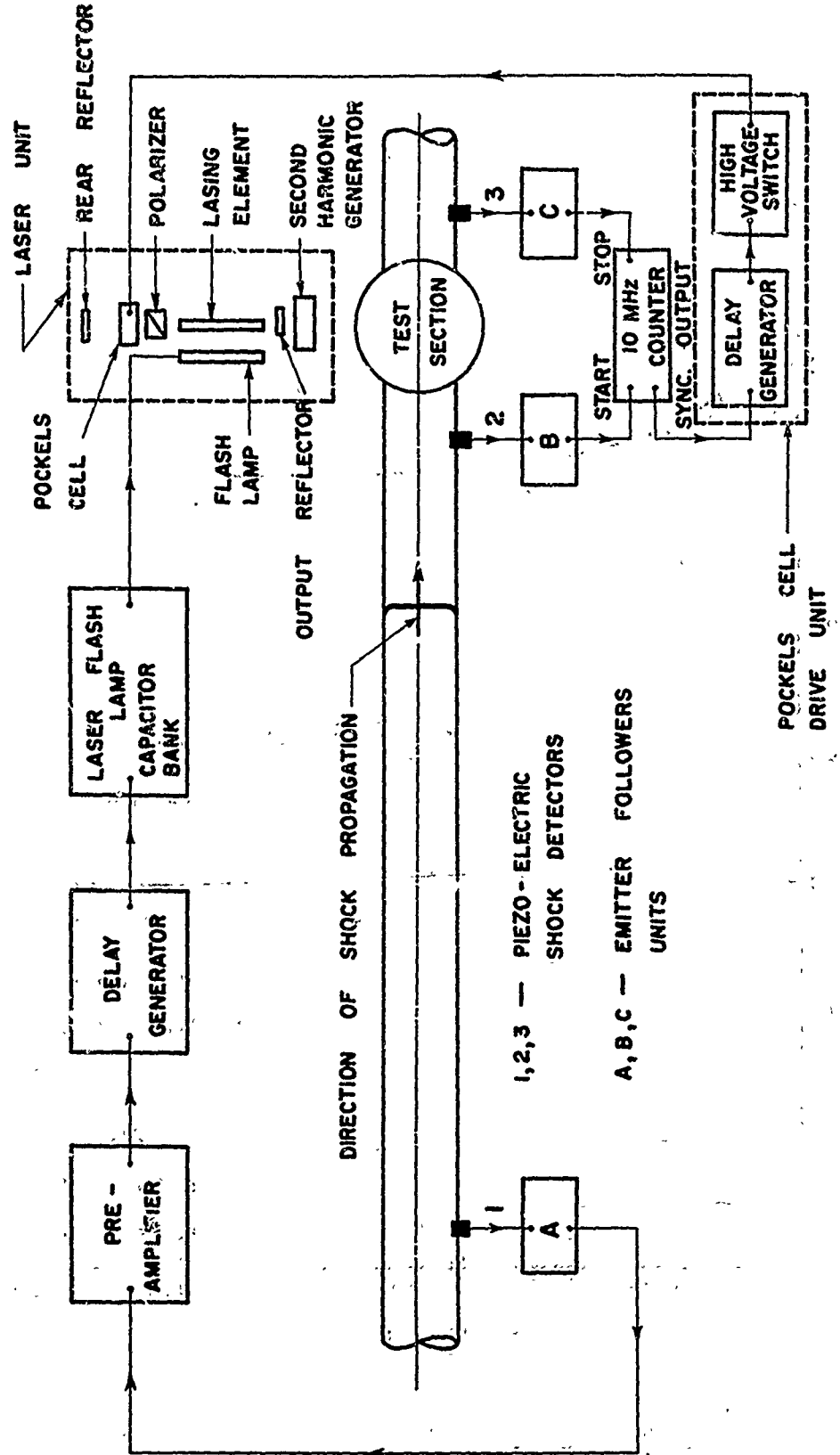
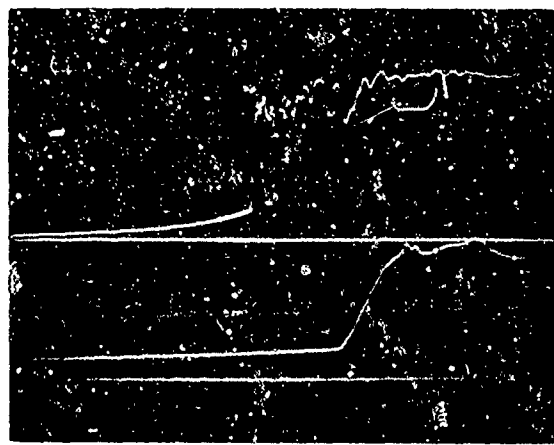
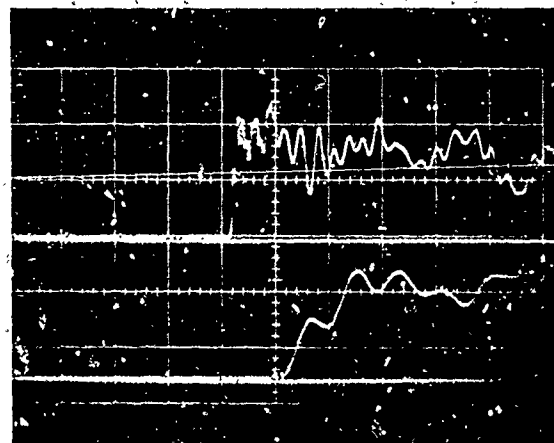


FIG. 2. SCHEMATIC LAYOUT OF ELECTRONICS FOR SHOCK VELOCITY MEASUREMENT AND LASER OPERATION.



(a) RUN #51, $M_s = 20.50$, $p_i = 1.228 \text{ mm Hg}$, $T_i = 297.0^\circ \text{K}$
UPPER TRACE $10 \mu\text{sec/cm}$, $1\nu/\text{cm}$
LOWER TRACE $1\mu\text{sec/cm}$, $1\nu/\text{cm}$
GAUGE COVERED WITH TRANSLUCENT LAYER OF
EPOXY RESIN.



(b) RUN #57, $M_s = 22.40$, $p_i = 0.614 \text{ mm Hg}$, $T_i \approx 295.3^\circ \text{K}$
UPPER TRACE $10 \mu\text{sec/cm}$, $1/2 \nu/\text{cm}$
LOWER TRACE $1\mu\text{sec/cm}$, $1/2 \nu/\text{cm}$
GAUGE COVERED WITH OPAQUE LAYER OF BLACK
SILICONE (RTV) RUBBER.

FIG. 3 EFFECT OF RADIATION PRECURSOR ON PIEZO-ELECTRIC SHOCK DETECTOR

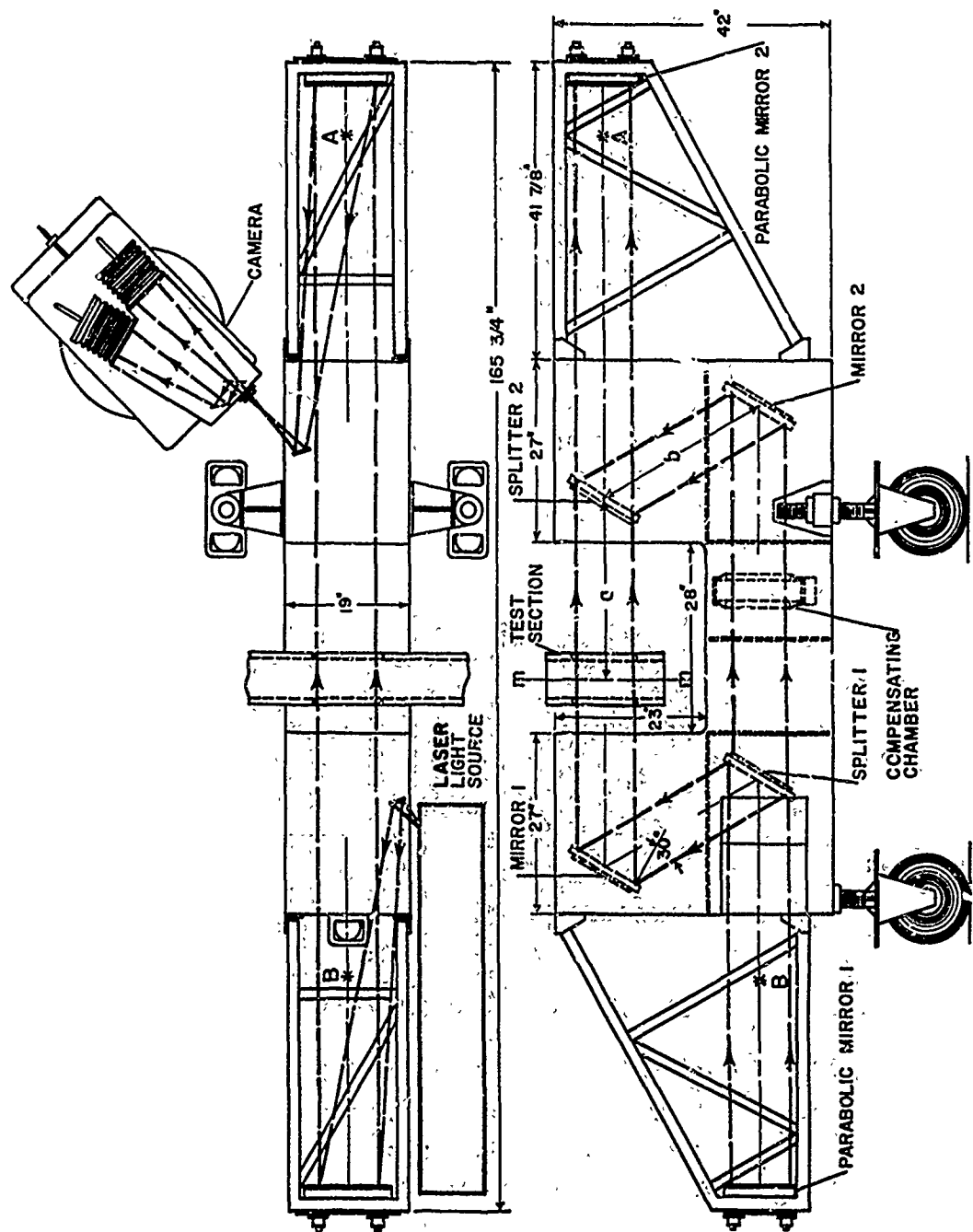


FIGURE 4. GEOMETRY OF 9 INCH MACH-ZEHNDER INTERFEROMETER

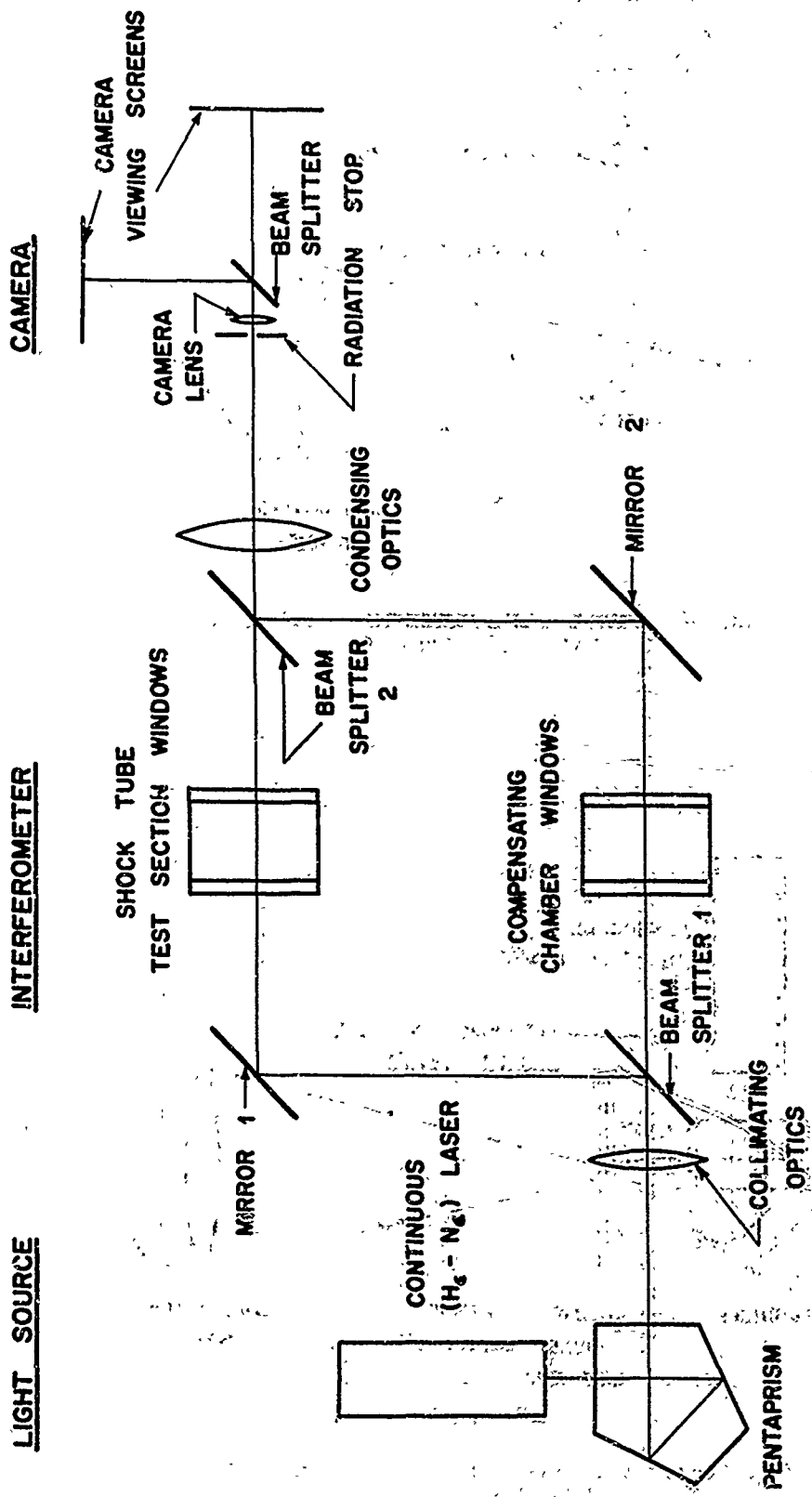


FIG. 5(a). INITIAL ALIGNMENT OF COMPLETE OPTICAL SYSTEM WITH HELIUM-NEON LASER.

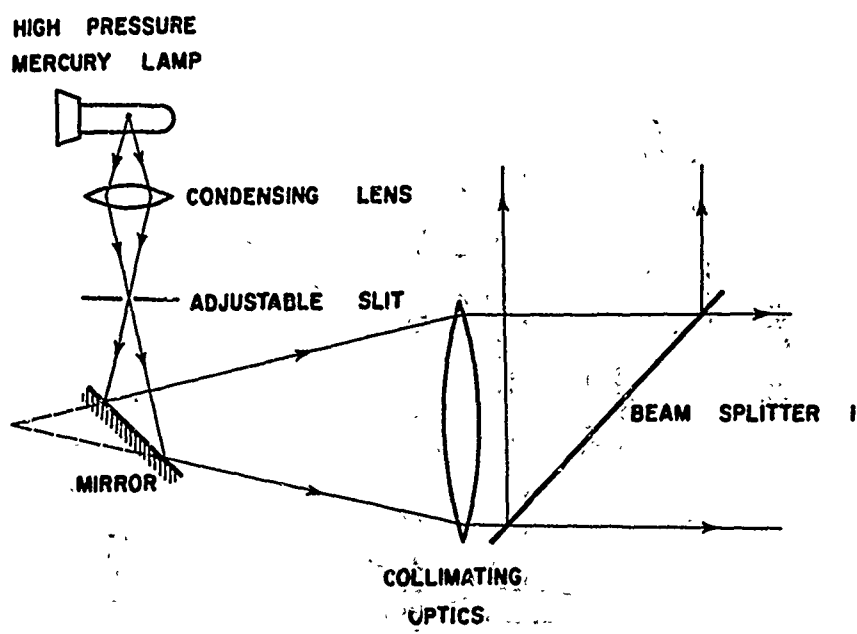


FIG. 5(b): INITIAL FRINGE ADJUSTMENT OF INTERFEROMETER
USING MERCURY VAPOUR LAMP.

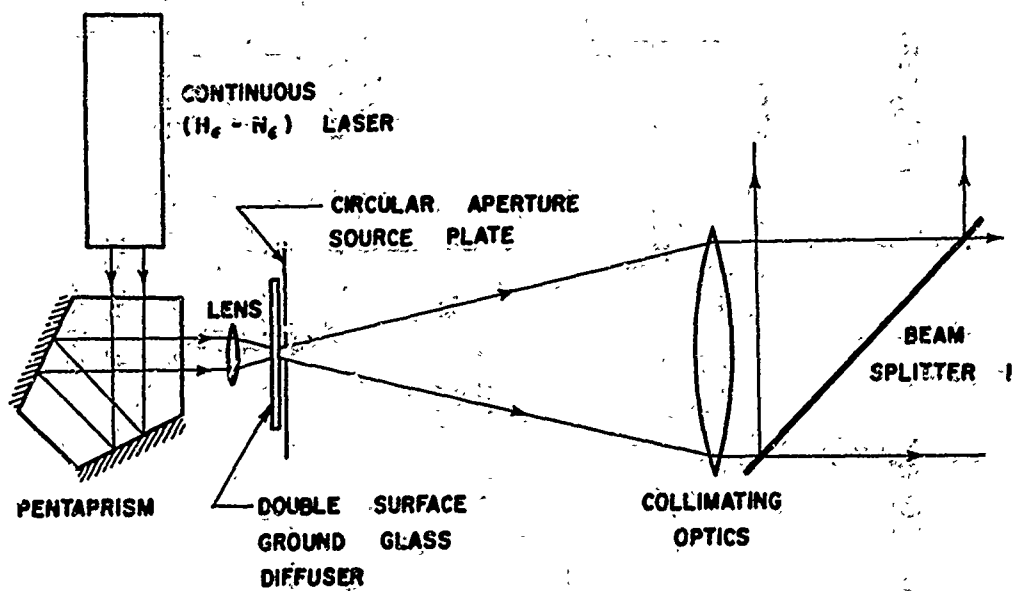


FIG. 5(c). ILLUMINATION OF INTERFEROMETER BY MEANS
OF HELIUM-NEON LASER.

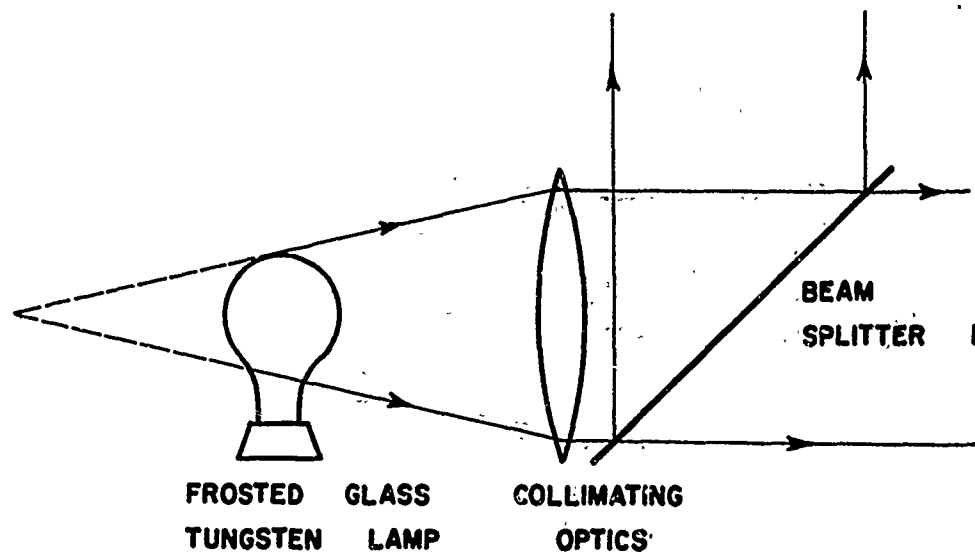


FIG. 5(d). DIFFUSE ILLUMINATION OF INTERFEROMETER BY TUNGSTEN LAMP FOR OBTAINING FOCUSED FRINGES.

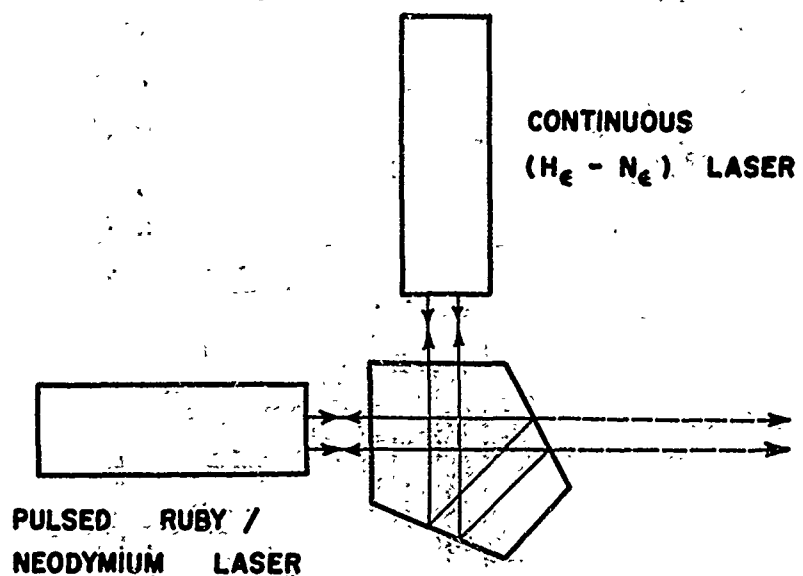


FIG. 5(e). ALIGNMENT OF RUBY/NEODYMIUM LASER WITH INTERFEROMETER SYSTEM BY MEANS OF HELIUM-NEON LASER.

MACH-ZEHNDER
INTERFEROMETER

CAMERA

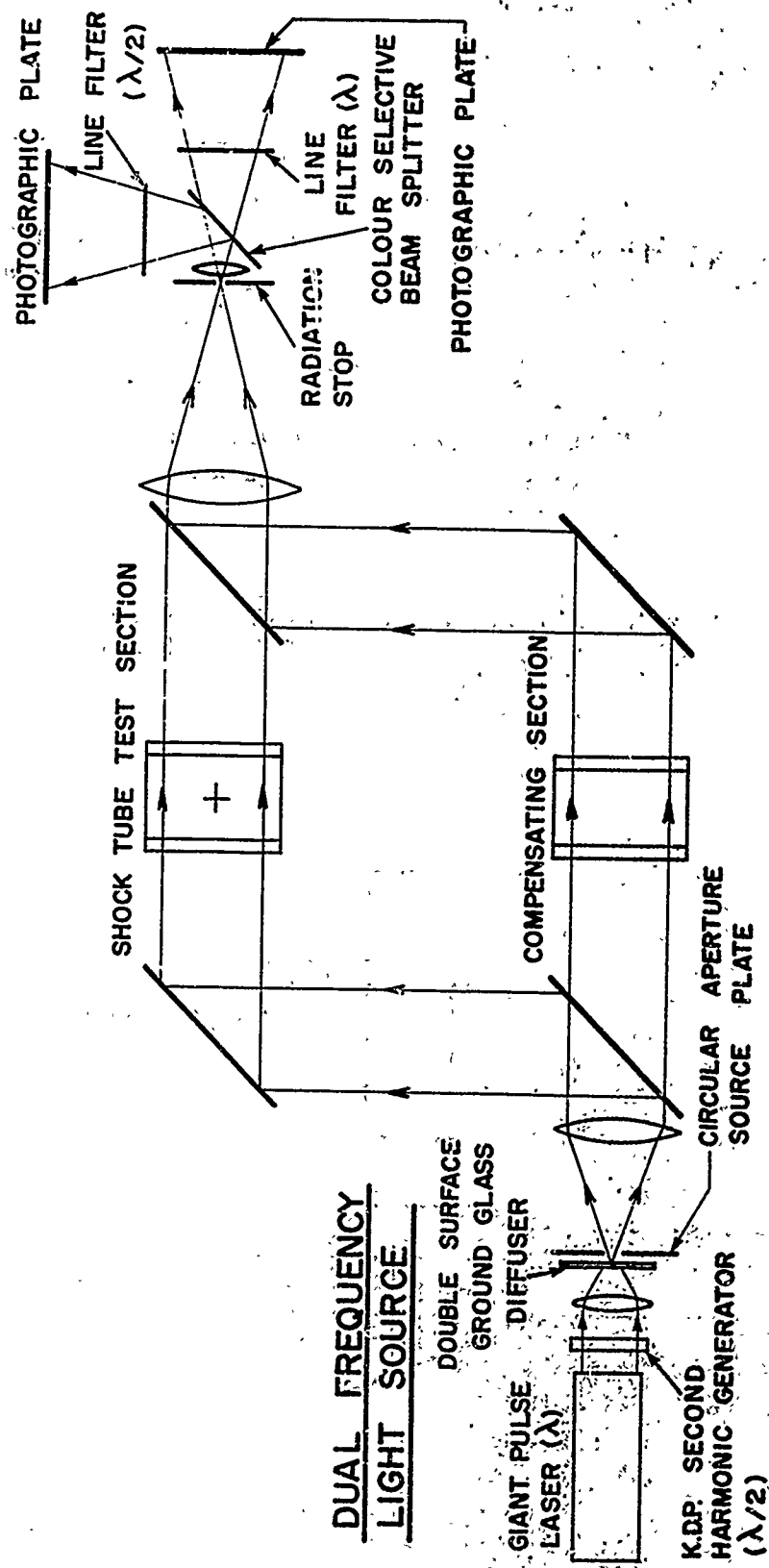


FIG. 5(f) SCHEMATIC OF DUAL FREQUENCY INTERFEROMETER SYSTEM

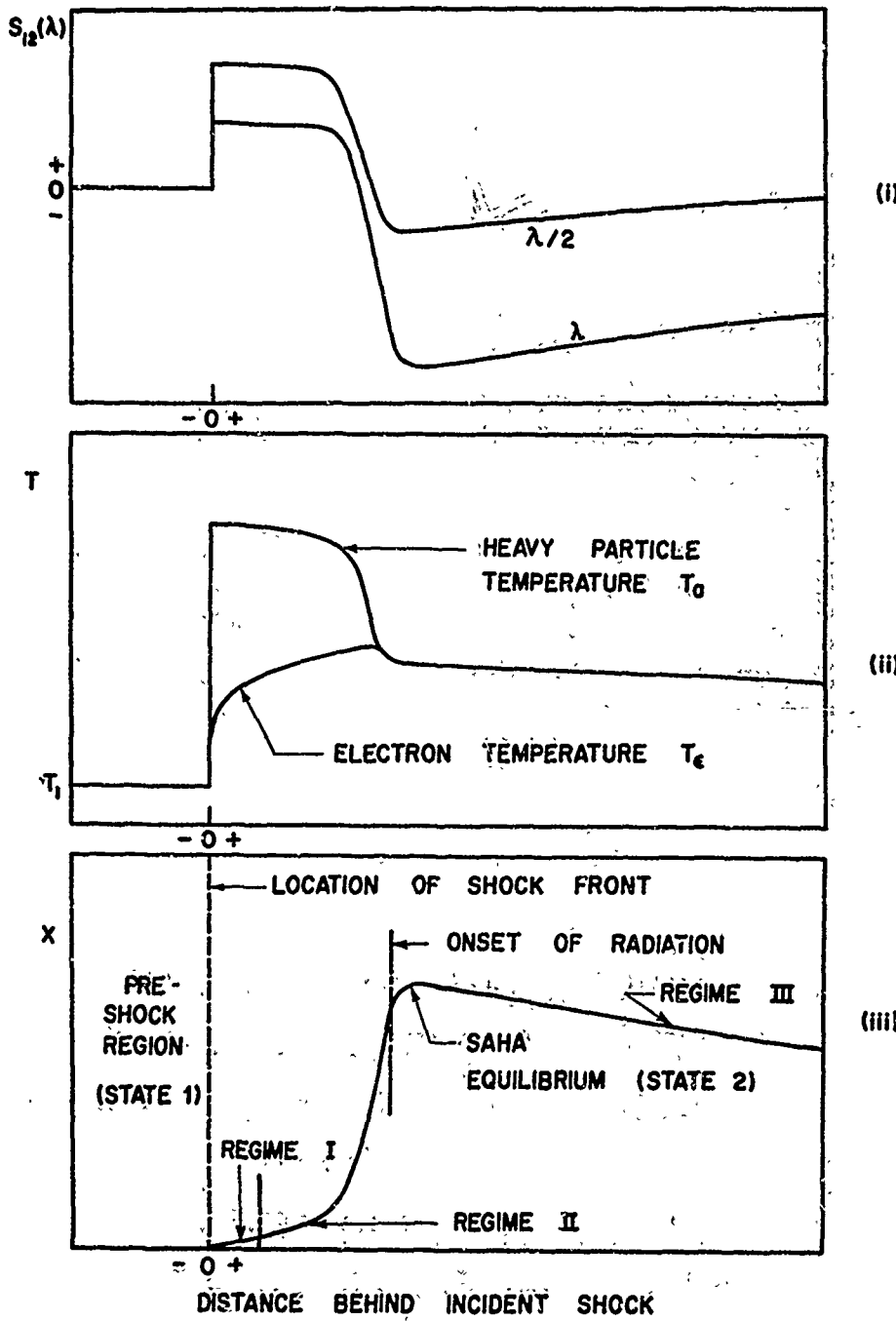
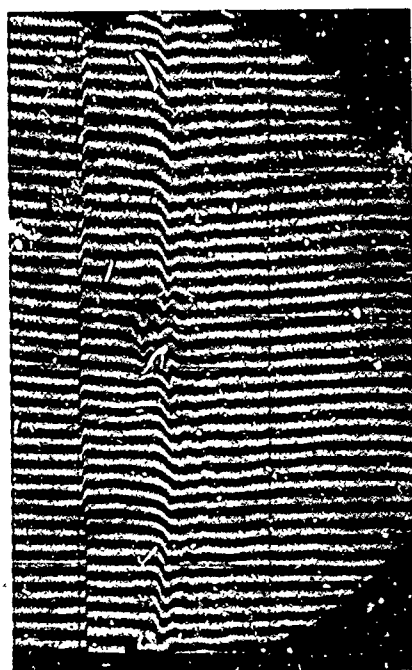
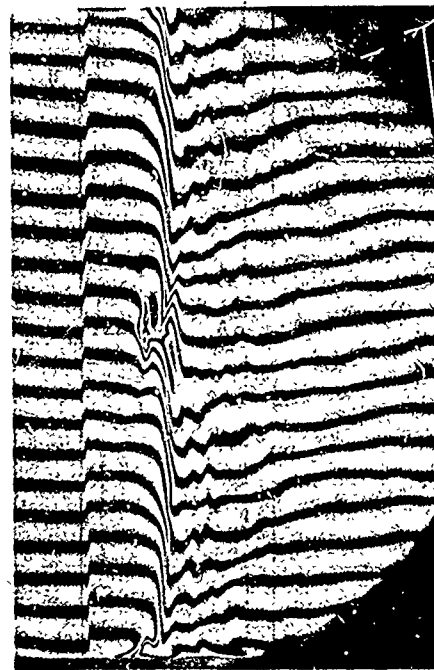


FIG. 6. SCHEMATIC REPRESENTATION OF (i) FRINGE SHIFTS, (ii) TEMPERATURES AND (iii) DEGREE OF IONIZATION BEHIND STRONG SHOCK MOVING IN INERT GAS.
 REGIME I: IONIZATION BY ATOM-ATOM COLLISIONS
 REGIME II: IONIZATION BY ATOM-ELECTRON COLLISIONS
 REGIME III: RECOMBINATION BY RADIATIVE COOLING.



(i)

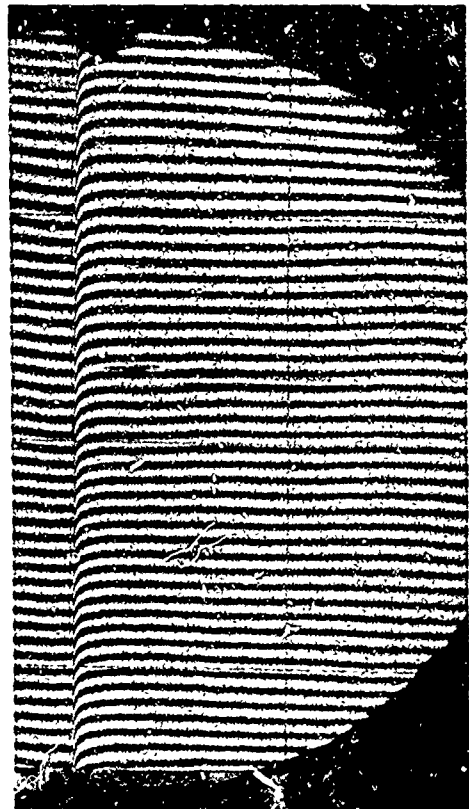


(ii)

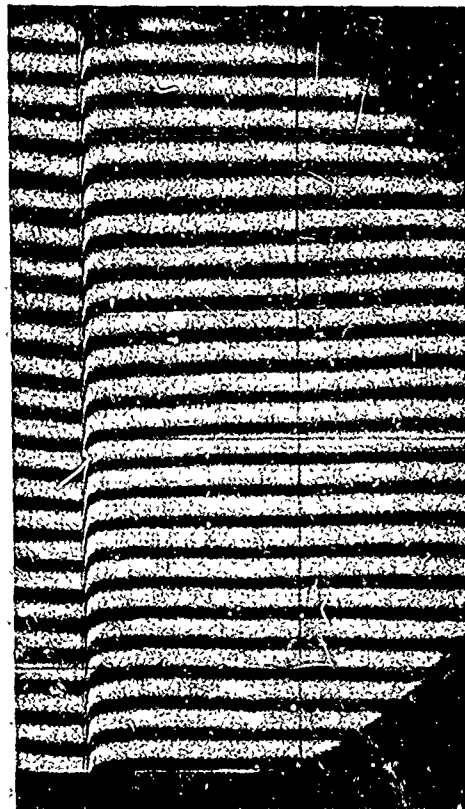
FIG. 7. SIMULTANEOUS MONOCHROMATIC INTERFEROGRAMS FOR A $M_s = 17.46$ SHOCK INTO ARGON AT $p_i = 2.32$ mm Hg WITHOUT THE ADDITION OF HYDROGEN.

(i) $\lambda = 3471 \text{ \AA}$, (ii) $\lambda = 6943 \text{ \AA}$.

SHOCK TRAVELLING TO LEFT. VERTICAL APERTURE 7 INCHES. AN INCREASE IN REFRACTIVE INDEX MOVES THE FRINGES UPWARD.



(i)



(ii)

FIG. 8 SIMULTANEOUS MONOCHROMATIC INTERFEROGRAMS FOR A $M_s = 16.60$ SHOCK INTO NITROGEN AT $p_1 = 2.26$ mm Hg. (i) $\lambda = 3471\text{\AA}$ (ii) $\lambda = 6943\text{\AA}$. SHOCK TRAVELLING TO LEFT. VERTICAL APERTURE IS 7 INCHES. AN INCREASE IN REFRACTIVE INDEX MOVES THE FRINGES UPWARD.

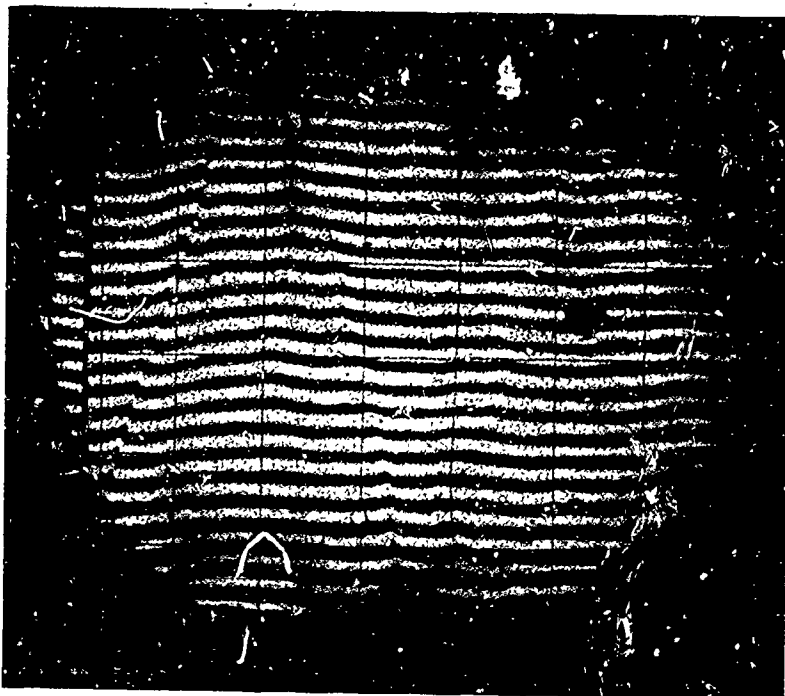


FIG 8(a) INTERFEROGRAM FOR $M_s = 11.6$ SHOCK INTO OXYGEN AT $p_1 = 40.0$ mmHg, $\lambda = 6943\text{\AA}$. SHOCK FRONT AT EXTREME LEFT AND MOVING TO LEFT. INCREASE IN REFRACTIVITY MOVES FRINGES DOWNWARDS

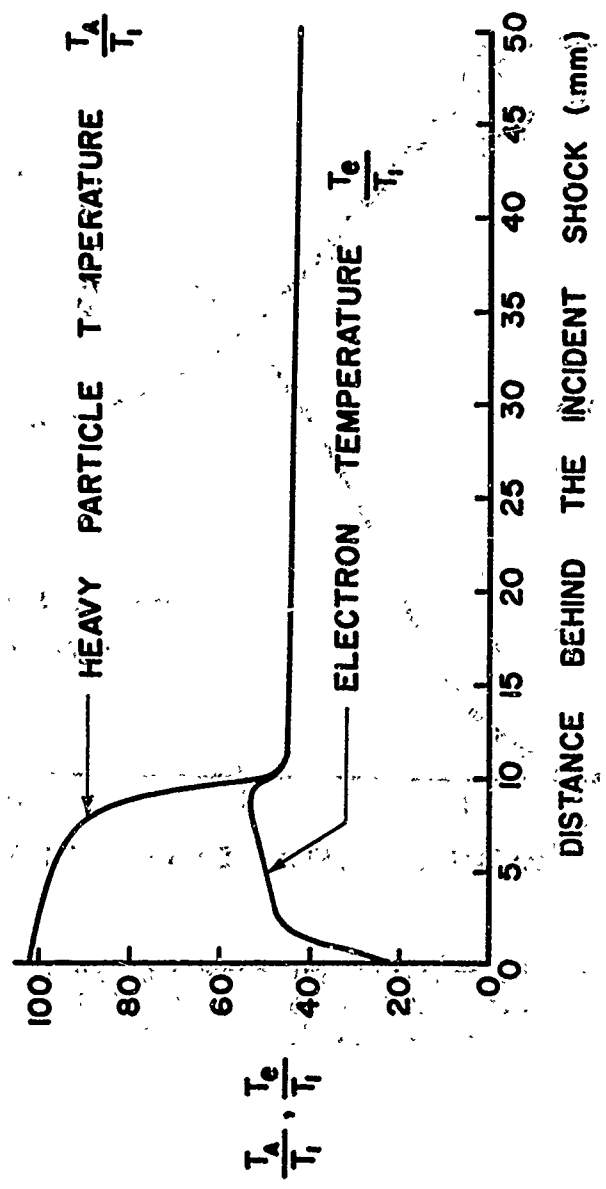


FIG. 9. HEAVY PARTICLE AND ELECTRON TEMPERATURES BEHIND MACH NUMBER 18.0 INCIDENT SHOCK FRONT IN ARGON, $p_1 = 3$ mm Hg, $T_1 = 296.5^\circ\text{K}$, $T_A/T_I = 100$ (FROM REF. 60).

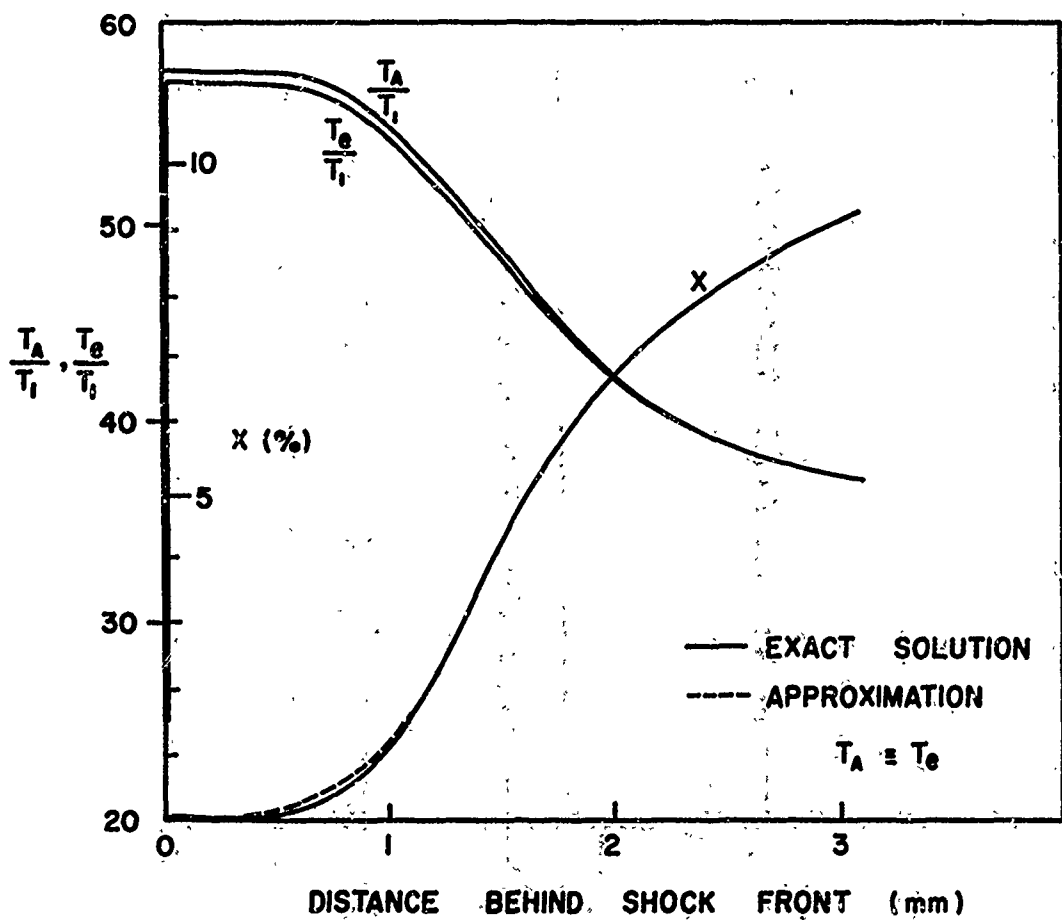
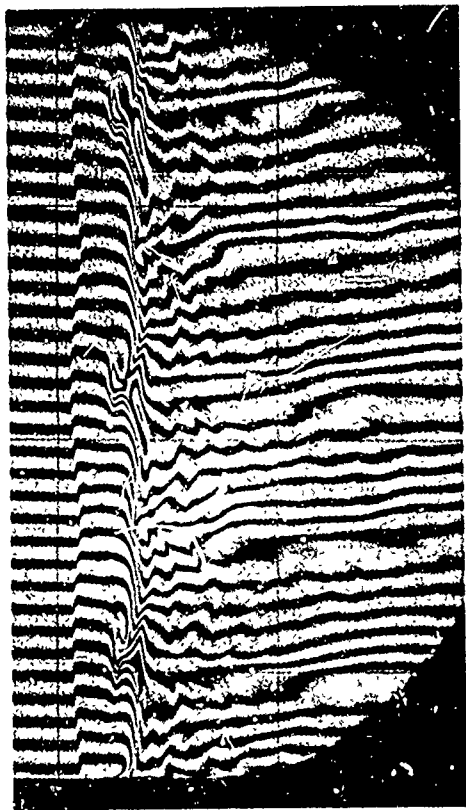
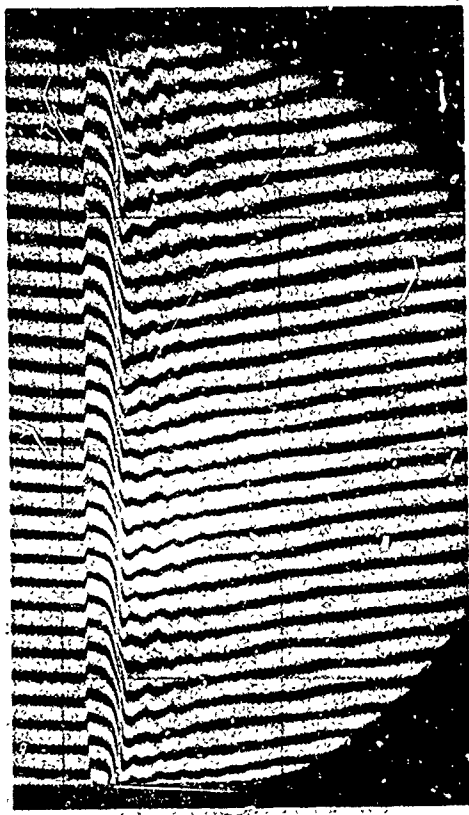


FIG. 10. TEMPERATURE AND DEGREE OF IONIZATION PROFILES BEHIND THE SHOCK FRONT IN HYDROGEN,
 $p_1 = 3 \text{ mmHg}$, $M_s = 25$ (FROM REF. 48).



(i)



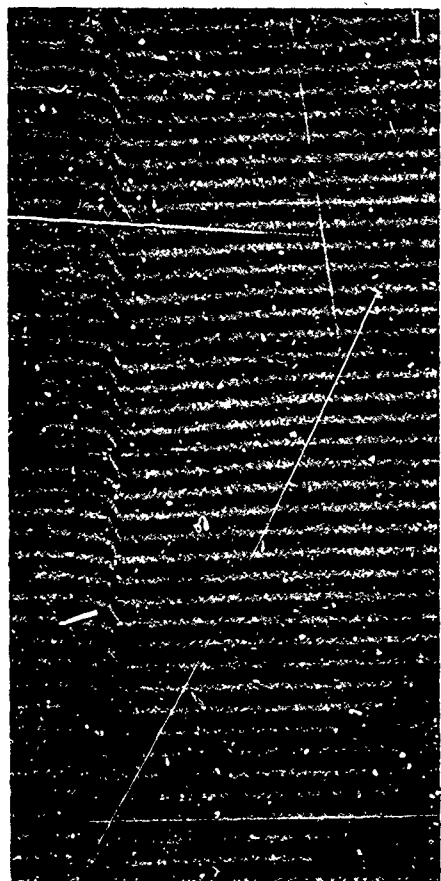
(ii)

FIG. II INTERFEROGRAMS OF SHOCKS INTO ARGON WITH SMALL PERCENTAGES OF HYDROGEN.
 $\lambda = 6943 \text{ \AA}$.

(i) $M_s = 17.01$, $p_i = 2.84 \text{ mm Hg} + 0.033\% \text{ H}_2$

(ii) $M_s = 17.11$, $p_i = 2.85 \text{ mm Hg} + 0.2\% \text{ H}_2$

SHOCK TRAVELLING TO LEFT. VERTICAL APERTURE IS 7 INCHES. AN INCREASE IN REFRACTIVE INDEX MOVES FRINGES UPWARD.



(i)



(ii)

FIG. 12 SIMULTANEOUS MONOCHROMATIC INTERFEROGRAMS FOR A $M_s = 17.15$ SHOCK INTO ARGON + 0.4% H_2 AT $p_i = 2.88$ mm Hg (i) $\lambda = 3471\text{\AA}$
(ii) $\lambda = 6943\text{\AA}$. SHOCK TRAVELLING TO LEFT.
REFERENCE WIRE SPACING IS 2 INCHES.
AN INCREASE IN REFRACTIVE INDEX MOVES THE FRINGES UPWARD.

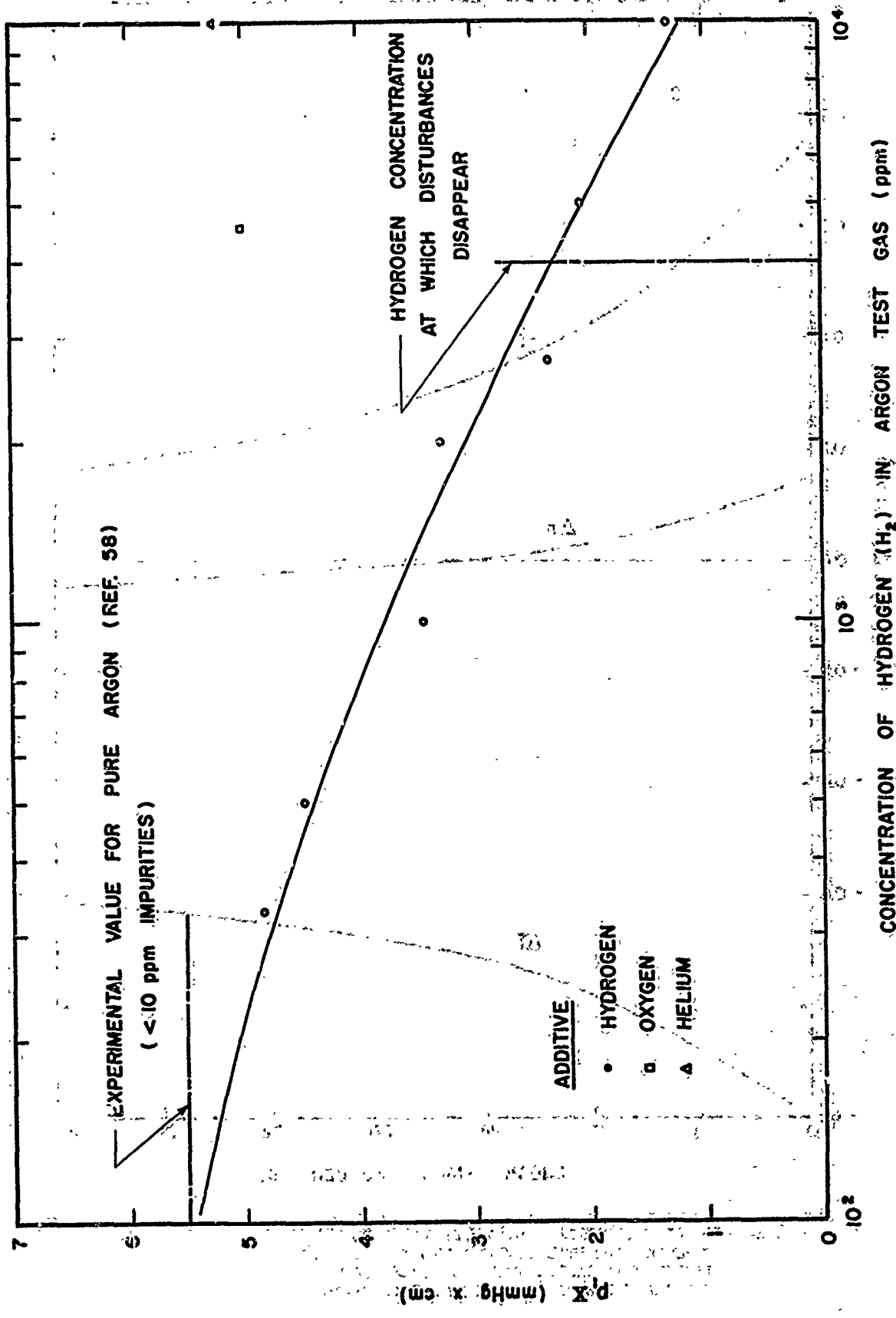


FIG. 13: EFFECT OF HYDROGEN ADDITIVE ON IONIZATION IN INCUBATION ZONE LENGTH $p_1 X$ FOR $M_s = 17.10$ SHOCK INTO ARGON AT $p_1 \approx 2.85$ mmHg.

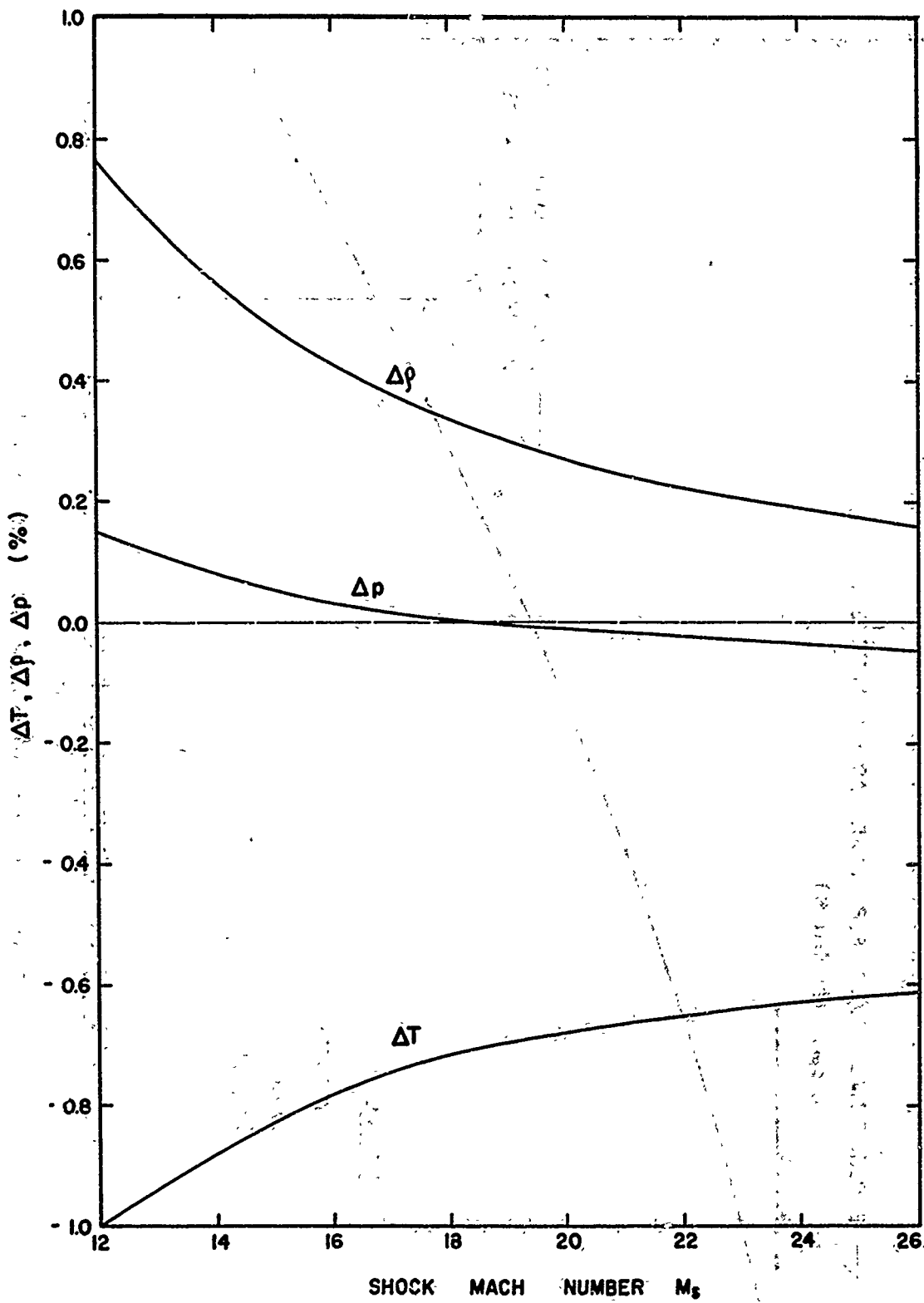
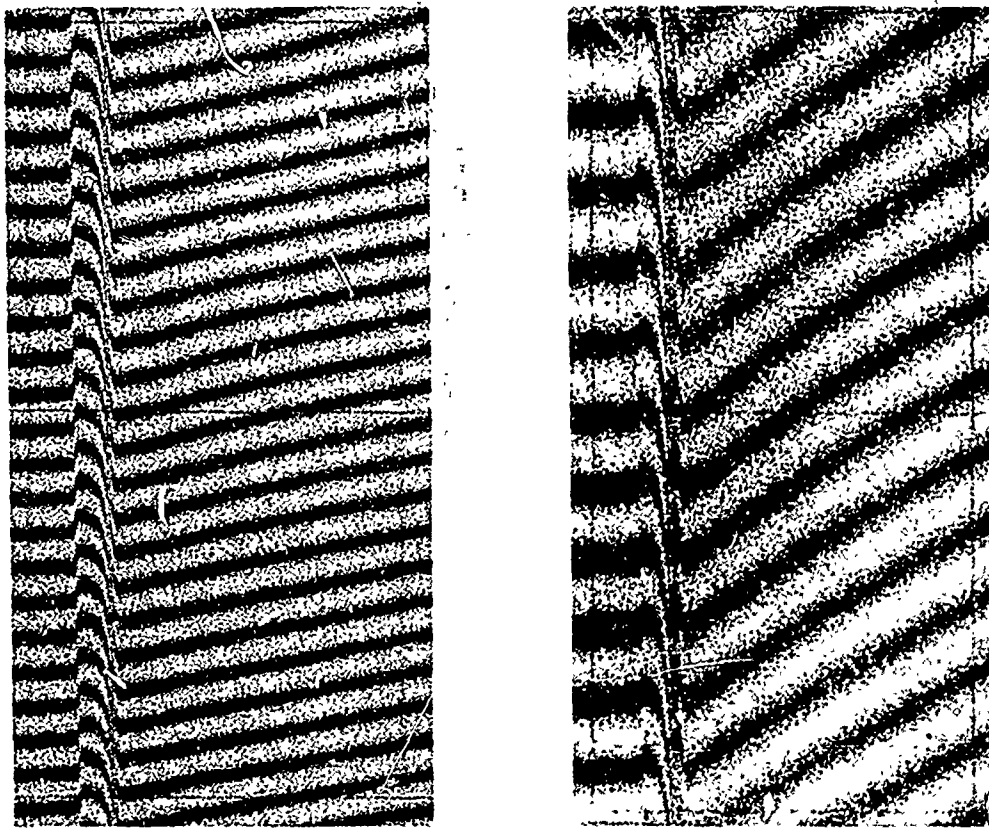


FIG. 14: EFFECT OF ADDITION OF 0.4% HYDROGEN ON FROZEN SHOCK PROPERTIES FOR SHOCK MOVING INTO ARGON SHOWN AS PERCENTAGE DEVIATIONS FROM THE VALUES FOR PURE ARGON. HYDROGEN ASSUMED TO BE COMPLETELY DISSOCIATED.



(i)

(ii)

FIG. 15 SIMULTANEOUS MONOCHROMATIC INTERFEROGRAMS
FOR A $M_s = 18.14$ SHOCK INTO ARGON + 0.4% H_2
AT $p_1 = 2.45$ mm Hg (i) $\lambda = 5300 \text{ \AA}$ (ii) $\lambda = 10600 \text{ \AA}$
SHOCK TRAVELLING TO LEFT. REFERENCE WIRE
SPACING IS .2 INCHES. AN INCREASE IN REFRAC-
TIVE INDEX MOVES THE FRINGES UPWARD.

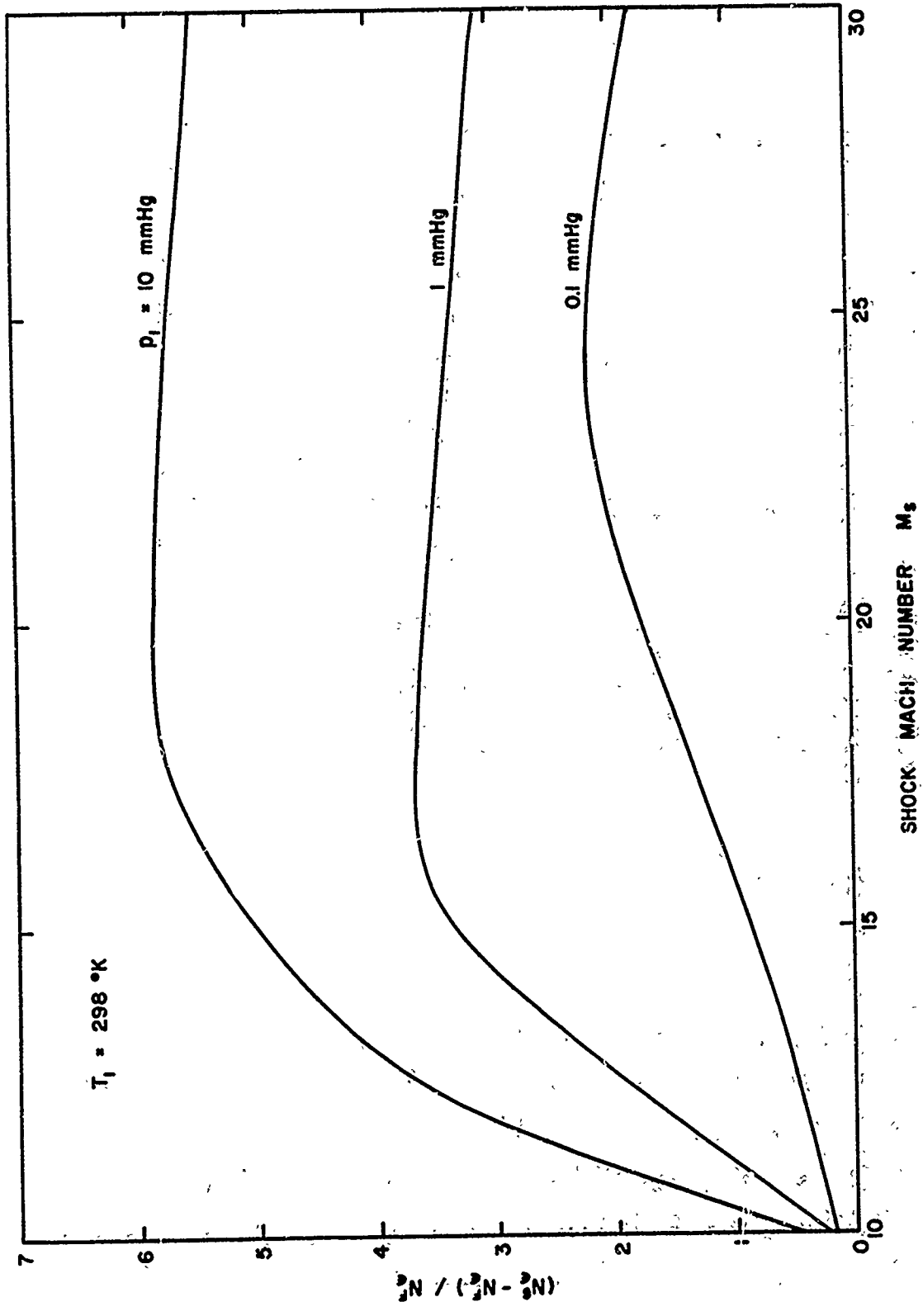


FIG. 16. COMPARISON OF ELECTRON DENSITIES CALCULATED FOR SAHA EQUILIBRIUM BEHIND INCIDENT SHOCK INTO ARGON. N_e^G CALCULATED USING ONLY GROUND STATE TERM IN ELECTRONIC PARTITION FUNCTION. N_e^F CALCULATED USING FULL ELECTRONIC EXCITATION PARTITION FUNCTION.

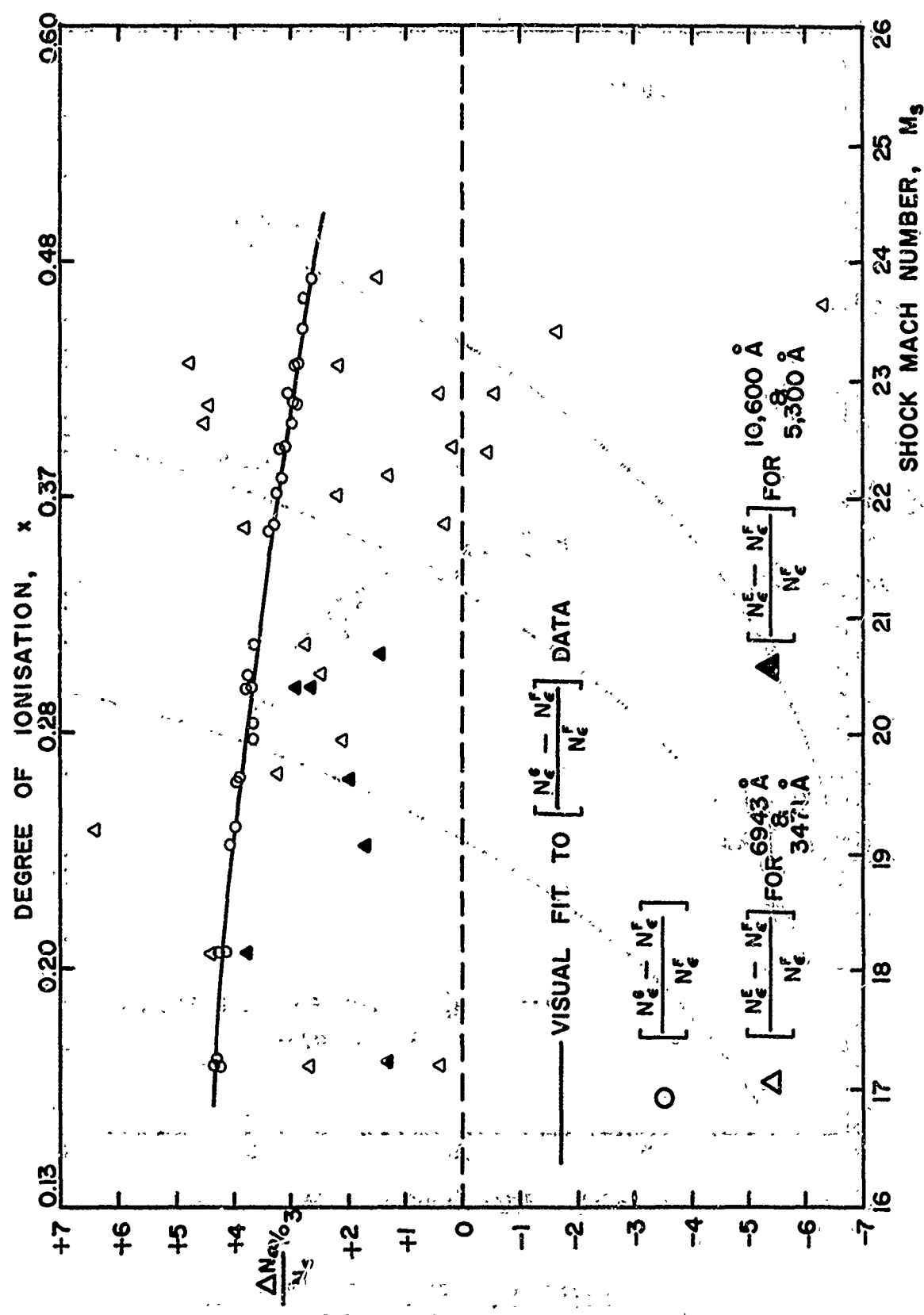


FIG. 17. COMPARISON BETWEEN EXPERIMENTAL ELECTRON DENSITY N_e^{exp} AND N_e^{eq} CALCULATED FOR SAHA EQUILIBRIUM BEHIND INCIDENT SHOCK INTO ARGON USING FULL ELECTRON EXCITATION PARTITION FUNCTION. ALSO COMPARISON BETWEEN N_e^{F} AND N_e^{eq} CALCULATED AS FOR N_e^{F} BUT USING ONLY GROUND STATE TERM OF PARTITION FUNCTION.

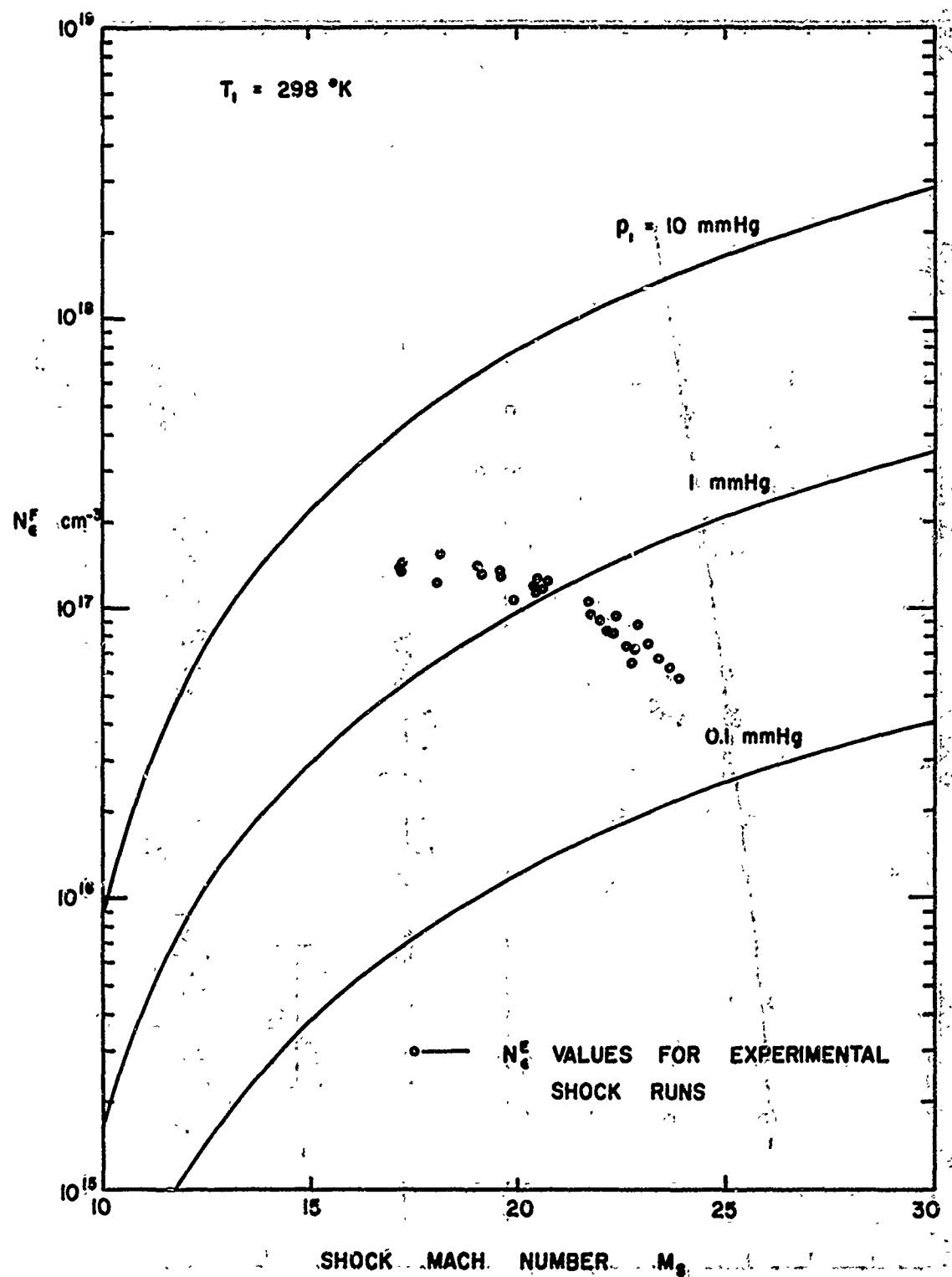


FIG. 18. ELECTRON DENSITY N_e^F CALCULATED FOR SAHA EQUILIBRIUM BEHIND INCIDENT SHOCK INTO ARGON USING FULL ELECTRONIC EXCITATION PARTITION FUNCTION.

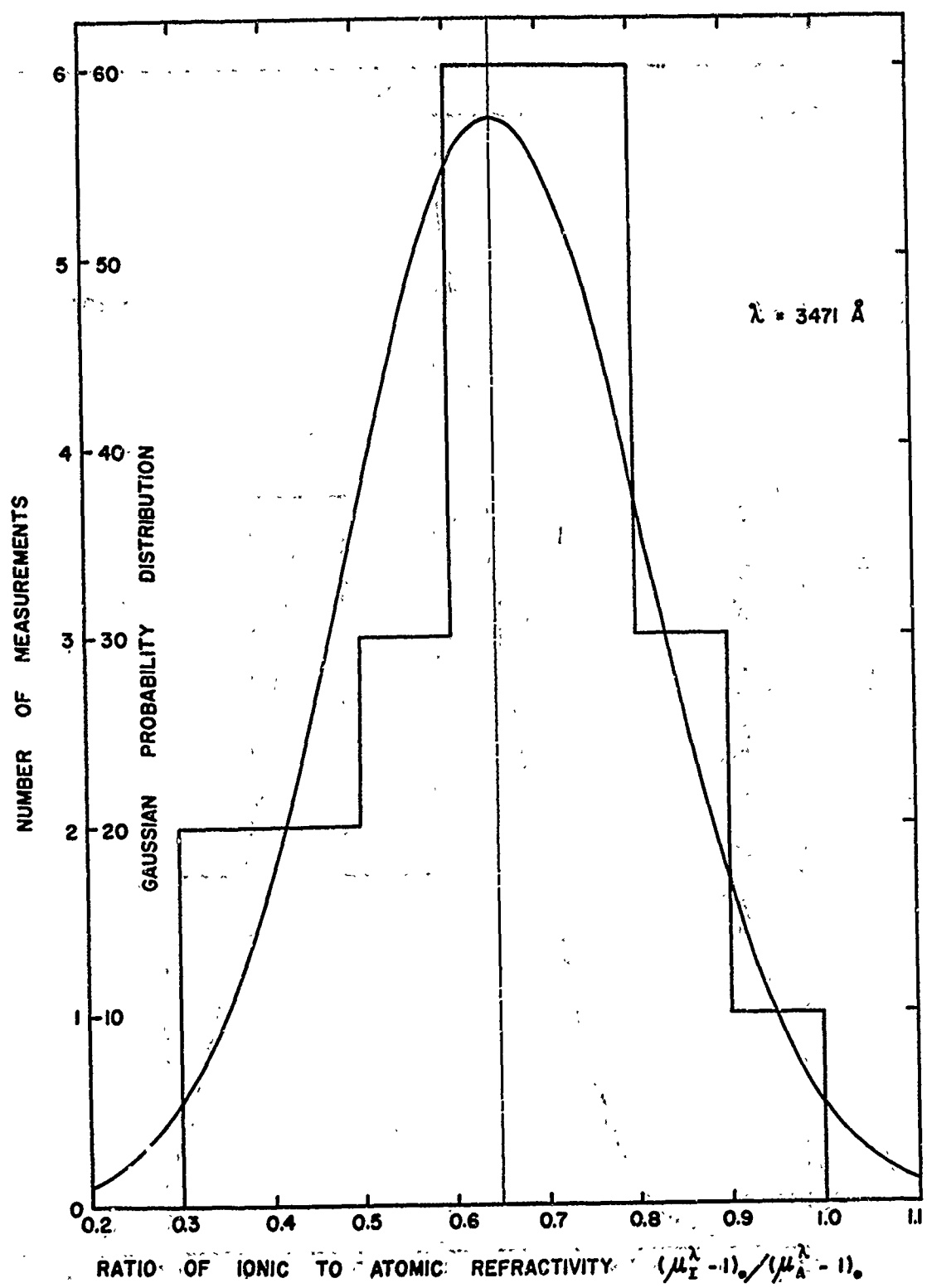


FIG. 19: HISTOGRAM OF EXPERIMENTAL $(\mu_I^\lambda - 1)_o / (\mu_A^\lambda - 1)_o$.
 RESULTS FOR $\lambda = 3471 \text{ \AA}$. MEAN VALUE = 0.650.
 TOTAL NUMBER OF MEASUREMENTS $N = 23$.
 STANDARD DEVIATION $\sigma = 0.160$. STANDARD
 ERROR OF MEAN $(\sigma/\sqrt{N}) = 0.033$.

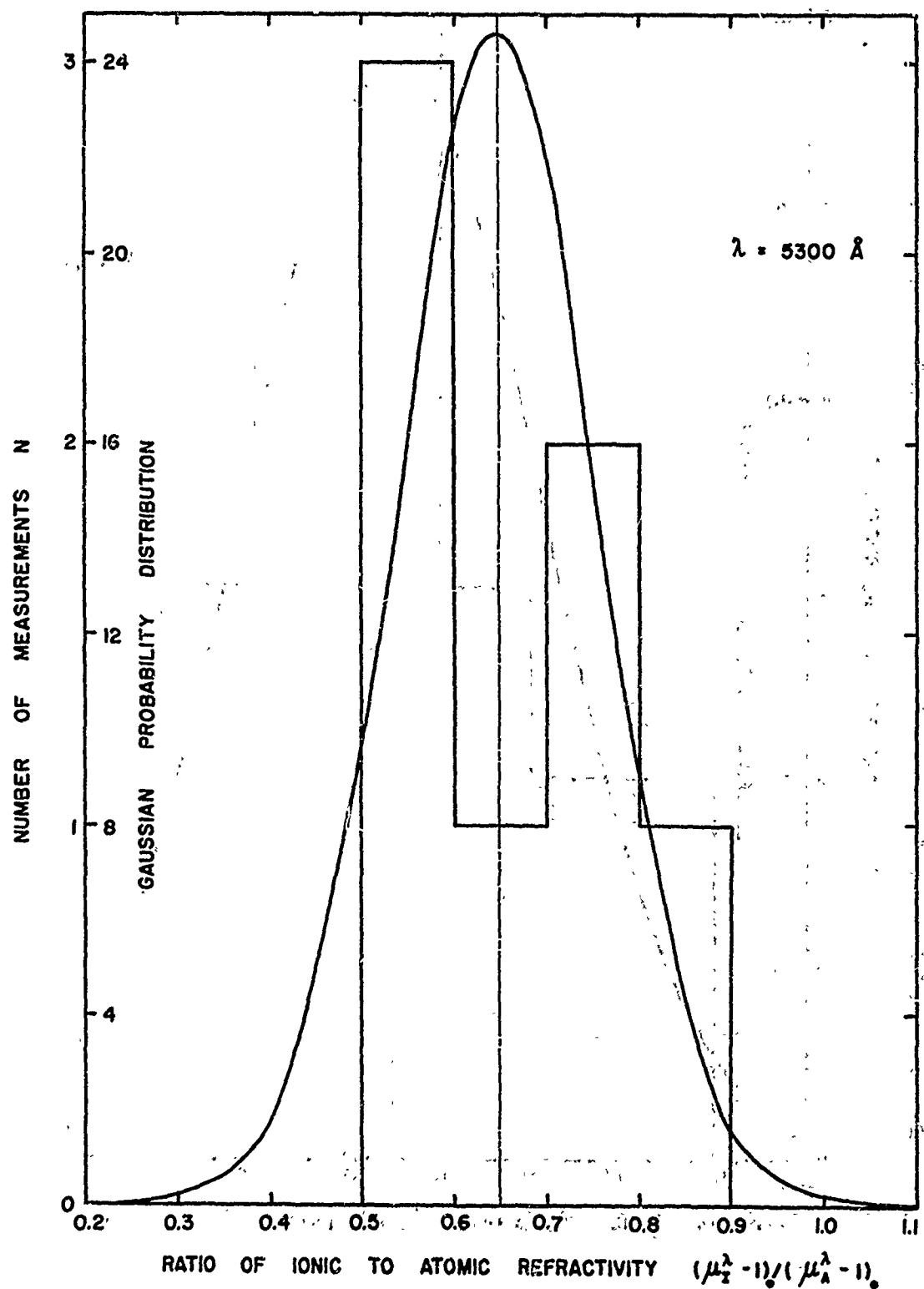


FIG.20: HISTOGRAM OF EXPERIMENTAL $(\mu_i^\lambda - 1) / (\mu_A^\lambda - 1)$ RESULTS FOR
 $\lambda = 5300 \text{ \AA}$. MEAN VALUE ≈ 0.647 . TOTAL NUMBER OF
 MEASUREMENTS $N = 7$. STANDARD DEVIATION $\sigma = 0.107$.
 STANDARD ERROR OF MEAN $(\sigma/\sqrt{N}) \approx 0.041$.

APPENDIX A: PROCEDURE FOR THE ANALYSIS OF THE INTERFEROGRAMS

This appendix describes the procedure for determining the equilibrium fringe shift between pre-shock state 1 and post shock (equilibrium) state 2 with the shockwave moving into the region of state 1 in a direction parallel to the fringe field so that the shock front lies perpendicular to this same fringe field (see Fig. A-1(i)).

For an ideal interferometer, devoid of inhomogeneities due to optical defects, vibrations and air currents, the measurement of the fringe shift is straightforward. This is achieved by extrapolating any given monochromatic fringe in region 1 into the desired equilibrium state in region 2 and measuring the total shift in terms of the fringe spacing.

In the present system, due to imperfections in the optical components such that the fringes connecting regions 1 and 2 are not perfectly straight and horizontal, it is necessary to take an interferogram of the optical field in the absence of the shock induced fringe shift. This therefore provides a map of the optical inhomogeneities present in the interferometer which can then be subtracted from the fringe shift measurements obtained from the shock flow interferograms so as to give the fringe shift due to the shock flow alone. It is therefore important that neither the flow nor the no-flow interferograms contain any fringe movements or distortions due to mechanical vibrations or air currents as correction for these shifts is beyond the control of the present experiment. The interferometer is therefore sealed in an airtight enclosure and care is taken to ensure that all sources of low frequency vibrations are inoperative during the period of any one experiment.

However, due to the finite time which exists between the taking of the no-flow and flow interferograms (465 minutes), it is possible for the interferometer setting to change due to thermal or mechanical disturbances. This can result in small changes in fringe spacing, position or orientation thereby constituting a source of error which must be accounted for in addition to that due to the inhomogeneities of the optical system.

Figure A-1 shows in schematic form the flow (i) and the no-flow (ii) interferograms typical of those encountered in this work where three dark monochromatic fringes are represented by continuous lines. The three fringes in the no-flow interferogram which are not necessarily the same three in the flow interferogram are intentionally given an exaggerated non-ideal appearance for the sake of this discussion.

The broken lines represent the horizontal and vertical reference wires referred to in Section 3.2 where the vertical wire is located so as to overlie the pre-shock zone (state 1) at a point close to the shock front. Point X' on the flow interferogram is chosen to lie at any desired equilibrium (or non-equilibrium) state 2. Point Y' on the no-flow interferogram is then chosen such that YY' = XX' on the assumption that the two interferograms are reproduced on the same scale otherwise a scaling factor is used.

The exercise therefore involves the measurement of the fringe fractions a, b, c, d, k, l, m and n formed on either side of the reference points X, X', Y and Y'. The purpose of measuring these fringe fractions, rather than following a given fringe through the shock front is that the measurements are localized in a given region of the aperture with respect to the given fixed

reference points X, X', Y and Y'. Therefore, provided the fringe spacing is small in relation to any region of fringe distortion, it should be possible to correct for these inhomogeneities in spite of small differences of fringe setting which occur between the fringes in region 1 of the flow interferogram to those in region 1 of the no-flow interferogram.

The shock flow fringe shift $S_{12}^\lambda(F)$ between pre-shock state 1 and shock state 2 can be given as

$$S_{12}^\lambda(F) = A + \frac{c}{(c+d)} - \frac{a}{(a+b)}$$

or alternatively as

$$S_{12}^\lambda(F) = A + \frac{b}{(a+b)} - \frac{d}{(d+c)} \quad (A-1)$$

where the integral fringe shift A is the minimum number of dark fringes one crosses in passing from X to X'. It should be noted that both equations in Eq. A-1 are exactly equivalent as they can both be reduced to the common form

$$S_{12}^\lambda(F) = A-1 + \frac{b}{(a+b)} + \frac{c}{(c+d)} .$$

Going from X to X' integral fringe shifts upwards are arbitrarily denoted as being positive and those downwards as negative but where the fringe fractions a,b,c,d, etc are scalar quantities. For the trivial example shown in Fig. A-1, $\lambda = +1$, $A = +1$ and $B = -1$. Clearly if a given fringe should recross either of these reference lines between points X and X' or Y and Y', then it should not be included in the values for A or B.

Ideally no change in fringe setting occurs between the taking of the no-flow and flow interferograms. In reality this is not the case due to the effects of vibrations, air currents and temperature changes such that $a \neq k$ and $b \neq l$. With a view to improving the accuracy of the measurements of $S_{12}^\lambda(F)$, the two values for $S_{12}^\lambda(F)$, given by Eq. A-1 are averaged to give

$$S_{12}^\lambda(F) = A + \frac{1}{2} \left[\frac{(c-d)}{(c+d)} + \frac{(b-a)}{(b+a)} \right] \quad (A-2)$$

In a similar manner it is now possible to obtain the corresponding vertical fringe shift $S_{12}^\lambda(NF)$ occurring between states 1 and 2 on the no-flow interferogram due to optical defects in the system. The equivalent average value for $S_{12}^\lambda(NF)$ is given by

$$S_{12}^\lambda(NF) = B + \frac{1}{2} \left[\frac{(m-n)}{(m+n)} + \frac{(l-k)}{(l+k)} \right] \quad (A-3)$$

The true total fringe shift S_{12}^λ due to the gas-dynamic phenomenon under investigation is therefore given by

$$S_{12}^\lambda = S_{12}^\lambda(F) - S_{12}^\lambda(NF)$$

which by substitution from Eq. A-2 and A-3 becomes

$$S_{12}^\lambda = A-B + 1/2 \left[\frac{(c-d)}{(c+d)} + \frac{(b-a)}{(b+a)} - \frac{(m-n)}{(m+n)} - \frac{(l-k)}{(l+k)} \right] \quad (A-4)$$

where the denominators for the terms within the brackets represent the fringe spacings about reference X, X', Y and Y'. Due to optical defects in the system, these fringe spacings do not have a common value although normal circumstances the differences are small.

It is now pertinent to discuss the effect of large optical inhomogeneities and changes of fringe setting which occur between the taking of the no-flow and flow interferograms on the validity of this analytical procedure. If the fringe spacing is large in relation to any given region of optical imperfection, then it is possible for this region to lie between two dark fringes at point X' on the flow interferogram (say) such that the fringes appear to be straight and parallel. However, this same region may lie at some intermediate fringe position at point Y' on the no-flow interferogram such that the local fringe profile now exhibits a non-ideal shape. It is therefore clear that the no-flow interferogram will introduce a fringe shift correction for an optical defect which is not included in the data from the flow interferogram. The effect of this anomaly can be minimized by taking one or both of two precautions. Firstly by ensuring that the fringe spacing is much smaller than any region of optical inhomogeneity, the fringe field effectively becomes a continuous map of the transmitted optical wavefront with all defects being clearly defined. This expedient is of course subject to the proviso that the fringe spacing be much larger than either the photographic emulsion or diffuser generated grain size or the reference wire diameter.

The other means by which this difference between the two interferograms can be minimized is by taking an average value for the fringe spacing about points X and Y and similarly for points X' and Y'. These average spacings are $(c+d+m+n)/2$ and $(b+a+k+l)/2$, which when substituted for the original values used in Eq. A-2 and A-3, provide a new expression for the total fringe shift given by

$$S_{12}^\lambda = A-B + \left\{ \frac{(c-d)-(m-n)}{(c+d+m+n)} + \frac{(b-a)-(l-k)}{(b+a+k+l)} \right\} \quad (A-5)$$

However except for relatively large differences between $(c+d)$ and $(m+n)$ and between $(b+a)$ and $(l+k)$, the value of S_{12}^λ given by Eq. A-5 is not likely to differ from the value given by Eq. A-4 by more than a fraction of one percent.

The effect of a change of fringe setting between the no-flow and flow interferograms on the value of S_{12}^λ can be considered in three parts. Firstly a change in vertical fringe position will only affect the fringes for preshock state 1 as a change in fringe position between the no-flow and flow interferograms for post-shock state 2 already exists. Clearly, the effect of this movement is subject to the comments already made regarding this point for region 2. Secondly, a change in fringe spacing ($\leq 1/20$ fringe say) will not have a noticeable effect on S_{12}^λ as calculated from either Eq. A-4 or A-5 provided the fringe spacing is sufficiently fine to resolve all the optical imperfections in the system. This is due to the fact that the ratio of the fringe fractions to the fringe spacings remains constant.

Finally, the effect of a change in fringe orientation away from the

horizontal setting occurring between the no-flow and flow interferograms cannot be dismissed as easily as for the effect of the other changes in fringe adjustment already discussed. Besides generating an apparent change in fringe spacing as viewed in the vertical direction, the measured fringe shift for the flow interferograms will clearly depend on the length of XX' . Precautions should therefore be taken to minimize this change in fringe orientation from the horizontal direction by isolating the interferometer from all external influences and by reducing the time period between the taking of the no-flow and flow interferograms. In addition the effect of this change on S_{12}' can be minimized by making XX' as small as possible or, in the presence of large changes in fringe orientation of the order of 5° to 10° , by making the fringe shift measurements in a direction perpendicular to the given fringe field instead of in a direction perpendicular to the horizontal reference wire, so that the fringe fractions a , b , c and d maintain an approximately correct numerical relationship to the values k , l , m and n for the no-flow interferogram.

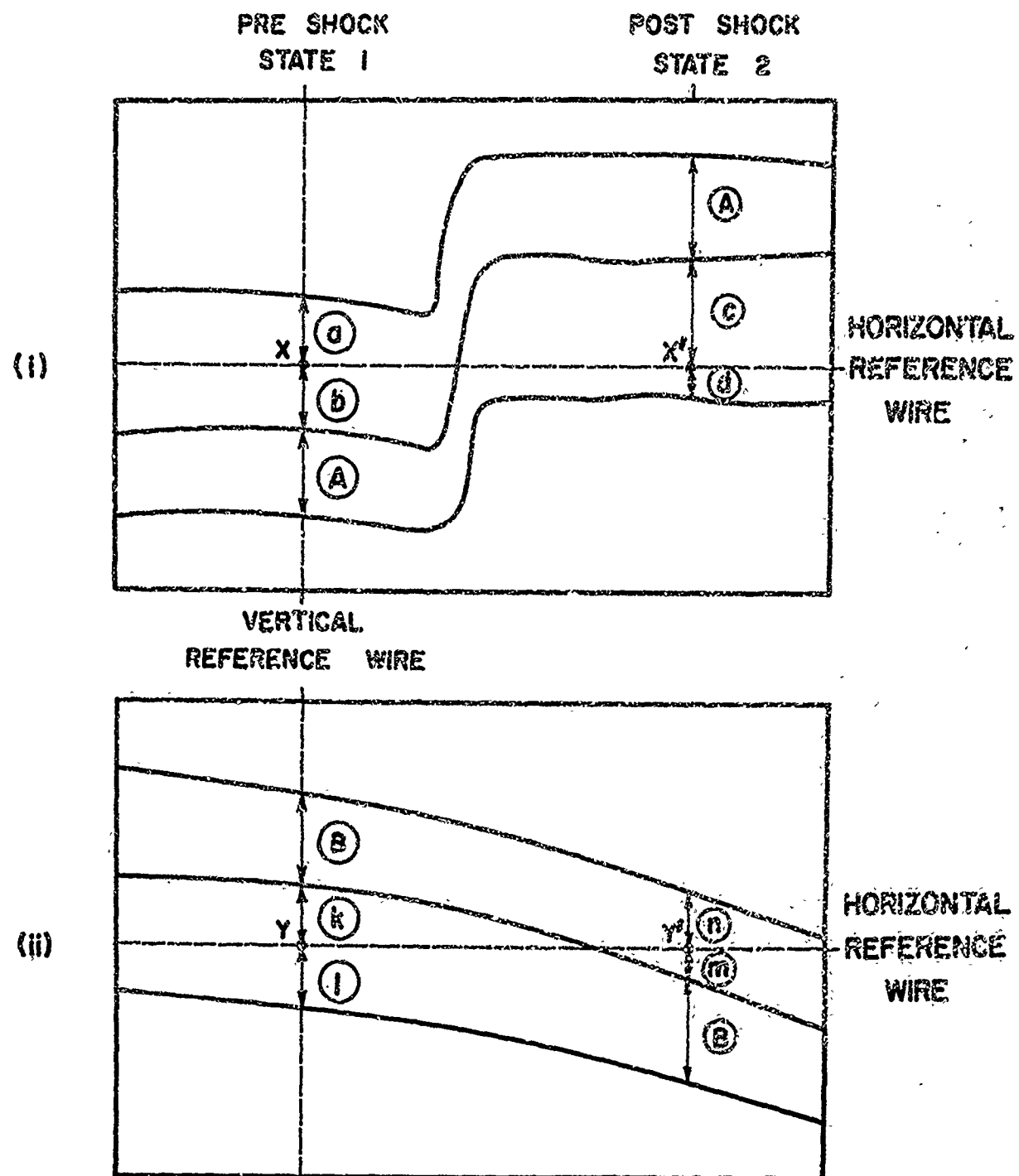


FIG. A-1. SCHEMATIC REPRESENTATION OF (i) FLOW INTERFEROGRAM OF SHOCK WAVE MOVING TO LEFT AND (ii) NO-FLOW INTERFEROGRAM. NOMINALLY HORIZONTAL DARK FRinges ARE SHOWN AS SOLID LINES. FRINGE SHIFT UPWARD FROM STATE 1 TO 2 IS POSITIVE.